An Analytical Model of Reinforced Concrete Beam-Column Joints Subjected to Cyclic Loading in Application to Frame Analysis

by

Tran Xuan Hoa

Student ID Number: 1196010

A dissertation submitted to the

Engineering Course, Department of Engineering,

Graduate School of Engineering,

Kochi University of Technology,

Kochi, Japan

in partial fulfillment of the requirements for the degree of

Doctor of Engineering

Assessment Committee:

Supervisor:	Yoshiro Kai
Co-Supervisor:	Seigo Nasu
	Hiroshi Shima
Committee:	Kazuhiro Kitayama (Tokyo Metropolitan University)
	Fumio Kusuhara (Nagoya Institute of Technology)
	Tomohiro Tsuji

September 2018

[This page is originally blank]

Abstract

Shear failure of beam column connections have attracted many researchers since it can lessen significantly the seismic resisting capability of a reinforced concrete (RC) frame building. For many years, with strong attention to this object, researchers have conducted numerous exprimental works, introduced theories to explain failure mechanisms, proposed analytical models, and developed design criteria with the aim of enhancing joint stiffness.

Recently, a new theory named *joint hinging* with considering joint shear deformation caused by rotation of four rigid bodies respect to hinging points has been proposed to explain joint shear failure mechanism. The theory exhibits some advantages in comparison to previous works with respect to characterizing new aspects revealed from experimental investigations. As a part of the theory, a mechanical model has been introduced to predict joint moment capacity. In this study, the major interest is to develop a two dimensional (2D) macro element based on that mechanical model to simulate behaviors of RC beam column connections under lateral loading. Bar springs and bond-slip springs are employed to represent in turn reinforcements and bond between bars and surrounding concrete, whereas struts are utilized to charecterize compressive zone in concrete which distinguish the joint element from previous multi-spring models. Deformations of these components resemble the rotation of rigid bodies in Shiohara mechanism. A configuration of joint independent deformations is also defined to form joint compatibility relationship, then the joint stiffness is established using the constitutive laws of material.

From the first main focus on modelling interior joints under cyclic loadings, applicability of the new joint element on simulating performances of exterior joints and knee joints is also presented. Additionally, application on investigating responses of a RC frame subjected to cyclic loading is then mentioned with the verification from the experimental data.

Contents

List of Figures

List of Tables

Chapter 1 Introduction

1.1 Motivation for the study

Many experimental investigations have revealed that the degradation of beam-column joint stiffness considerably induces the collapse of frame buildings. In practice, concrete design codes such as AIJ, ACI, NZS, EC8 have already included in their seismic provisions guidelines for preventing shear failure in beam-column joint [1-4]. Recently, Shiohara has developed an innovative theory which named *Joint hinging mechanism* to explain the joint shear failure action which was first introduced [5], then analytically predicted [6], and finally verified by experiments [7]. A method to determine the joint hinging strength derived from the mechanism is also included in preparation for the new AIJ code [8].

Several analytical models based on the mechanism have been proposed to simulate joint seismic performances including an elasto-plastic joint model for frame analysis [9], a 2D multi-spring joint model [10], and a 3D multi-spring joint model [11]. They tried to use springs to perform behaviors of materials including reinforcements and concrete. However, a model developed directly from its mechanism and keeping all of its original aspects is not available because in estimating the joint strength, only equilibrium of forces is adopted and compatibility is neglected [5].

1.2 Research Objective

1.2.1 Originality

Different from other multi-spring models, the present joint model was fabricated directly from Shiohara's joint hinging mechanical model. In the mechanical model, the joint deformation was attributed to the rotation of rigid segments respect to hinging points and an equilibrium of forces which consisted of the external forces and internal forces in concrete and reinforcements was established to predict the joint moment capacity. The research here defined the joint components such as bar springs, concrete struts and bond-slip springs so that their deformations resembled the rotation of rigid segments in Shiohara mechanical model. Moreover, the axial force of these struts and springs resembled the respective internal forces of material in the mechanical equilibrium. As a result, the equilibrium was reserved and a corresponding compatibility was proposed to establish the joint stiffness.

1

1.2.2 Procedure

- Define a new 2D configuration of the joint deformations and define the joint components developed from Shiohara theory
- Establish the joint compatibility and the joint 2D stiffness, then verify the joint model in sequence: the monotonic response of the interior joints with an identical depth and with a different depth of beams and columns, with and without perfect bond condition, and the cyclic response of the interior joints with normal properties.
- Apply on investigating the response of the exterior joints, knee joints and a RC frame under lateral loading

1.2.3 Contribution

- Include compatibility into Shiohara's joint hinging mechanism successfully
- Propose a new 2D RC beam-column joint element which keeps essential original aspects of Shiohara's joint hinging mechanism and show applicability in simulating cyclic response and developing a structural design tool for 2D RC frame structures.

1.3 Review of the previous studies on the seismic response of RC beam-column joints

As one of the most sensitive regions of a RC frame building under earthquake, beam-column connection has been interested by many researchers. During last several decades, a plenty of experiments regarding cyclic loadings have been conducted to study the degradation of joint stiffness and bar anchorage loss, whereby revealed the inelasticity of joint performances. Durani et al. [12] tested six specimens of full-scale interior beam-column joints under cyclic loadings and found that behaviors of beam-column connections were considerably influenced by the magnitude of joint shear stress in case of lacking transverse beam and slab. Joint hoops contributed significantly to confinement of a joint, enhanced joint performances and a perfect improvement could be made with an odd number of steel hoops no less than three layers. Walker et al. [13, 14] conducted an experimental and an analytical research on eleven specimens of beam-column joints to investigate the shear resisting performance of joints in former RC frames before the 1970s. The study showed deterioration of the joint stiffness caused by damage and concluded that achieved story drifts by simulating joints joint like rigid nodes might be significantly less than real story drifts. Park et al. [15] tested a group of interior and exterior joints following NZS 3101. It was then said that joint shear strength could be improved by shifting locations of plastic hinge away from column faces.

With considerable interests of simulating joint nonlinear behaviors, various joint models have been proposed using different techniques to enhance computer efficiency and compatibility with other frame members [16]. El-Metwally and Chen [17] introduced a model adopting an inelastic rotational spring located between beams and columns to perform nonlinear characteristics as shown in Figure 1.1. The rotational spring carried the moment-rotation relationship and was generated by the thermodynamics of irreversible processes. Three parameters used to define this spring included: the initial linear rotational stiffness, the ultimate moment capacity, and the internal variable referring to the dissipated energy. Deterioration of bond strength and the hysteretic behavior of cracks at joint faces and frame members were considered to cause energy dissipated, and bond-slip curve by Morita and Kaku [18] was employed. The degradation of stiffness and joint strength related to shear loading were nonetheless not mentioned.
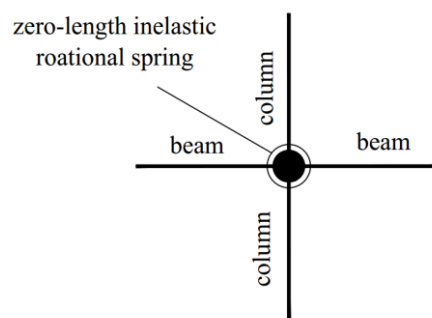
Figure 1.1 Nonlinear rotational spring model proposed by El-Metwally and Chen

Youssef and Ghobarah [19] suggested a model enclosing joint region by four rigid plates connecting to each other by pin constraint as denoted in Figure 1.2. The connection between frame members and rigid plates including three steel springs and three concrete springs represented concrete crushing and bond slip. These springs characterized groups of reinforcements and compressive concrete correspondingly, whereas shear response was modeled by shear springs. Concrete hysteresis rule proposed by Kent and Park [20] with a suggested transition from tension path to compression path was adopted for concrete springs [21]. Bond slip rule was derived from the model introduced by Giuriani et al. [22].

Lowes and Altoontash [23] proposed a multi-sping joint element as idealized in Figure 1.3. The model consisted of a shear panel, four zero length interface shear springs, and eight zero-length bar-slip springs. Stiffness and strength loss caused by shear failure were represented by shear

panel while the loss by anchorage degradation was modelled by bar-slip springs, degradation due to shear transfer related to cracks at joint faces was simulated by interface-shear springs. Constitutive rule for shear panel was derived from modified compressive field
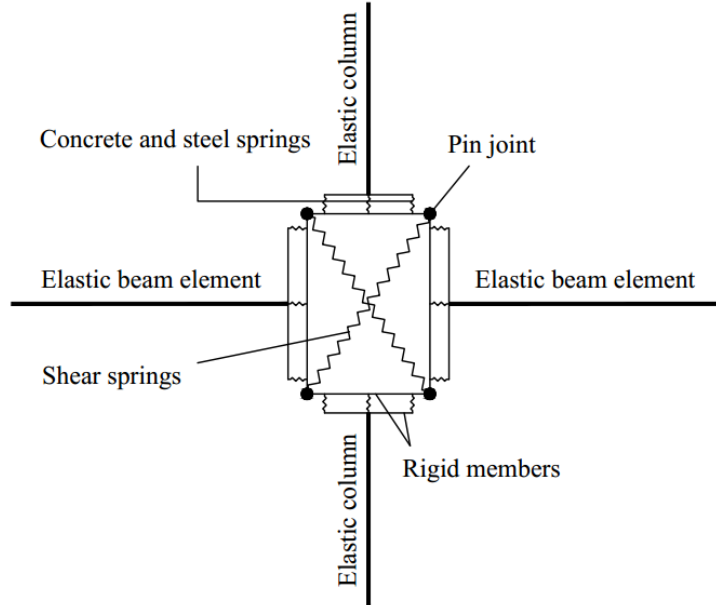
Figure 1.2 Joint model proposed by Youssef and Ghobarah
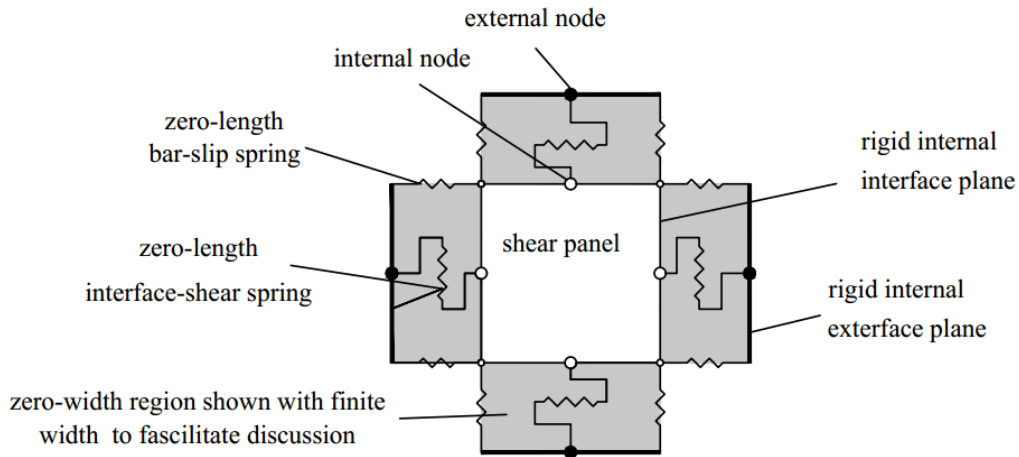
Figure 1.3 Joint model proposed by Lowes and Altoontash

theory proposed by Vecchio and Collins [24]. As for hysteresis rule of bond-slip behavior, a new bar-slip model was developed from experimental results based on previous models such as Eligehausen et al. [25], Viwathanatepa et al. [26], Shima et al. [27].

In fabricating beam-column joint models, theory with respect to joint shear damage is indispensable, and for many previous works, the strut and truss mechanism defined by Paulay et al. [28-30] have been preferable [31, 32] to explain the transferring action of shear force in a shear or moment resisting mechanism. This mechanism included a diagonal strut representing compressive concrete and horizontal and vertical ties representing reinforcements in the joint region. An equilibrium of forces was formed between the strut and ties, then when ties were tensioned to resist shear force, the strut was compressed and confinement in joint core occured. The failure of a joint was attributed to strut crushing or poor anchorage of ties, yielding of reinforcements. This mechanism exhibited advantages of consisting some material parameters for estimating the joint capacity such as concrete strength, amount of reinforcing bars, size of anchorage reinforcements in joint regions but fails to integrate the flexural strength of adjacent frame members. Shiohara pointed out an essential deficiency of this mechanism which was the lack of a parameter with respect to discriminating different joint types like interior, exterior and corner joints to determine the empirical allowable joint stress [33]. Moreover, by examining the result data of series of tests on the seismic behaviors of interior beam-column joints, it was found that joint shear and story shear were not proportional since story shear degraded but joint shear continued to develop till the end of tests [5]. The shear resisting capacity of joints was, therefore, considered to be reserved. The strut and truss model of Paulay could not explain well the foregoing aspects. Shiohara then proposed *joint shear hinging failure mechanism* with aspects of a moment resisting component which exhibited advantages in explaining the above behaviors successfully. Futhermore, a method derived from the mechanism to predict the joint moment capacity mathematically was also established.

Based on Shiohara mechanism, several beam-column joint models subjected to cyclic loading have been introduced. Tajiri et al. [9] proposed a 2D macro joint element used for elasto-plastic frames as denoted in Figure 1.4. The model was a four-node element with twelve degrees of freedom. Axial springs which connected to rigid plates at the joint perimeter were utilized to represent reinforcements, concrete, and bond-slip behavior. Modified model of Park et al. [34] was used to model concrete springs in plastic hinge regions of frame members and in the joint region. Hysteresis rule for steel springs was derived from the modified model suggested by Ramberg and Osgood [35]. Bond-slip behavior was simulated by rule introduced by Morita and Kaku [18].

5

Based on this element, Kusuhara et al. [10] introduced a joint model to apply for 2D interior and exterior joints with some changes in arranging springs as shown in Figure 1.5. Springs in the plastic hinge of beams and columns were not mentioned. Instead of those, three types of concrete springs were employed including vertical-, horizontal-, and diagonal orientation concrete springs. To model their behaviors, a constitutive rule on the basis of model proposed by Kent and Park [34] in which the tension path used the fracture energy theory of Nakamura [36]. Steel springs represented reinforcements and a bilinear rule was suggested for their performance, while bond-slip springs were located between two adjacent steel springs to simulate anchorage loss along longitudinal bars with bond-slip rule deriving from the model of Eligchausen [25] using skeleton suggested by CEB-FIP code [37].
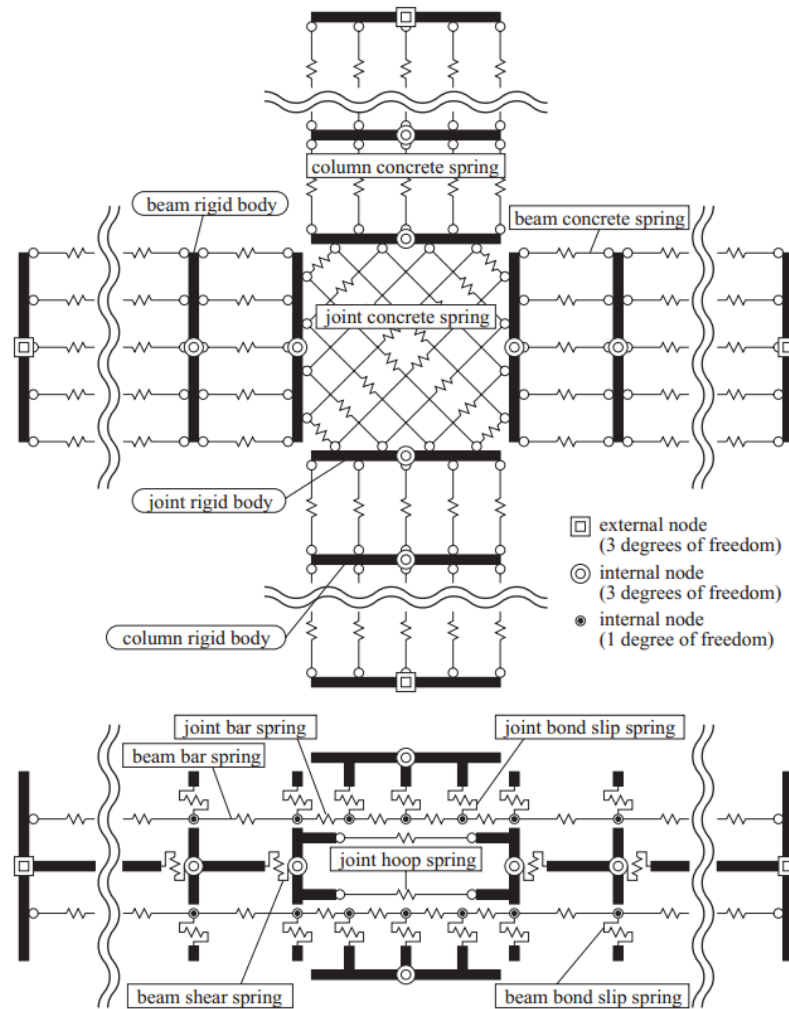
Figure 1.4 Model suggested by Tajiri, Shiohara, and Kusuhara
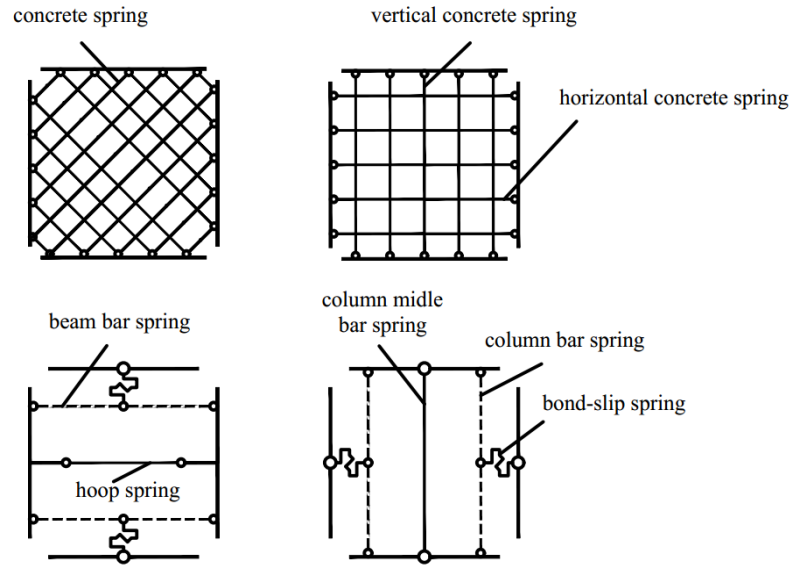
(a) Interior joint model
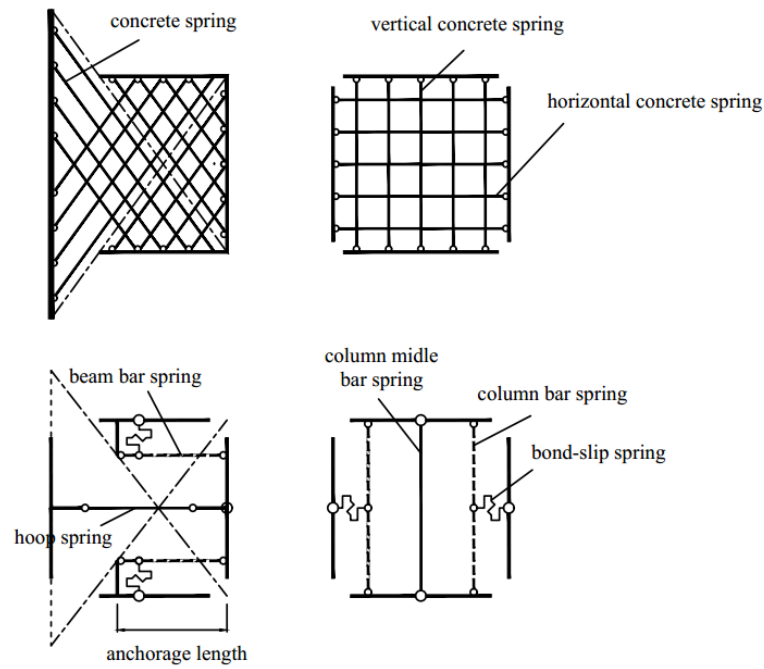
(b) Exterior joint model

Figure 1.5 Model proposed by Kusuhara and Shiohara

Kim et al. [11] developed Kusuhara model into a three dimensional (3D) form to simulate the cyclic response of slab-beam-column subassemblages under bi-lateral as described in
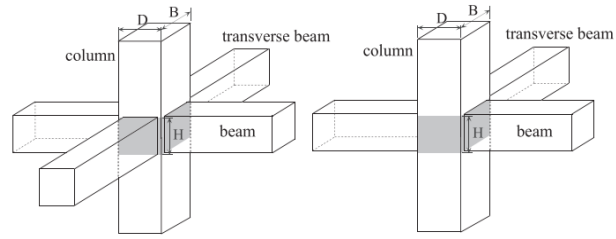
(a) 3D joint

(b) Concrete springs

(b) Longitudinal steel element and bond-slip spring

(c) Transverse steel element and slab steel element
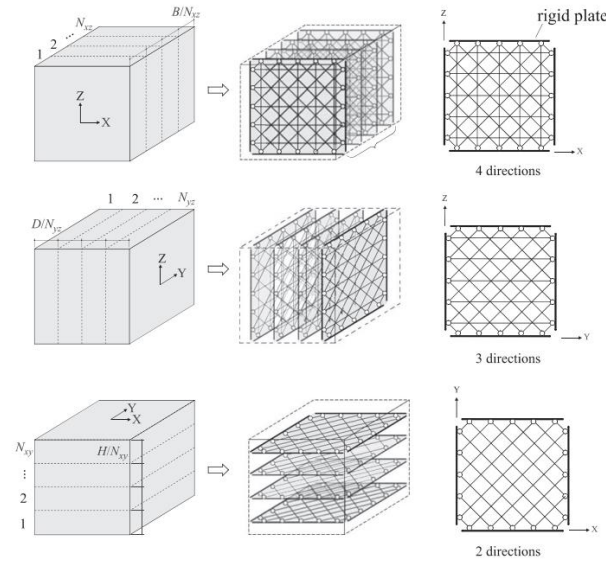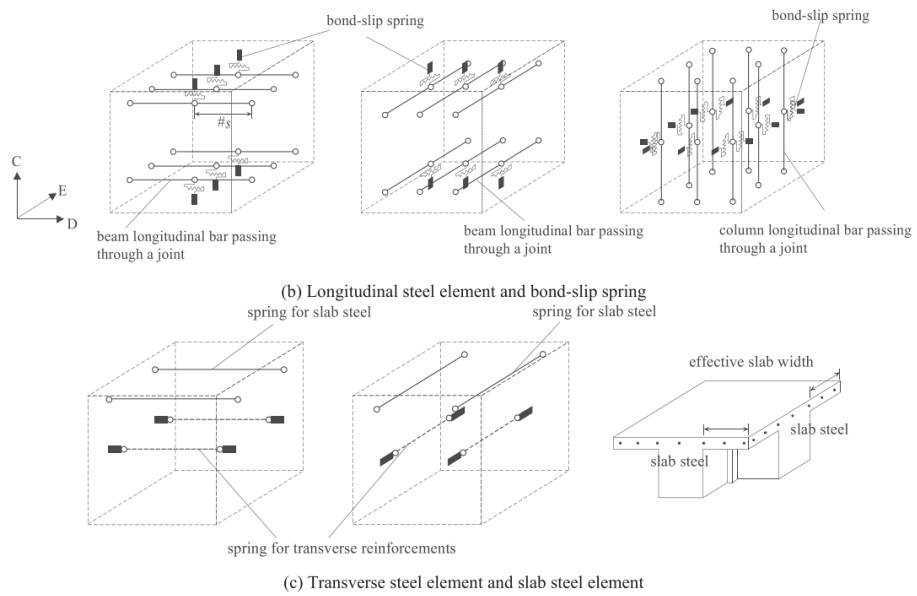
(c) Bond-slip springs

Figure 1.6 Model proposed by Kim, Kusuhara and Shiohara

8

Figure 1.6. The 3D joint model comprised six rigid plates connecting to each other by steel, bond-slip, and concrete springs. Verification was conducted by applying the joint element to simulate a slab-beam-column subassemblages under bidirectional loading [38].

Although three aforementioned joint models were based on Shiohara theory, they were developed from the basis of a multi-spring model. The joint model in this study tended to develop directly from Shiohara's mechanical model to reserve its aspects. For example, concrete was simulated by concrete struts to resemble compressive zone explained by the theory. Details of the new model and other explanations are described in the next Chapter.

1.4 Outline of dissertation

The main parts of this dissertation include three chapters which focus on proposing the new joint model, verification, and application. The next parts are organized as belows:

- Chapter 2 defines the new joint model for interior joints and verifies the joint analytical response with test data.
- Chapter 3 applies the model into cases of exterior joints with modifications, knee joints, and RC frame analysis.
- Chapter 4 suggests recommendations and future research.

Chapter 2 Suggestion of A New Beam-Column Joint Model and Application on Investigating Response of Interior Joints Under Lateral Loading

2.1 Abstract

A general model for simulating the response of the interior beam-column joints under lateral loading was presented in this chapter. The model is a two-dimensional macro-element developed from the theory of joint shear failure mechanism of Shiohara, which consists of four nodes with twelve degrees of freedom, and considers joint deformations as a combination of nine independent component deformations. The joint core was simulated by concrete struts while reinforcements were modeled by bar springs, and anchorage loss along longitudinal bars crossing joint body was represented by bond-slip springs. The study utilized constitutive models of concrete, steel, and bond-slip to characterize the performance of materials. A simple element for the interior joints in which the beams and columns have the same depth and width was introduced first. The monotonic response was established to capture the monotonic backbone of the cyclic response. Then, the calibration of the simple joint element was added so that it could be applied for general interior joints with the normal geometric properties subjected to cyclic loadings. Data from tests of interior joint sub-assemblages under cyclic loadings were employed to verify the analytical model. The result indicated its reliability in performing behaviors of interior beam-column connections developed from the shear failure theory.

2.2 Elastic stiffness of the beam-column joint element

Figure 2.1 shows the geometric properties of the joint element. A beam-to-column connection has four surfaces connecting to beams and columns. These are often modeled as line element, through the centers of those surfaces. The joint element is defined as a rectangular element with four nodes located at the center of the four rigid plates that represent the rigid bodies in SMM. d_x and d_z are the height and width of the joint. t is the joint thickness determined from the recommendation of AIJ 1999 [1]:

$$t = t_b + t_{c1} + t_{c2} \tag{2.1}$$

where t_b is beam width, t_{c1} and t_{c2} refer the smaller of ¼ column depth and ½ the distance between beam and column face on either side of beam.

Each node had three DOFs including one rotation and two translations. In the XZ plane coordinate, four nodes are named A, B, C, and D with 12 DOFs (u_A, v_A, θ_A, u_B, v_B, θ_B, u_C, v_C, θ_C, u_D, v_D, and θ_D) and 12 corresponding nodal forces (F_{xA}, F_{zA}, M_A, F_{xB}, F_{zB}, M_B, F_{xC}, F_{zC}, M_C, F_{xD}, F_{zD}, M_D). With this definition, the deformation of a joint model could be expressed as a combination of nine independent components; namely the four axial deformations (Δ_{x1}, Δ_{x2}, Δ_{z1}, and Δ_{z2}), four bending deformations (φ_{x1}, φ_{x2}, φ_{z1}, and φ_{z2}), and shear deformation φ_0. Complementary to this set of deformations were the nine independent internal forces, namely the four axial forces (N_{x1}, N_{x2}, N_{z1}, and N_{z2}), four bending moments (M_{x1}, M_{x2}, M_{z1}, and M_{z2}), and anti-symmetric bending moment (M_0).

Because of contragredience, there existed compatible relationships between the nine independent deformations of a joint and the 12 nodal displacements, and relationships between the 12 nodal forces and the nine internal forces. These relationships are expressed as follows:

$$\boldsymbol{\delta} = \mathbf{B}_0 \mathbf{e} \tag{2.2}$$

$$\mathbf{p} = \mathbf{B}_0^{\mathrm{T}} \mathbf{f} \tag{2.3}$$

$\boldsymbol{\delta}$ is the vector of the nine independent deformations of a joint element:

$$\boldsymbol{\delta} = \left\{ \Delta_{x1}, \Delta_{x2}, \Delta_{z1}, \Delta_{z2}, \varphi_{x1}, \varphi_{x2}, \varphi_{z1}, \varphi_{z2}, \varphi_O \right\} \tag{2.4}$$

e is the vector of the 12 nodal displacements:

$$\mathbf{e} = \left\{ u_A, v_A, q_A, u_B, v_B, q_B, u_C, v_C, q_C, u_D, v_D, q_D \right\} \tag{2.5}$$

p is the vector of the 12 joint nodal forces:

$$\mathbf{p} = \left\{ F_{xA}, F_{zA}, M_A, F_{xB}, F_{zB}, M_B, F_{xC}, F_{zC}, M_C, F_{xD}, F_{zD}, M_D \right\} \tag{2.6}$$

f is the vector of the nine joint internal forces:

$$\mathbf{f} = \left\{ N_{x1}, N_{x2}, N_{z1}, N_{z2}, M_{x1}, M_{x2}, M_{z1}, M_{z2}, M_O \right\} \tag{2.7}$$

(a) Joint dimension; (b) Joint deformations; (c) Joint internal forces
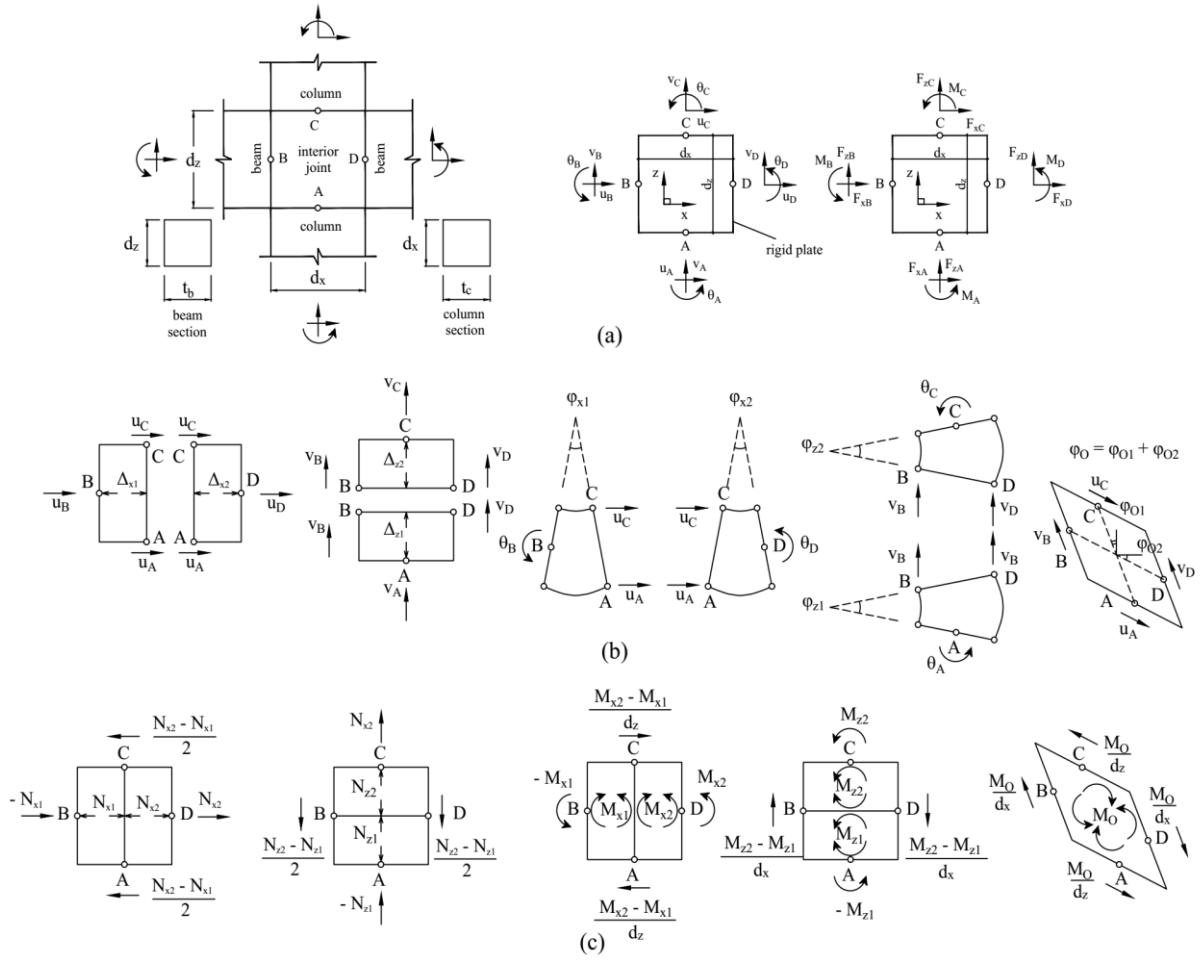
Figure 2.1. Geometric properties of the interior joint model

$\boldsymbol{B_0}$ is the compatibility matrix between $\boldsymbol{\delta}$ and $\mathbf{d}$:

$$\mathbf{B}_0 = \begin{bmatrix} 0.5 & 0 & 0 & -1 & 0 & 0 & 0.5 & 0 & 0 & 0 & 0 & 0 \\ -0.5 & 0 & 0 & 0 & 0 & 0 & -0.5 & 0 & 0 & 1 & 0 & 0 \\ 0 & -1 & 0 & 0 & 0.5 & 0 & 0 & 0 & 0 & 0 & 0.5 & 0 \\ 0 & 0 & 0 & 0 & -0.5 & 0 & 0 & 1 & 0 & 0 & -0.5 & 0 \\ \dfrac{1}{d_z} & 0 & 0 & 0 & 0 & -1 & -\dfrac{1}{d_z} & 0 & 0 & 0 & 0 & 0 \\ -\dfrac{1}{d_z} & 0 & 0 & 0 & 0 & 0 & \dfrac{1}{d_z} & 0 & 0 & 0 & 0 & 1 \\ 0 & 0 & -1 & 0 & -\dfrac{1}{d_x} & 0 & 0 & 0 & 0 & 0 & \dfrac{1}{d_x} & 0 \\ 0 & 0 & 0 & 0 & \dfrac{1}{d_x} & 0 & 0 & 0 & 1 & 0 & -\dfrac{1}{d_x} & 0 \\ \dfrac{1}{d_z} & 0 & 0 & 0 & \dfrac{1}{d_x} & 0 & -\dfrac{1}{d_z} & 0 & 0 & 0 & -\dfrac{1}{d_x} & 0 \end{bmatrix} \qquad (2.8)$$

The joint stiffness matrix **K** can be expressed by the relationship between the vector of the nodal forces **p** and the vector of the nodal displacements **d** as follows:

$$\mathbf{p} = \mathbf{K}\,\mathbf{e} \tag{2.9}$$

where

$$\mathbf{K} = \mathbf{B}_0^t\,\mathbf{k}_0\,\mathbf{B}_0 \tag{2.10}$$

$\mathbf{k}_0$ is the matrix consisting of the component stiffness corresponding to the nine independent deformations mentioned above.

If the joint response is considered to be elastic and the Poisson effect is neglected, $\mathbf{k}_0$ can be determined as follows:

$$\mathbf{k}_0 = \begin{bmatrix}
\dfrac{2td_zE_c}{d_x} & 0 & 0 & 0 & 0 & 0 & 0 & 0 & 0 \\
0 & \dfrac{2td_zE_c}{d_x} & 0 & 0 & 0 & 0 & 0 & 0 & 0 \\
0 & 0 & \dfrac{2td_xE_c}{d_z} & 0 & 0 & 0 & 0 & 0 & 0 \\
0 & 0 & 0 & \dfrac{2td_xE_c}{d_z} & 0 & 0 & 0 & 0 & 0 \\
0 & 0 & 0 & 0 & \dfrac{td_z^{\,3}E_c}{6d_x} & 0 & 0 & 0 & 0 \\
0 & 0 & 0 & 0 & 0 & \dfrac{td_z^{\,3}E_c}{6d_x} & 0 & 0 & 0 \\
0 & 0 & 0 & 0 & 0 & 0 & \dfrac{td_x^{\,3}E_c}{6d_z} & 0 & 0 \\
0 & 0 & 0 & 0 & 0 & 0 & 0 & \dfrac{td_x^{\,3}E_c}{6d_z} & 0 \\
0 & 0 & 0 & 0 & 0 & 0 & 0 & 0 & \dfrac{1}{\dfrac{d_z}{4td_x^{\,3}E_c}+\dfrac{d_x}{4td_z^{\,3}E_c}+\dfrac{\kappa}{td^2G}}
\end{bmatrix} \tag{2.11}$$

where E_c is the concrete modulus; G is the concrete shear modulus; $\kappa = 1.2$

Equation (2.10) mentions the elastic stiffness matrix of a joint element when deformation is small. When cracks occur, the joint nonlinear behavior is characterized by springs and struts, which represent materials, based on the basis of SMM.

2.3 Suggestion of a new model to investigate the monotonic response of the interior beam-column joints with an identical depth of beams and columns and perfect bond condition

2.3.1 Derivation from Shiohara's theory

At the beginning, Shiohara introduced joint hinging mechanism into RC beam-column interior connections [5, 33]. Based on joint behavior at the shear failure mode, the mechanism assumed that joint deformations were caused by rotation of four triangular rigid bodies respect to hinging points, as shown in Figure 2.2. These bodies attached to each other by reinforcing bars. On each bodies, there were equilibriums of forces regarding resultant compressive forces of concrete through hinging points, resultant forces in reinforcements and external forces. As shown in Figure 2.3, V_b, N_b, M_b, V_c, N_c,, and M_c refer external forces, T_1 to T_{10} refer resultant forces in reinforcements, C_1 to C_4 refer resultant compressive forces in concrete, $g_x d_x$ and $g_z d_z$ refer bar distances of columns and beams.
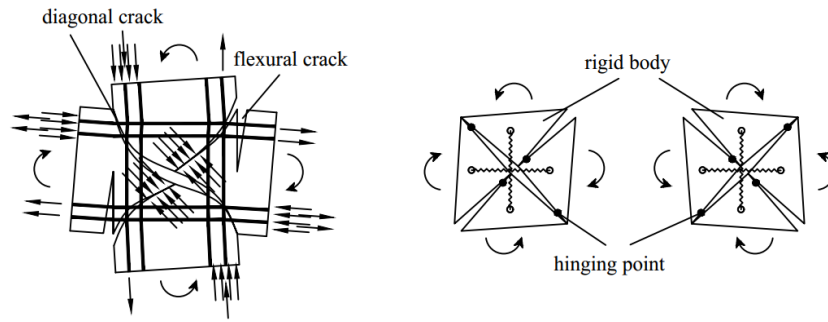
(a) Behavior of failure model   (b) Mechanical model including two failure modes

Figure 2.2 Shiohara mechanism

SMM was mentioned as a momment resisting mechanism. The relationship between the rotation of rigid free bodies, which represented for joint deformations, and the resultant forces in concrete and reinforcement is described in Figure 2.4. For concrete, the rotation of free bodies caused a linear distribution of deformation along the joint diagonal. A linear distribution of concrete strain on the diagonal was assumed corresponding to this deformation in which strain and deformation were considered to be those of two adjacent concrete struts with the same length. From the strain distribution, the stress distribution along the joint diagonal was also achiewed based on concrete constitutive rules. As a result, the resultant forces in concrete were determined. Similarly, the resultant forces in reinforcements were also computed from the rotation of free bodies in SMM.
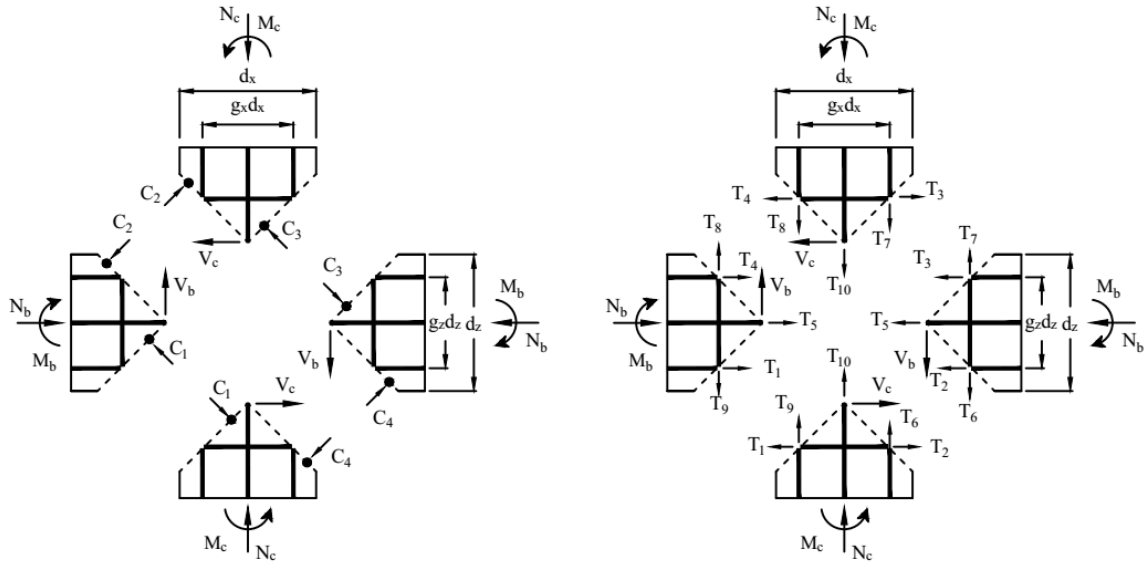
Figure 2.3 Forces applied on rigid bodies in Shiohara's mechanical model
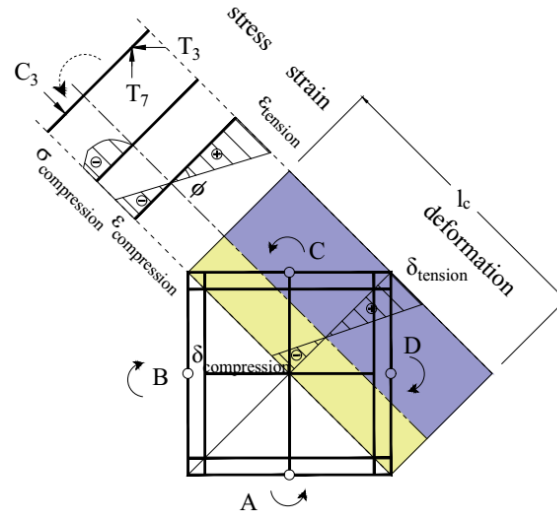
Figure 2.4 Relationship between rigid bodies' rotation and resultant forces in material

In this section, a 2D joint element developed directly from Shiohara's mechanical model [5] (SMM) in Figure 2.2 was proposed. Because SMM computed the strength of the joint moment resistance but did not consider the joint compatibility, this study defined the compatibility relationships of the joint to investigate the joint behaviors from the beginning of the loading to the failure stage. Bar springs and concrete struts were used to simulate the resultant forces in reinforcements and concrete applied to the four free bodies that was represented as rigid plates. The deformation of bar springs and concrete struts, on the other hand, were computed from the rotation of the four free bodies of SMM. This was the first time struts were employed to simulate

concrete in the joint core in SMM which was totally different from the previous multi-spring joint models [9-11]. The strain on the cross section of the struts was assumed to distributed linearly and determined from the rotation of the free bodies in SMM. The corresponding stress distribution was computed from the strain distribution through the constitutive concrete model.

In this section, the new joint model was introduced to investigate the joints in which the beams and columns have the same depth and width joints. This is also the scope discussed in SMM. Moreover, to reduce the complexity of explaining the computational procedure, the monotonic analysis was considered to capture the backbone curve of the joint cyclic behaviors. The comparison to the test data was carried out to verify the joint monotonic response.

2.3.2 Concrete struts

To analyze the expansion of the crack forming hinging mechanism, Shiohara [6] investigated the strain and stress state in the joint core from before cracking to after cracking and up to the ultimate state. Shiohara reported that the bi-axial stress state before cracking existed in both the tensile areas and compressive areas. After cracking, the stress state in the compressive areas became uniaxial. Moreover, stress did not exist in the tensile areas.

There were four compressive zones and four tensile zones at a loading stage due to the rotation of the free bodies, as shown in Figure 2.5(a). The four compressive zones represented the flow of the forces that transferred through concrete. In SMM, the inclination of these forces are 45° which is the same as the inclination of the diagonals. To determine the width of the compressive zones, the displacements of the joint center and the joint corners in the diagonal direction, which could be computed from the nine independent deformations mentioned in Equation (2.4), were interested.

In Figure 2.5(b), δ_{com_1}, δ_{com_2}, δ_{com_3}, δ_{com_4}, δ_{ten_5}, δ_{ten_6}, δ_{ten_7}, and δ_{ten_8} are the displacements of the joint center and the joint corners in the diagonal direction which are computed as follows:

$$\delta_{com\_1} = \frac{d}{\sqrt{2}} \left(\frac{\Delta_{x1}}{d} + \frac{\Delta_{z1}}{d} - \frac{\varphi_{x1}}{2} + \frac{\varphi_{z1}}{2} + \varphi_0 \right) \tag{2.12}$$

$$\delta_{com\_2} = \frac{2\Delta_{x1} + 2\Delta_{z2} - \varphi_{x1}d - \varphi_{z2}d}{2\sqrt{2}} \tag{2.13}$$

$$\delta_{com\_3} = \frac{d}{\sqrt{2}} \left(\frac{\Delta_{x2}}{d} + \frac{\Delta_{z2}}{d} + \frac{\varphi_{x2}}{2} - \frac{\varphi_{z2}}{2} + \varphi_0 \right) \tag{2.14}$$

16

$$\delta_{com\_4} = \frac{2\Delta_{x2} + 2\Delta_{z1} + \varphi_{x2}d + \varphi_{z1}d}{2\sqrt{2}} \tag{2.15}$$

$$\delta_{ten\_5} = \frac{2\Delta_{x1} + 2\Delta_{z2} + \varphi_{x1}d + \varphi_{z2}d - 2\varphi_0 d}{2\sqrt{2}} \tag{2.16}$$

$$\delta_{ten\_6} = \frac{d}{\sqrt{2}}\left(\frac{\Delta_{x1}}{d} + \frac{\Delta_{z1}}{d} + \frac{\varphi_{x1}}{2} - \frac{\varphi_{z1}}{2}\right) \tag{2.17}$$

$$\delta_{ten\_7} = \frac{2\Delta_{x2} + 2\Delta_{z1} - \varphi_{x2}d - \varphi_{z1}d - 2\varphi_0 d}{2\sqrt{2}} \tag{2.18}$$

$$\delta_{ten\_8} = \frac{d}{\sqrt{2}}\left(\frac{\Delta_{x2}}{d} + \frac{\Delta_{z2}}{d} - \frac{\varphi_{x2}}{2} + \frac{\varphi_{z2}}{2}\right) \tag{2.19}$$

The displacements in the inclination of 45° of the points on the diagonals changed linearly from the joint center to the joint corners. The points with zero displacement separated each half of the joint diagonals into the compressive zone and tensile zone in the concrete. In the present study, the concrete strain was also assumed to distribute linearly on the joint diagonals in which the point with zero strain was the same with the point with zero displacement, as shown in Figure 2.5(c). The joint concrete core was considered to consist eight concrete struts, namely C_1 to C_8 as shown in Figure 2.5(d), so that the above distribution of strain was also that of the strut sections. The strut width was the same with the distributed width on the diagonals of the corresponding tensile strain or compressive strain, namely w_{C1} to w_{C8}. The four concrete struts corresponding to the tensile strain zone might not carry force. The name "strut" was still used to define to them because they might carry the compressive forces in other stages. For example, in the beginning of the loading the struts were compressed due to the axial force in the columns but the compressive force in these struts disappeared when the free bodies rotated. Before cracking, the joint was considered to be an elastic solid element. After cracking, springs and struts were used to characterize the joint behaviors. The orientation of the struts was assumed to be 45° at any stage after cracking.

In Figure 2.5(a), the concrete compressive forces distributed along the joint diagonals. Thus, the length of the concrete struts near the joint diagonals was assigned to be the same with the length of the joint diagonals. Because the strain of a point on the joint diagonal was considered to be the ratio of its displacement to the length of the strut where it was located, the length of two adjacent struts must be identical to satisfy that the point with zero displacement did not have strain. Therefore, the length of the struts near the corners was also equal to the diagonal

length. To this end, the eight struts had the same length (l_C). Note that the length of the struts near the corners was not necessarily as short as the length of the compressive zones in Figure 2.5(a) but needed to satisfy the distribution of the displacement and strain discussed above. Moreover, if the strut near the corners was short, a small rotation of the free bodies might result in the great strain in the strut which was irrational because in practical, the amount of the concrete length extended to beams and columns must be considered.

Figure 2.5(e) shows a typical strain distribution in the half-length of a diagonal with strut i in compression and strut j in tension. The strain at the compression end (ε_{com_i}) and the strain at the tension end (ε_{ten_j}) were calculated as follows:

$$\varepsilon_{com\_i} = \frac{\delta_{com\_i}}{l_C} \tag{2.20}$$

$$\varepsilon_{ten\_j} = \frac{\delta_{ten\_j}}{l_C} \tag{2.21}$$

In Figure 2.5(e)., coefficient ξ_i and ξ_j used to determine the width of strut i (w_{Ci}) and strut j (w_{Cj}) were computed respectively as follows:

$$\xi_i = \frac{\left|\varepsilon_{com\_i}\right|}{\left|\varepsilon_{com\_i}\right| + \left|\varepsilon_{ten\_j}\right|} \tag{2.22}$$

$$\xi_j = 1 - \xi_i \tag{2.23}$$

Then:

$$w_{Ci} = \xi_i \frac{l_C}{2} \tag{2.24}$$

$$w_{Cj} = \xi_j \frac{l_C}{2} \tag{2.25}$$

These widths were employed to calculate the struts' cross-sectional areas (A_{Ci} and A_{Cj}) as follows:

$$A_{Ci} = w_{Ci}t \tag{2.26}$$

$$A_{Cj} = w_{Cj}t \tag{2.27}$$

σ_{Ci} and σ_{Cj} which are in turn the average stresses of strut i in compression and strut j in tension respectively, can be expressed as follows:

$$\sigma_{Ci} = \frac{\int_0^{\varepsilon_{com\_i}} \sigma_{(\varepsilon)} d\varepsilon}{\varepsilon_{com\_i}} \qquad (2.28)$$

$$\sigma_{Cj} = \frac{\int_0^{\varepsilon_{ten\_j}} \sigma_{(\varepsilon)} d\varepsilon}{\varepsilon_{\varepsilon_{ten\_j}}} \qquad (2.29)$$

where $\sigma_{(\varepsilon)}$ is the strain's envelope stress function.

Location of strut axial forces is computed by distances between them and corner points for struts near corners or the joint center for others near the center and are governed by coefficient β_1 to β_8, as shown in Figure 2.5(f). These coefficients were calculated as follows:

$$\beta_i = \xi_i \left(1 - \frac{\int_0^{\varepsilon_{com\_i}} \varepsilon\sigma_{(\varepsilon)} d\varepsilon}{\varepsilon_{com\_i} \int_0^{\varepsilon_{com\_i}} \sigma_{(\varepsilon)} d\varepsilon} \right) \quad with\ i = 1\ to\ 8 \qquad (2.30)$$

$$\beta_j = \xi_j \left(1 - \frac{\int_0^{\varepsilon_{ten\_j}} \varepsilon\sigma_{(\varepsilon)} d\varepsilon}{\varepsilon_{ten\_j} \int_0^{\varepsilon_{ten\_j}} \sigma_{(\varepsilon)} d\varepsilon} \right) \quad with\ j = 1\ to\ 8 \qquad (2.31)$$

Note that in Equation. (2.28) to Equation.(2.31), σ_{Ci}, σ_{Cj}, β_i, and β_j are considered to be zero if ε_{com_i} or ε_{ten_j} reaches zero.

The arrangement of the struts attached to the rigid plates are also shown in Figure 2.5(f).
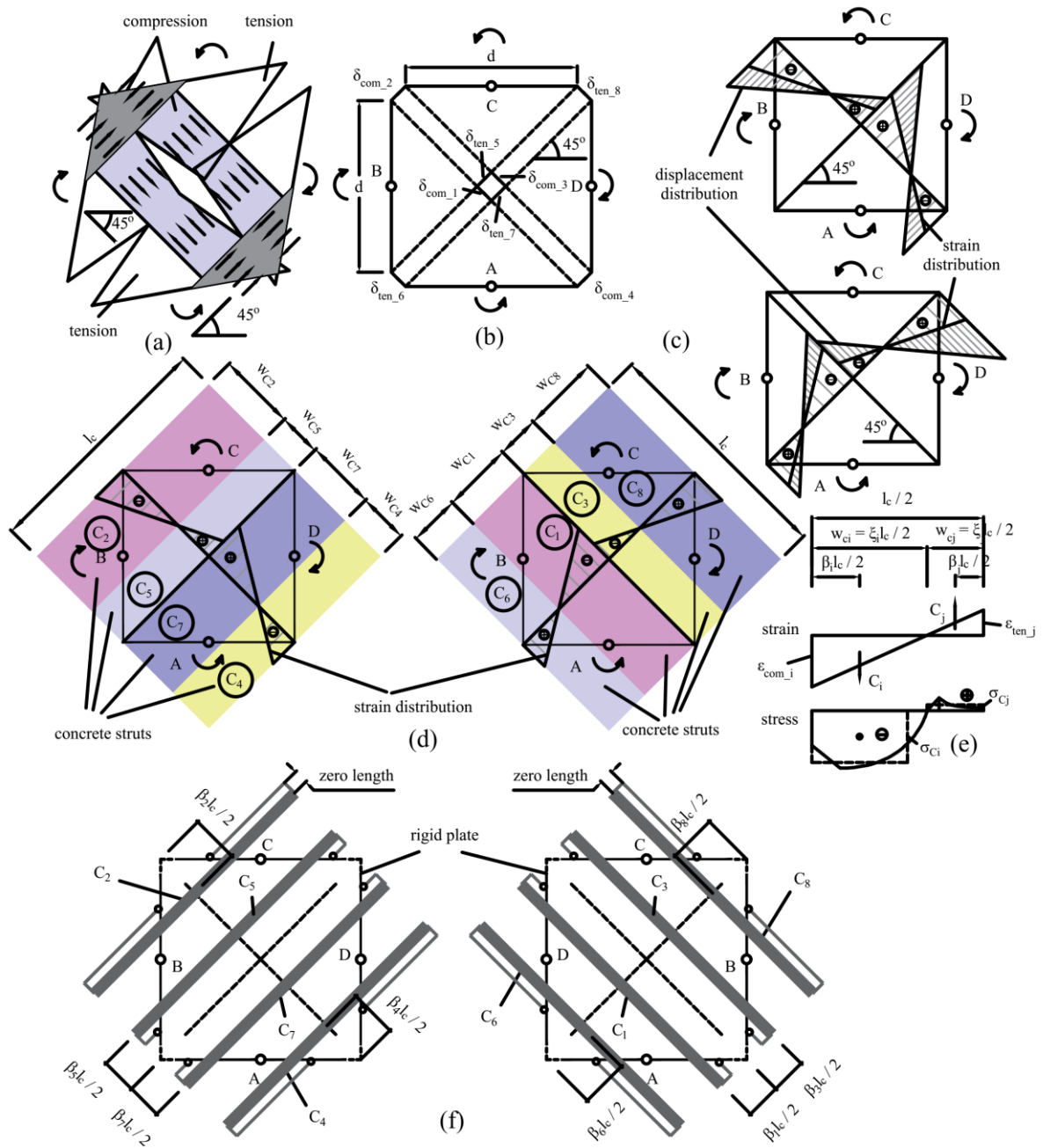
(a) Tensile zone and compressive zone in concrete; (b) Displacement of the center point and corner points in the inclination of 45°; (c) Displacement and strain distribution on the joint diagonals in the inclination of 45°; (d) Illustration of concrete strain distribution and the width of the struts; (e) Typical stress distribution on a half of joint diagonals; (f) Connection of concrete struts to rigid plates;

Figure 2.5. Definition of concrete struts in the new interior joint element

2.3.3 Bar springs

The rotation of the four rigid plates simulated the rotation of the four free bodies of SMM. When the rigid plates rotated, there were following displacements (Δ_{T1}, Δ_{T2}, Δ_{T3}, Δ_{T4}, Δ_{T5}, Δ_{T6}, Δ_{T7}, Δ_{T8}, Δ_{T9}, Δ_{T10}) at the location of the reinforcements, as shown in Figure 2.6.
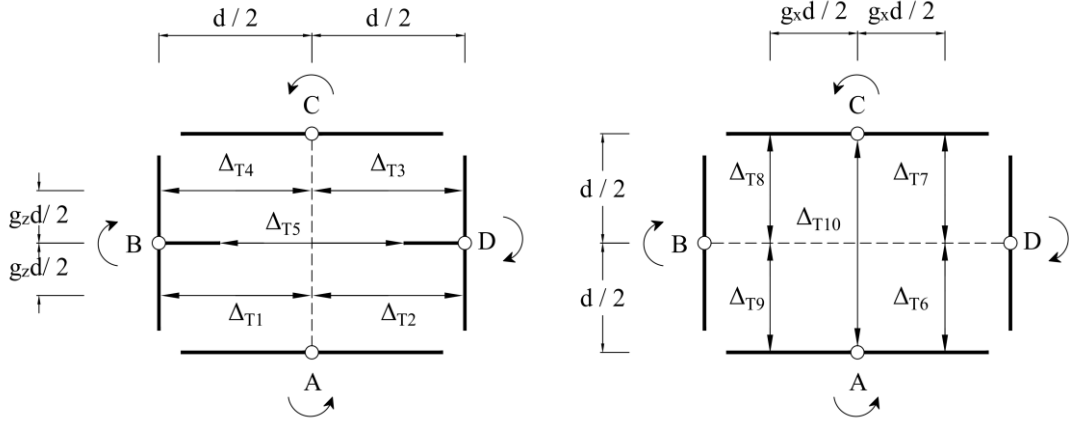
Figure 2.6. Deformation at the location of reinforcements in the new interior joint model

These displacements could be computed by nine independent components of the joint deformations as follows:

$$\Delta_{T1} = \Delta_{x1} + \frac{g_z d\varphi_{x1}}{2} + \frac{(1-g_z)d\varphi_{z1}}{2} + \frac{(1-g_z)d\varphi_0}{2} \tag{2.32}$$

$$\Delta_{T2} = \Delta_{x2} + \frac{g_z d\varphi_{x2}}{2} - \frac{(1-g_z)d\varphi_{z1}}{2} - \frac{(1-g_z)d\varphi_0}{2} \tag{2.33}$$

$$\Delta_{T3} = \Delta_{x2} - \frac{g_z d\varphi_{x2}}{2} - \frac{(1-g_z)d\varphi_{z2}}{2} + \frac{(1-g_z)d\varphi_0}{2} \tag{2.34}$$

$$\Delta_{T4} = \Delta_{x1} - \frac{g_z d\varphi_{x1}}{2} + \frac{(1-g_z)d\varphi_{z2}}{2} - \frac{(1-g_z)d\varphi_0}{2} \tag{2.35}$$

$$\Delta_{T5} = \Delta_{x1} + \Delta_{x2} \tag{2.36}$$

$$\Delta_{T6} = \Delta_{z1} + \frac{g_x d\varphi_{z1}}{2} - \frac{(1-g_x)d\varphi_{x2}}{2} - \frac{(1-g_x)d\varphi_0}{2} \tag{2.37}$$

$$\Delta_{T7} = \Delta_{z2} + \frac{g_x d\varphi_{z2}}{2} + \frac{(1-g_x)d\varphi_{x2}}{2} + \frac{(1-g_x)d\varphi_0}{2} \tag{2.38}$$

21

$$\Delta_{T8} = \Delta_{z2} - \frac{g_x d\varphi_{z2}}{2} + \frac{(1-g_x)d\varphi_{x1}}{2} - \frac{(1-g_x)d\varphi_0}{2} \tag{2.39}$$

$$\Delta_{T9} = \Delta_{z1} - \frac{g_x d\varphi_{z1}}{2} - \frac{(1-g_x)d\varphi_{x1}}{2} + \frac{(1-g_x)d\varphi_0}{2} \tag{2.40}$$

$$\Delta_{T10} = \Delta_{z1} + \Delta_{z2} \tag{2.41}$$

In this section, bar springs were defined based on these displacements to represent reinforcements in joint core. Notation T_1 to T_{10} were also utilized for their names, and their axial forces refer resultant forces of reinforcing bars in SMM, as shown in Figure 2.7 and Figure 2.8 while their deformations were assigned by Δ_{T1} to Δ_{T10} respectively with the assumption of perfect bond condition.

Lengths of bar springs were defined as follows:

$$l_{T1} = l_{T2} = l_{T3} = l_{T4} = l_{T6} = l_{T7} = l_{T8} = l_{T9} = \frac{d}{2} \tag{2.42}$$

$$l_{T5} = g_x d \tag{2.43}$$

$$l_{T10} = d \tag{2.44}$$

where l_{T1}, l_{T2}, l_{T3}, l_{T4}, l_{T5}, l_{T6}, l_{T7}, l_{T8}, l_{T9}, and l_{T10} are length of bar spring T_1, T_2, T_3, T_4, T_5, T_6, T_7, T_8, T_9, and T_{10} respectively.
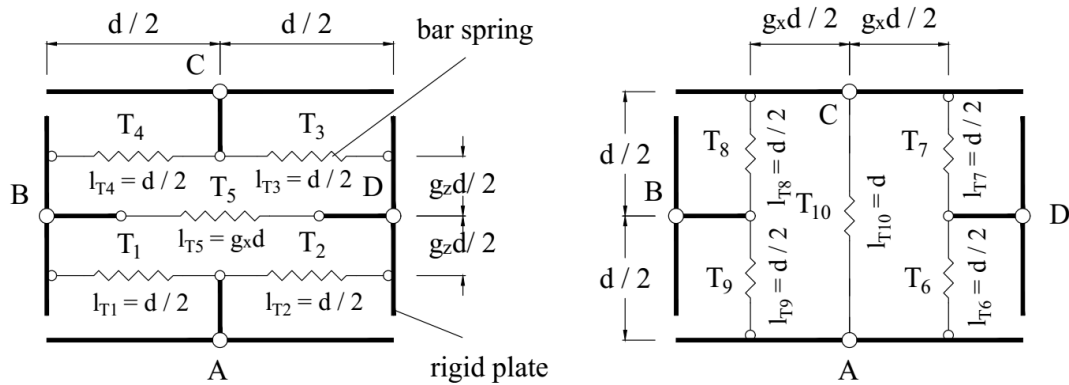
Figure 2.7. Definition of bar springs in the new interior joint model

22
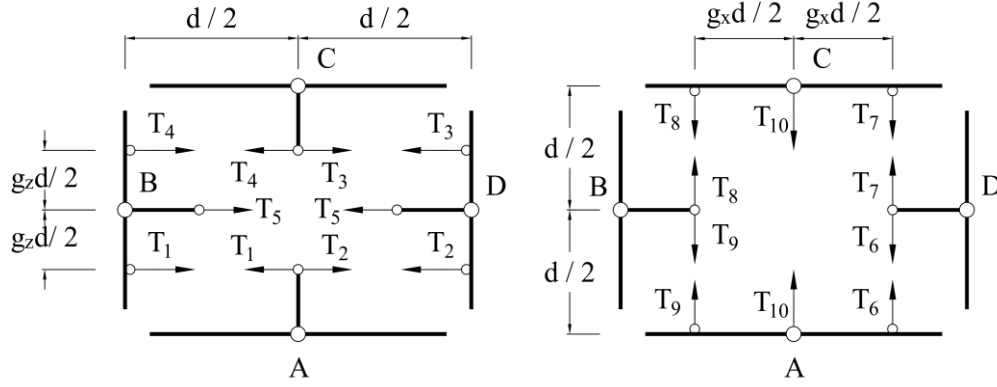
Figure 2.8. Axial forces of bar springs in the new interior joint model

2.3.4 Joint compatibility and stiffness

2.3.4.1 Before cracking

The joint behavior before cracking was assumed to be elastic. The joint stiffness was computed by Equation (2.10).

2.3.4.2 After cracking

Cracks were considered to occur when any tensile displacements in Equation (2.16) to Equation (2.19) exceeded the crack width as follows:

$$\delta_{ten\_i} > \varepsilon_t l_c \qquad with\ i = 5\ to\ 8 \tag{2.45}$$

where ε_t is the strain at tensile strength of concrete.

After cracking, properties of struts and springs were included in the joint stiffness. There was a compatibility between vector Δ, which included the average deformations of the concrete struts and the deformations of the bar springs with the vector of the nine independent joint deformations $\boldsymbol{\delta}$ as follows:

$$\boldsymbol{\Delta} = \mathbf{B_1}\boldsymbol{\delta} \tag{2.46}$$

where

$$\Delta = \left\{ \Delta_{C_1}, \Delta_{C_2}, ..., \Delta_{C_7}, \Delta_{C_8}, \Delta_{T_1}, \Delta_{T_2}, ..., \Delta_{T_5}, ..., \Delta_{T_9}, \Delta_{T_{10}} \right\} \tag{2.47}$$

In Equation (2.47) Δ_{C1} to Δ_{C8} are the average deformations of the corresponding concrete struts.

23

Because of contragredience, the vector of the nine joint forces $\mathbf{f}$ could be determined from the vector comprising the axial forces of the concrete struts and bar springs $\mathbf{q}$, as follows:

$$\mathbf{f} = \mathbf{B_1^T q} \tag{2.48}$$

where

$$\mathbf{q} = \left\{ C_1, C_2, C_3, C_4, C_5, C_6, C_7, C_8, T_1, T_2, T_3, T_4, T_5, T_6, T_7, T_8, T_9, T_{10} \right\} \tag{2.49}$$

and $\mathbf{B_1}$ is the compatibility matrix between Δ and $\boldsymbol{\delta}$:

$$\mathbf{B_1} = \begin{bmatrix}
\frac{1}{\sqrt{2}} & 0 & \frac{1}{\sqrt{2}} & 0 & -\left(\frac{1}{2}-\beta_1\right)\frac{d}{\sqrt{2}} & 0 & \left(\frac{1}{2}-\beta_1\right)\frac{d}{\sqrt{2}} & 0 & (1-\beta_1)\frac{d}{\sqrt{2}} \\
\frac{1}{\sqrt{2}} & 0 & 0 & \frac{1}{\sqrt{2}} & -\left(\frac{1}{2}-\beta_2\right)\frac{d}{\sqrt{2}} & 0 & 0 & -\left(\frac{1}{2}-\beta_2\right)\frac{d}{\sqrt{2}} & -\beta_2\frac{d}{\sqrt{2}} \\
0 & \frac{1}{\sqrt{2}} & 0 & \frac{1}{\sqrt{2}} & 0 & \left(\frac{1}{2}-\beta_3\right)\frac{d}{\sqrt{2}} & 0 & -\left(\frac{1}{2}-\beta_3\right)\frac{d}{\sqrt{2}} & (1-\beta_3)\frac{d}{\sqrt{2}} \\
0 & \frac{1}{\sqrt{2}} & \frac{1}{\sqrt{2}} & 0 & 0 & \left(\frac{1}{2}-\beta_4\right)\frac{d}{\sqrt{2}} & \left(\frac{1}{2}-\beta_4\right)\frac{d}{\sqrt{2}} & 0 & -\beta_4\frac{d}{\sqrt{2}} \\
\frac{1}{\sqrt{2}} & 0 & 0 & \frac{1}{\sqrt{2}} & \left(\frac{1}{2}-\beta_5\right)\frac{d}{\sqrt{2}} & 0 & 0 & \left(\frac{1}{2}-\beta_5\right)\frac{d}{\sqrt{2}} & -(1-\beta_5)\frac{d}{\sqrt{2}} \\
\frac{1}{\sqrt{2}} & 0 & \frac{1}{\sqrt{2}} & 0 & \left(\frac{1}{2}-\beta_6\right)\frac{d}{\sqrt{2}} & 0 & -\left(\frac{1}{2}-\beta_6\right)\frac{d}{\sqrt{2}} & 0 & \beta_6\frac{d}{\sqrt{2}} \\
0 & \frac{1}{\sqrt{2}} & \frac{1}{\sqrt{2}} & 0 & 0 & -\left(\frac{1}{2}-\beta_7\right)\frac{d}{\sqrt{2}} & -\left(\frac{1}{2}-\beta_7\right)\frac{d}{\sqrt{2}} & 0 & -(1-\beta_7)\frac{d}{\sqrt{2}} \\
0 & \frac{1}{\sqrt{2}} & 0 & \frac{1}{\sqrt{2}} & 0 & -\left(\frac{1}{2}-\beta_8\right)\frac{d}{\sqrt{2}} & 0 & \left(\frac{1}{2}-\beta_8\right)\frac{d}{\sqrt{2}} & \beta_8\frac{d}{\sqrt{2}} \\
1 & 0 & 0 & 0 & \frac{g_z d}{2} & 0 & \frac{(1-g_z)d}{2} & 0 & \frac{(1-g_z)d}{2} \\
0 & 1 & 0 & 0 & 0 & \frac{g_z d}{2} & -\frac{(1-g_z)d}{2} & 0 & -\frac{(1-g_z)d}{2} \\
0 & 1 & 0 & 0 & 0 & -\frac{g_z d}{2} & 0 & -\frac{(1-g_z)d}{2} & \frac{(1-g_z)d}{2} \\
1 & 0 & 0 & 0 & -\frac{g_z d}{2} & 0 & 0 & \frac{(1-g_z)d}{2} & -\frac{(1-g_z)d}{2} \\
1 & 1 & 0 & 0 & 0 & 0 & 0 & 0 & 0 \\
0 & 0 & 1 & 0 & 0 & -\frac{(1-g_x)d}{2} & \frac{g_x d}{2} & 0 & -\frac{(1-g_x)d}{2} \\
0 & 0 & 0 & 1 & 0 & \frac{(1-g_x)d}{2} & 0 & \frac{g_x d}{2} & \frac{(1-g_x)d}{2} \\
0 & 0 & 0 & 1 & \frac{(1-g_x)d}{2} & 0 & 0 & -\frac{g_x d}{2} & -\frac{(1-g_x)d}{2} \\
0 & 0 & 1 & 0 & -\frac{(1-g_x)d}{2} & 0 & -\frac{g_x d}{2} & 0 & \frac{(1-g_x)d}{2} \\
0 & 0 & 1 & 1 & 0 & 0 & 0 & 0 & 0
\end{bmatrix} \tag{2.50}$$

The stiffness matrix $\mathbf{k_0}$ in Equation (2.10) was expressed as follows:

$$\mathbf{k_0} = \mathbf{B_1^t\, k_1\, B_1} \tag{2.51}$$

$\mathbf{k_1}$ is the component stiffness matrix of concrete struts and bar springs:

$$\mathbf{k}_1 = \begin{bmatrix} \mathbf{k_C} & 0 \\ 0 & \mathbf{k_T} \end{bmatrix} \tag{2.52}$$

In the above equation, $\mathbf{k_C}$ and $\mathbf{k_T}$ is the diagonal stiffness matrix of concrete struts and springs respectively. Components of $\mathbf{k_C}$ was defined as follows:

$$k_{Ci} = \frac{C_i^n - C_i^{n-1}}{\Delta_{Ci}^n - \Delta_{Ci}^{n-1}} \quad (i = 1 \div 8) \tag{2.53}$$

where C_i^n, Δ_{Ci}^n, C_i^{n-1}, and Δ_{Ci}^{n-1} are the axial forces and average deformations of strut C_i and strut C_j at step n and step $n-1$ respectively. Δ_i^n and Δ_i^{n-1} are defined as follows:

$$\Delta_{Ci}^n = \frac{\xi_i - \beta_i}{\xi_i} \delta_{com\_i} \tag{2.54}$$

$$\Delta_{Cj}^n = \frac{\xi_j - \beta_j}{\xi_j} \delta_{ten\_j} \tag{2.55}$$

In the initial cracking, the width of the concrete struts is assigned as follows:

$$w_{Ci} = \frac{l_C}{4} \quad (i = 1 \div 8) \tag{2.56}$$

The initial stiffness of the struts is computed as:

$$k_{Ci} = \frac{E_c A_{ci}}{l_c} \quad (i = 1 \div 8) \tag{2.57}$$

where E_c is the modulus of concrete.

Finally, Equation (2.10) becomes:

$$\mathbf{K} = \mathbf{B_0^t} \mathbf{B_1^t} \mathbf{k}_1 \mathbf{B_1} \mathbf{B_0} \tag{2.58}$$

2.3.5 Orientation and length of concrete struts

Before cracking, the joint element was considered to be elastic and the elastic stiffness was used to investigate joint behaviors. After cracking, struts and springs were used to define the joint

nonlinear stiffness. At the ultimate stage, the orientation of struts was 45° according to SMM. From the end of the elastic stage till the ultimate stage, it was necessary to define struts' angle. In this study, it was assumed that struts' angle was also 45° from cracking till the failure point. To verify this assumption, the below part introduces an analytical study on the influence of struts' angle to the joint performance in the vicinity of stages after cracking.

Several joint elements with following aspects were considered for analysis:

- Joints have the same width d_x
- For each joint, a case of strut in diagonal direction and a case of strut in 45° were studied
- A normal compressive stress (σ) and a shear stress (τ) were applied with $r = \sigma/\tau = const$ during loading. Four cases were included: $r = 0, 1, 2,$ and 10

The stress state of a typical joint element and struts' angle are shown in Figure 2.9 and Figure 2.10.

The angle (θ) regarding the orientation of diagonals had a relationship with the stress ratio (r) as follows:

$$\tan 2\theta = \frac{2\tau}{\sigma} \tag{2.59}$$

or

$$\theta = \arctan\frac{d_x}{d_z} = \arctan\left(-\frac{\sigma}{2\tau} + \sqrt{\left(\frac{\sigma}{2\tau}\right)^2 + 1}\right) \tag{2.60}$$
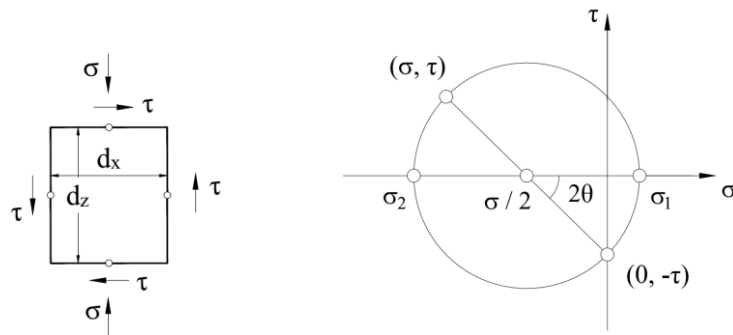
Figure 2.9. Stress state of the joint element and Mohr circle
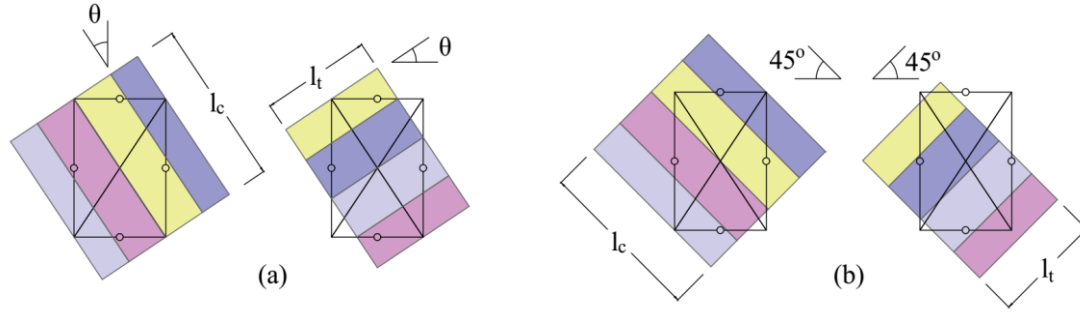
(a) In diagonal direction; (b) In 45°

Figure 2.10. Orientation of concrete struts
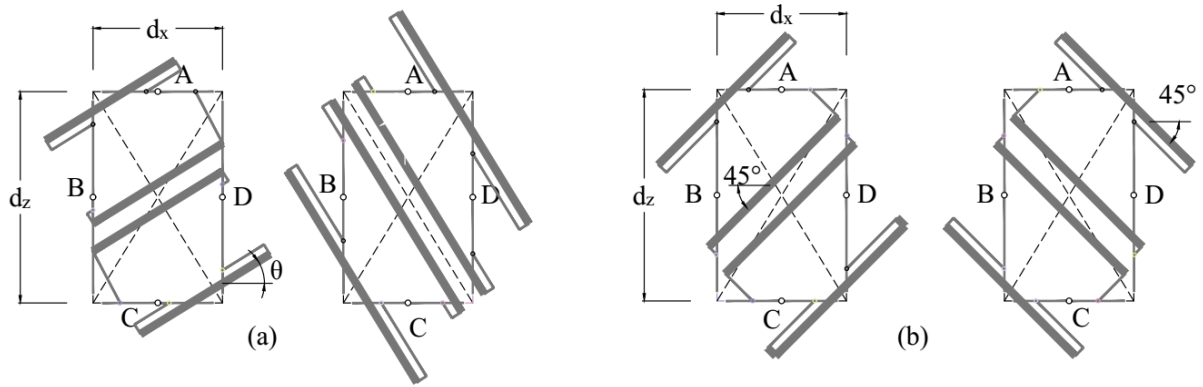
(a) In diagonal direction; (b) In 45°

Figure 2.11. Two computational cases for struts' orientation

Before analysis, it was needed to determine the length of concrete struts. The struts' length was chosen so that the stress state in the elastic state was reserved. A set of joint nodal displacements in Figure 2.12 was used to form the plane stress state in Figure 2.9.

$$u_A = v_A = \theta_A = \theta_C = 0$$
$$v_C = -r|u_C|$$
$$u_B = u_D = |u_C| / 2$$
$$v_B = v_D = v_C / 2$$
$$\theta_B = \theta_D = -|u_C| / d_z$$
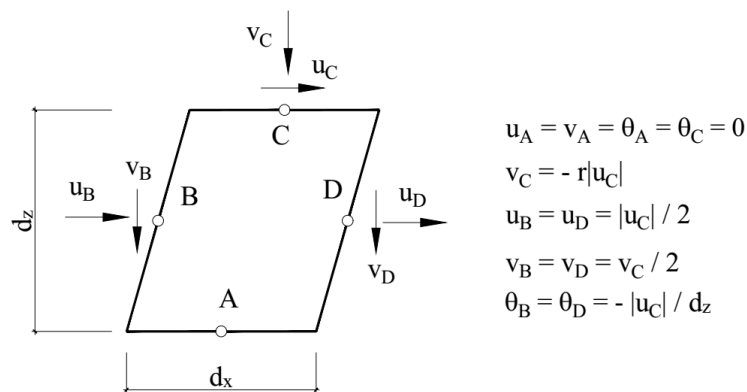
Figure 2.12. Nodal displacements of the simple plane stress state

The vector of joint deformations in Equation (2.2) was computed as belows:

$$
\begin{Bmatrix} \Delta_{x1} \\ \Delta_{x2} \\ \Delta_{z1} \\ \Delta_{z2} \\ \varphi_{x1} \\ \varphi_{x2} \\ \varphi_{z1} \\ \varphi_{z2} \\ \varphi_{0} \end{Bmatrix} =
\begin{bmatrix}
0.5 & 0 & 0 & -1 & 0 & 0 & 0.5 & 0 & 0 & 0 & 0 & 0 \\
-0.5 & 0 & 0 & 0 & 0 & 0 & -0.5 & 0 & 0 & 1 & 0 & 0 \\
0 & -1 & 0 & 0 & 0.5 & 0 & 0 & 0 & 0 & 0 & 0.5 & 0 \\
0 & 0 & 0 & 0 & -0.5 & 0 & 0 & 1 & 0 & 0 & -0.5 & 0 \\
\dfrac{1}{d_z} & 0 & 0 & 0 & 0 & -1 & -\dfrac{1}{d_z} & 0 & 0 & 0 & 0 & 0 \\
-\dfrac{1}{d_z} & 0 & 0 & 0 & 0 & 0 & \dfrac{1}{d_z} & 0 & 0 & 0 & 0 & 1 \\
0 & 0 & -1 & 0 & -\dfrac{1}{d_x} & 0 & 0 & 0 & 0 & 0 & \dfrac{1}{d_x} & 0 \\
0 & 0 & 0 & 0 & \dfrac{1}{d_x} & 0 & 0 & 0 & 1 & 0 & -\dfrac{1}{d_x} & 0 \\
\dfrac{1}{d_z} & 0 & 0 & 0 & \dfrac{1}{d_x} & 0 & -\dfrac{1}{d_z} & 0 & 0 & 0 & -\dfrac{1}{d_x} & 0
\end{bmatrix}
\begin{Bmatrix} u_A \\ v_A \\ \theta_A \\ u_B \\ v_B \\ \theta_B \\ u_C \\ v_C \\ \theta_C \\ u_D \\ v_D \\ \theta_D \end{Bmatrix} =
\begin{Bmatrix} 0 \\ 0 \\ 0 \\ -\dfrac{r|u_C|}{2} \\ -\dfrac{r|u_C|}{2} \\ 0 \\ 0 \\ 0 \\ 0 \\ -\dfrac{|u_C|}{d_z} \end{Bmatrix}
\qquad (2.61)
$$

The stiffness matrix $\mathbf{k_0}$ in Equation (2.10) was used to compute the vector of joint forces as follows in which the pure shear stiffness was considered:

$$
\begin{Bmatrix} N_{x1} \\ N_{x2} \\ N_{z1} \\ N_{z2} \\ M_{x1} \\ M_{x2} \\ M_{z1} \\ M_{z2} \\ M_{0} \end{Bmatrix} =
\begin{bmatrix}
\dfrac{2td_z E_c}{d_x} & 0 & 0 & 0 & 0 & 0 & 0 & 0 & 0 \\
0 & \dfrac{2td_z E_c}{d_x} & 0 & 0 & 0 & 0 & 0 & 0 & 0 \\
0 & 0 & \dfrac{2td_x E_c}{d_z} & 0 & 0 & 0 & 0 & 0 & 0 \\
0 & 0 & 0 & \dfrac{2td_x E_c}{d_z} & 0 & 0 & 0 & 0 & 0 \\
0 & 0 & 0 & 0 & \dfrac{td_z^{3} E_c}{6d_x} & 0 & 0 & 0 & 0 \\
0 & 0 & 0 & 0 & 0 & \dfrac{td_z^{3} E_c}{6d_x} & 0 & 0 & 0 \\
0 & 0 & 0 & 0 & 0 & 0 & \dfrac{td_x^{3} E_c}{6d_z} & 0 & 0 \\
0 & 0 & 0 & 0 & 0 & 0 & 0 & \dfrac{td_x^{3} E_c}{6d_z} & 0 \\
0 & 0 & 0 & 0 & 0 & 0 & 0 & 0 & \dfrac{td_x d_z G}{\kappa}
\end{bmatrix}
\begin{Bmatrix} 0 \\ 0 \\ -\dfrac{r|u_C|}{2} \\ -\dfrac{r|u_C|}{2} \\ 0 \\ 0 \\ 0 \\ -\dfrac{|u_C|}{d_z} \end{Bmatrix} =
\begin{Bmatrix} 0 \\ 0 \\ -\dfrac{rtd_x E_c}{d_z}|u_C| \\ -\dfrac{rtd_x E_c}{d_z}|u_C| \\ 0 \\ 0 \\ 0 \\ -\dfrac{td_x G}{\kappa}|u_C| \end{Bmatrix}
\qquad (2.62)
$$

The nodal forces was computed from Equation (2.3) as follows:

$$
\begin{Bmatrix} F_{xA} \\ F_{zA} \\ M_A \\ F_{xB} \\ F_{zB} \\ M_B \\ F_{xC} \\ F_{zC} \\ M_C \\ F_{xD} \\ F_{zD} \\ M_D \end{Bmatrix} =
\begin{bmatrix}
0.5 & 0 & 0 & -1 & 0 & 0 & 0.5 & 0 & 0 & 0 & 0 & 0 \\
-0.5 & 0 & 0 & 0 & 0 & 0 & -0.5 & 0 & 0 & 1 & 0 & 0 \\
0 & -1 & 0 & 0 & 0.5 & 0 & 0 & 0 & 0 & 0 & 0.5 & 0 \\
0 & 0 & 0 & 0 & -0.5 & 0 & 0 & 1 & 0 & 0 & -0.5 & 0 \\
\dfrac{1}{d_z} & 0 & 0 & 0 & 0 & -1 & -\dfrac{1}{d_z} & 0 & 0 & 0 & 0 & 0 \\
-\dfrac{1}{d_z} & 0 & 0 & 0 & 0 & 0 & \dfrac{1}{d_z} & 0 & 0 & 0 & 0 & 1 \\
0 & 0 & -1 & 0 & -\dfrac{1}{d_x} & 0 & 0 & 0 & 0 & 0 & \dfrac{1}{d_x} & 0 \\
0 & 0 & 0 & 0 & \dfrac{1}{d_x} & 0 & 0 & 0 & 1 & 0 & -\dfrac{1}{d_x} & 0 \\
\dfrac{1}{d_z} & 0 & 0 & 0 & \dfrac{1}{d_x} & 0 & -\dfrac{1}{d_z} & 0 & 0 & 0 & -\dfrac{1}{d_x} & 0
\end{bmatrix}^{T}
\begin{Bmatrix} 0 \\ 0 \\ 0 \\ -\dfrac{rtd_xE_c}{d_z}|u_C| \\ -\dfrac{rtd_xE_c}{d_z}|u_C| \\ 0 \\ 0 \\ 0 \\ -\dfrac{td_xG}{\kappa}|u_C| \end{Bmatrix}
=
\begin{Bmatrix} -\dfrac{td_xG}{\kappa d_z}|u_C| \\ \dfrac{rtd_xE_c}{d_z}|u_C| \\ 0 \\ 0 \\ -\dfrac{tG}{\kappa}|u_C| \\ 0 \\ \dfrac{td_xG}{\kappa d_z}|u_C| \\ -\dfrac{rtd_xE_c}{d_z}|u_C| \\ 0 \\ 0 \\ \dfrac{tG}{\kappa}|u_C| \\ 0 \end{Bmatrix}
\tag{2.63}
$$

The Mohr circle in Figure 2.9 became that in Figure 2.13. From Equation (2.60) , the stress ratio $r = \sigma/\tau$ was represented by d_x/d_z as follows:

$$
r = \frac{1-\left(\dfrac{d_x}{d_z}\right)^2}{2\kappa\left(1+v\right)\dfrac{d_x}{d_z}}
\tag{2.64}
$$

where v is the Poisson coefficient.
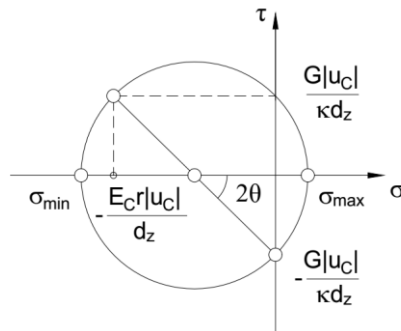
Figure 2.13. Mohr circles with stress represented by u_c

The principal stresses which were in diagonal direction and perpendicular to diagonal direction were also determined:

$$\sigma_{max} = \frac{|u_C|}{d_z} \left(\sqrt{\left(\frac{1-\left(\frac{d_x}{d_z}\right)^2}{\frac{2d_x}{d_z}} \frac{G}{\kappa} \right)^2 + \left(\frac{G}{\kappa}\right)^2} - \frac{1-\left(\frac{d_x}{d_z}\right)^2}{\frac{2d_x}{d_z}} \frac{G}{\kappa} \right) \tag{2.65}$$

$$\sigma_{min} = \frac{|u_C|}{d_z} \frac{G}{\kappa} \left(-\sqrt{\left(\frac{1-\left(\frac{d_x}{d_z}\right)^2}{\frac{2d_x}{d_z}} \right)^2 + 1} - \frac{1-\left(\frac{d_x}{d_z}\right)^2}{\frac{2d_x}{d_z}} \right) \tag{2.66}$$

The average deformations on diagonals caused by the rotation of rigid bodies were computed as belows:

$$\frac{\delta_{com\_1} + \delta_{ten\_6}}{2} = \frac{\delta_{com\_3} + \delta_{ten\_8}}{2} = \frac{d_x d_z}{\sqrt{d_x^2 + d_z^2}} \left(-\frac{1-\left(\frac{d_x}{d_z}\right)^2}{4d_x^2 \kappa (1+v)} d_z |u_C| - \frac{|u_C|}{2d_z} \right) \tag{2.67}$$

$$\frac{\delta_{com\_2} + \delta_{ten\_5}}{2} = \frac{\delta_{com\_4} + \delta_{ten\_7}}{2} = -\frac{\left[1-\left(\frac{d_x}{d_z}\right)^2\right] d_z |u_C|}{4\kappa (1+v) \sqrt{d_x^2 + d_z^2}} + \frac{\sqrt{d_x^2 + d_z^2} |u_C|}{d_z} \tag{2.68}$$

To reserve the stress state using concrete struts, the following equations were employed:

$$\sigma_{min} = \frac{\delta_{com\_1} + \delta_{ten\_6}}{2} \frac{E_c}{l_c} \tag{2.69}$$

$$\sigma_{max} = \frac{\delta_{com\_2} + \delta_{ten\_5}}{2} \frac{E_c}{l_t} \tag{2.70}$$

The length of concrete struts was computed as follows:

$$l_c = \frac{\delta_{com\_1} + \delta_{ten\_6}}{2} \frac{E_c}{\sigma_{min}} \tag{2.71}$$

$$l_t = \frac{\delta_{com\_2} + \delta_{ten\_5}}{2} \frac{E_c}{\sigma_{max}} \tag{2.72}$$

The set-up of specimens for analysis is shown in Figure 2.14.
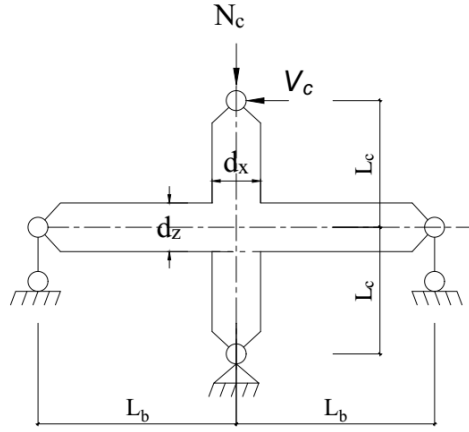
Figure 2.14. Specimen for analytical study

With r = 0:

$$d_x = d_z = 300mm;\ l_t = l_c = 293mm;\ L_b = L_c = 3.0m;\ r = \frac{\sigma}{\tau} = 0;\ \theta = 45^o$$

The analytical result is shown in Figure 2.15.
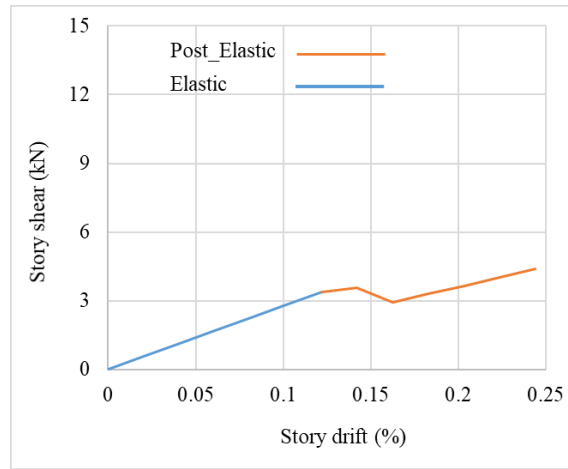
Figure 2.15. Analytical result of story shear versus story drift relationship (r = 0)

With r = 1:

$$d_x = 300mm;\ d_z = 485mm;\ l_t = 431mm;\ l_c = 345mm; L_b = 1.854m;\ L_c = 3.0m;\ r = \frac{\sigma}{\tau} = 1;\ \theta = 31.7^o$$

The analytical result is shown in Figure 2.16 and Table 2.1.

31
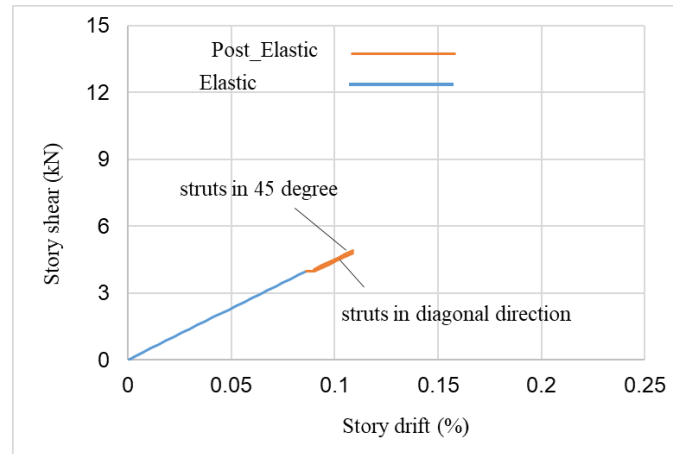
Figure 2.16. Analytical result of story shear versus story drift relationship (r = 1)

Table 2.1. Result of story shear ratio (r = 1)

Story drift (%)	Story shear ratio	Stage
0.079	1	
0.083	1	Elastic
0.086	1	
0.090	1.02	
0.094	1.02	
0.098	1.02	
0.101	1.02	Post-elastic
0.105	1.02	
0.109	1.02	

With r = 2:

$$d_x = 300mm; \ d_z = 724mm; \ l_t = 636mm; \ l_c = 435mm; \ L_b = 1.243m; \ L_c = 3.0m; \ r = \frac{\sigma}{\tau} = 2; \ \theta = 22.5^o$$

The analytical result is shown in Figure 2.17 and Table 2.2.
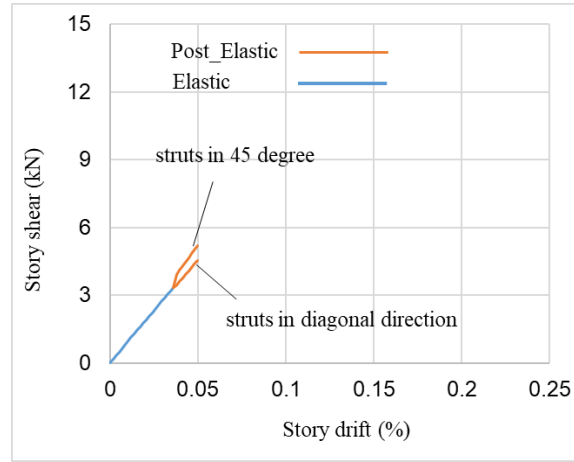
Figure 2.17. Analytical result of story shear versus story drift relationship (r = 2)

Table 2.2. Result of story shear ratio (r = 2)

Story drift	Story shear ratio	Stage
0.029	1	Elastic
0.031	1	
0.033	1	
0.034	1	
0.036	1	
0.038	1.14	Post-elastic
0.040	1.14	
0.041	1.14	
0.043	1.14	
0.045	1.14	
0.046	1.14	
0.048	1.14	
0.050	1.14	

With r = 10:

$$d_x = 300mm; \ d_z = 3030mm; \ l_t = 6142mm; \ l_c = 1534mm; L_b = 0.297m; \ L_c = 3.0m; \ r = \frac{\sigma}{\tau} = 10; \ \theta = 5.7^o$$

The analytical result is shown in Figure 2.18 and Table 2.3.
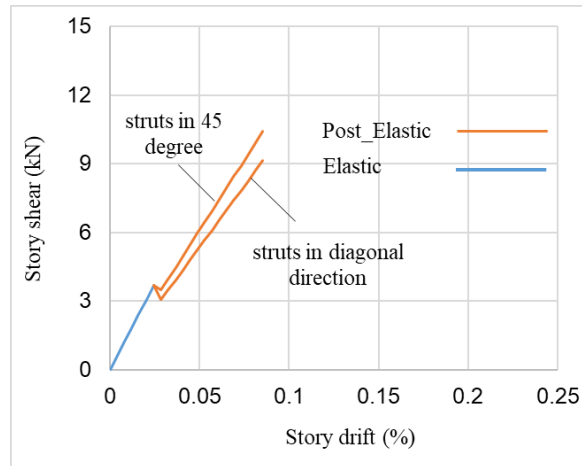
Figure 2.18. Analytical result of story shear versus story drift relationship (r = 10)

Table 2.3. Result of story shear ratio (r = 10)

Story drift	Story shear ratio	Stage
0.004	1	Elastic
0.008	1	
0.012	1	
0.016	1	
0.020	1	
0.024	1	
0.028	1.14	Post-elastic
0.033	1.14	
0.037	1.14	
0.041	1.14	
0.045	1.14	
0.049	1.14	
0.053	1.14	

The results showed that there was a little difference between the story shear computed with struts' angle of 45 degrees and the story shear computed with struts in diagonal direction in four

analytical cases. Corresponding to the stress ratio of 1, 2, and 10, the different ratio of story shear was 1.02, 1.14, and 1.14. This indicated that the assumption of struts' angle of 45 degrees after cracking was acceptable for analysis.

2.3.6   Constitutive material model

2.3.6.1   Constitutive steel model

The elastic-perfectly plastic hysteretic model is adopted for expressing the stress-strain relationship of bar springs which is assumed to follow the bilinear rule, as shown in Figure 2.19. Following formulas depicts skeleton curves of this model:

$$\sigma = \begin{cases} \sigma_y + 0.01E_s\left(\varepsilon - \varepsilon_y\right) & \left(\varepsilon_y \leq \varepsilon\right) \\ E_s\varepsilon & \left(-\varepsilon_y < \varepsilon < \varepsilon_y\right) \\ -\sigma_y + 0.01E_s\left(\varepsilon + \varepsilon_y\right) & \left(\varepsilon \leq -\varepsilon_y\right) \end{cases} \tag{2.73}$$

where σ, ε and E_s are stress, strain, and the initial stiffness respectively.
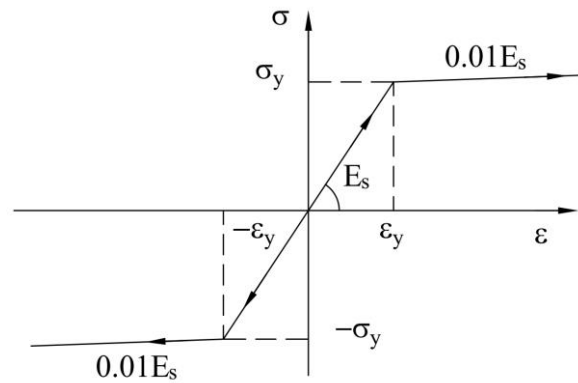
Figure 2.19. Monotonic constitutive steel rule

2.3.6.2   Constitutive concrete model

The concrete hysteresis rule used in this study is shown in Figure 2.20. The concrete stress was expressed as a function of the concrete strain in such specific cases that Equation (2.28) to Equation (2.31) could be achieved.

The envelope of the confined concrete proposed by Scott et al.[39] was used in the monotonic loading of the compressive path. The skeleton curves are expressed as follows:

$$
\sigma = \begin{cases}
0.001 E_c \varepsilon & \left(\varepsilon_t \leq \varepsilon\right) \quad (\textit{after cracking}) \\[2mm]
E_c \varepsilon & \left(0 \leq \varepsilon < \varepsilon_t\right) \quad (\textit{before cracking}) \\[2mm]
K_c f_c{}' \left[-\dfrac{2\varepsilon}{K_c \varepsilon_{c0}} + \left(\dfrac{\varepsilon}{K_c \varepsilon_{c0}}\right)^2 \right] & \left(K_c \varepsilon_{c0} \leq \varepsilon < 0\right) \\[4mm]
-K_c f_c{}' \left[1 + Z_m \left(\varepsilon - K_c \varepsilon_{c0}\right) \right] & \left(-\dfrac{0.8}{Z_m} + K_c \varepsilon_{c0} \leq \varepsilon < K_c \varepsilon_{c0}\right) \\[4mm]
0.001 E_c \left(\varepsilon + \dfrac{0.8}{Z_m} - K_c \varepsilon_{c0}\right) - 0.2 K_c f_c{}' & \left(\varepsilon < -\dfrac{0.8}{Z_m} + K_c \varepsilon_{c0}\right) \\[4mm]
.
\end{cases}
\tag{2.74}
$$

where K_c is a coefficient regarding the confinement of concrete:

$$
K_c = 1 + \frac{\rho_h \sigma_{yh}}{f_c{}'} \tag{2.75}
$$

$$
Z_m = \frac{0.5}{\dfrac{3 + 0.29 f_c{}'}{145 f_c{}' - 1000} + \dfrac{3}{4} \rho_h \sqrt{\dfrac{h''}{s_h}} + K_c \varepsilon_{c0}} \tag{2.76}
$$

In the above equation, σ, ε, and $f_c{}'$ are the stress, strain, and compressive strength respectively, ε_{c0} is the strain at the compressive strength $(\varepsilon_{c0} = -0.002)$; ρ_h is the volume ratio of the rectangular steel hoops to the volume of the concrete core measured at the exterior of the peripheral hoop; σ_{yh} is the yield strength of the hoop; s_h is the spacing of the hoops; and h'' is the width of the concrete core measured at the exterior of the peripheral hoop.

In this study, only the concrete in compression was considered. The concrete in tension was not interested because its contribution was small. Stiffness of E_c and $0.001 E_c$ was assigned to the tension path before and after cracking respectively. The strain at tensile strength was defined as follows:

$$
\varepsilon_t = \frac{0.1 f_c{}'}{E_c} \tag{2.77}
$$

36
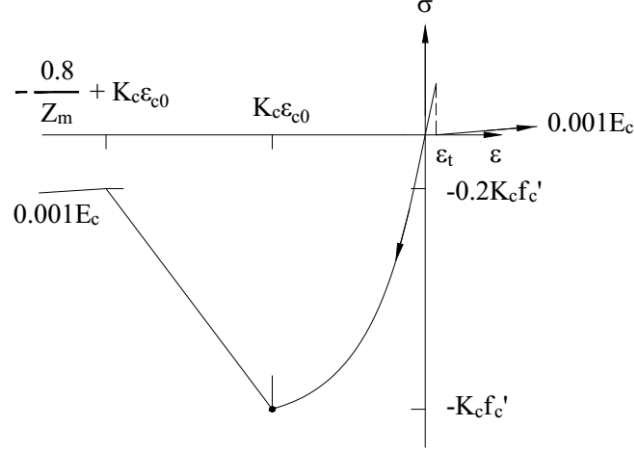
Figure 2.20. Monotonic constitutive concrete rule

To determine the stress distribution from the strain distribution in the diagonal-oriented section of the struts, an assumption of zero stress at zero strain was adopted. The loading paths were calculated by Equation (2.28) and Equation (2.29) with the loading envelopes defined above.

When $K_c \varepsilon_{c0} \leq \varepsilon_{com\_i} < 0$:

$$\sigma_{Ci} = \int_0^{\varepsilon_{com\_i}} \frac{K_c f_c{}'}{\varepsilon_{com\_i}} \left[-\frac{2\varepsilon}{K_c \varepsilon_{c0}} + \left(\frac{\varepsilon}{K_c \varepsilon_{c0}} \right)^2 \right] d\varepsilon \tag{2.78}$$

$$\beta_{Ci} = \xi_i \left[1 - \frac{\int_0^{\varepsilon_{com\_i}} \left(-\frac{2\varepsilon^2}{K_c \varepsilon_{c0}} + \frac{\varepsilon^3}{\left(K_c \varepsilon_{c0} \right)^2} \right) d\varepsilon}{\varepsilon_{com\_i} \int_0^{\varepsilon_{com\_i}} \left(-\frac{2\varepsilon}{K_c \varepsilon_{c0}} + \left(\frac{\varepsilon}{K_c \varepsilon_{c0}} \right)^2 \right) d\varepsilon} \right] \tag{2.79}$$

When $-\frac{0.8}{Z_m} + K_c \varepsilon_{c0} \leq \varepsilon_{com\_i} < K_c \varepsilon_{c0}$:

$$\sigma_{Ci} = \int_0^{K_c f_c{}'} \frac{K_c f_c{}'}{\varepsilon_{com\_i}} \left[-\frac{2\varepsilon}{K_c \varepsilon_{c0}} + \left(\frac{\varepsilon}{K_c \varepsilon_{c0}} \right)^2 \right] d\varepsilon - \int_{K_c f_c{}'}^{\varepsilon_{com\_i}} \frac{K_c f_c{}'}{\varepsilon_{com\_i}} \left[1 + Z_m \left(\varepsilon - K_c \varepsilon_{c0} \right) \right] d\varepsilon \tag{2.80}$$

37

$$\beta_{Ci} = \xi_i \left[1 - \frac{\displaystyle\int_0^{K_c f_c'} \left(-\frac{2\varepsilon^2}{K_c \varepsilon_{c0}} + \frac{\varepsilon^3}{\left(K_c \varepsilon_{c0}\right)^2} \right) d\varepsilon - \int_{K_c f_c'}^{\varepsilon_{com\_i}} \left[\varepsilon + Z_m \left(\varepsilon^2 - K_c \varepsilon_{c0} \varepsilon \right) \right] d\varepsilon}{\displaystyle \varepsilon_{com\_i} \int_0^{K_c f_c'} \left[-\frac{2\varepsilon}{K_c \varepsilon_{c0}} + \left(\frac{\varepsilon}{K_c \varepsilon_{c0}} \right)^2 \right] d\varepsilon - \int_{K_c f_c'}^{\varepsilon_{com\_i}} \left[1 + Z_m \left(\varepsilon - K_c \varepsilon_{c0} \right) \right] d\varepsilon} \right] \tag{2.81}$$

When $\varepsilon_{com\_i} < -\dfrac{0.8}{Z_m} + K_c \varepsilon_{c0}$:

$$\sigma_{Ci} = \int_0^{K_c f_c'} \frac{K_c f_c'}{\varepsilon_{com\_i}} \left[-\frac{2\varepsilon}{K_c \varepsilon_{c0}} + \left(\frac{\varepsilon}{K_c \varepsilon_{c0}} \right)^2 \right] d\varepsilon - \int_{K_c f_c'}^{-\frac{0.8}{Z_m} + K_c \varepsilon_{c0}} \frac{K_c f_c'}{\varepsilon_{com\_i}} \left[1 + Z_m \left(\varepsilon - K_c \varepsilon_{c0} \right) \right] d\varepsilon$$

$$+ \int_{-\frac{0.8}{Z_m} + K_c \varepsilon_{c0}}^{\varepsilon_{com\_i}} \left[\frac{0.001 E_c}{\varepsilon_{com\_i}} \left(\varepsilon + \frac{0.8}{Z_m} - K_c \varepsilon_{c0} \right) - \frac{0.2 K_c f_c'}{\varepsilon_{com\_i}} \right] d\varepsilon \tag{2.82}$$

$$\beta_{Ci} = \xi_i \left[1 - \frac{\displaystyle\int_0^{K_c f_c'} \left[-\frac{2\varepsilon}{K_c \varepsilon_{c0}} + \left(\frac{\varepsilon}{K_c \varepsilon_{c0}} \right)^2 \right] d\varepsilon - \int_{K_c f_c'}^{-\frac{0.8}{Z_m} + K_c \varepsilon_{c0}} \left[1 + Z_m \left(\varepsilon - K_c \varepsilon_{c0} \right) \right] d\varepsilon + \displaystyle\int_{-\frac{0.8}{Z_m} + K_c \varepsilon_{c0}}^{\varepsilon_{com\_i}} \left[\frac{0.001 E_c}{K_c f_c'} \left(\varepsilon + \frac{0.8}{Z_m} - K_c \varepsilon_{c0} \right) - 0.2 \right] d\varepsilon}{\varepsilon_{com\_i} \left\{ \displaystyle\int_0^{K_c f_c'} \left[-\frac{2\varepsilon}{K_c \varepsilon_{c0}} + \left(\frac{\varepsilon}{K_c \varepsilon_{c0}} \right)^2 \right] d\varepsilon - \int_{K_c f_c'}^{-\frac{0.8}{Z_m} + K_c \varepsilon_{c0}} \left[1 + Z_m \left(\varepsilon - K_c \varepsilon_{c0} \right) \right] d\varepsilon + \displaystyle\int_{-\frac{0.8}{Z_m} + K_c \varepsilon_{c0}}^{\varepsilon_{com\_i}} \left[\frac{0.001 E_c}{K_c f_c'} \left(\varepsilon + \frac{0.8}{Z_m} - K_c \varepsilon_{c0} \right) - 0.2 \right] d\varepsilon \right\}} \right] \tag{2.83}$$

2.3.7   Computational procedure

The detailed computational procedure of the joint is described in Figure 2.21 for stages before cracking and in Figure 2.22 for stages after cracking in which a set of the joint nodal displacements (**e**) returned in a set of the joint nodal forces (**p**). In the frame analysis, the chart in Figure 2.23 shows the iterative computational technique at an analytical step with n times of iteration in which the Newton-Raphson method was used. When the error of the nodal forces decreased and met the desired tolerance, the errors of the axial forces in the springs and the

struts of the joint were automatically eliminated. Due to the convergence criterial of Newton-Raphson method, the degradation paths were not interested. Object-Based Structural Analysis (OBASAN), which is an open-source object-oriented program developed by the authors' laboratory is used to produce responses of the analysis.

To model the beams and the columns, the element "beam end" in OBASAN was used. This element was developed on the basis of the one-component model [40, 41] in which the inelastic flexural deformation of the element was assumed to be governed by the deformation of two rotational springs located at the ends. The axial force versus the axial deformation was assumed to be elastic and the shear deformation was included. The bond-slip within the beams and the columns was not considered. The moment-rotation relationship was used to define the characteristics of the two rotational springs. Takeda hysteresis rule [42] was used to establish the hysteresis response.

The moment-rotation backbone consisting of three points (θ_c, M_c), (θ_y, M_y), and (θ_u, M_u) was determined from the backbone of the moment-curvature relationship consisting of three points (ϕ_c, M_c), (ϕ_y, M_y), and (ϕ_u, M_u). In this study, M_c, M_y, and M_u were determined following ACI 318 [2]. The following equations show the computation of the rotations from the curvatures. The rotation at cracking of tensile concrete:

$$\theta_c = M_c\left(\frac{l}{3EI} + \frac{\kappa}{GAl}\right) \tag{2.84}$$

where EI is the initial elastic flexural rigidity; l is the length of a simply supported member; κ is the shear coefficient; GA is the shear rigidity; M_c is the moment at cracking of tensile concrete. The rotation at the yielding of tensile reinforcement:

$$\theta_y = \frac{l\left[\left(1-\lambda^3\right)\phi_y + \lambda^2\phi_c\right]}{3} \tag{2.85}$$

$$\lambda = \frac{M_c}{M_y} \tag{2.86}$$

ϕ_c is the curvature at cracking of tensile concrete; ϕ_y is the curvature at cracking of tensile reinforcement; M_y is the moment at yielding of tensile reinforcement.

The rotation at the crushing of compressive concrete:

$$\theta_u = \frac{l}{6}\left[\left\{\frac{(2+\lambda_2)(1-\lambda_2)(\alpha\lambda_2+1-\lambda_2)}{\alpha}+\lambda_2(1+\lambda_2)-2\lambda_1^3\right\}\frac{\phi_y}{\lambda_2}+2\lambda_1^2\phi_c\right] \qquad (2.87)$$

where

$$\lambda_1 = \frac{M_c}{M_u} \qquad (2.88)$$

$$\lambda_2 = \frac{M_y}{M_u} \qquad (2.89)$$

$$\alpha = \frac{M_u - M_y}{\phi_u - \phi_y}\frac{\phi_y}{M_y} \qquad (2.90)$$

M_u is the moment at crushing of compressive concrete.
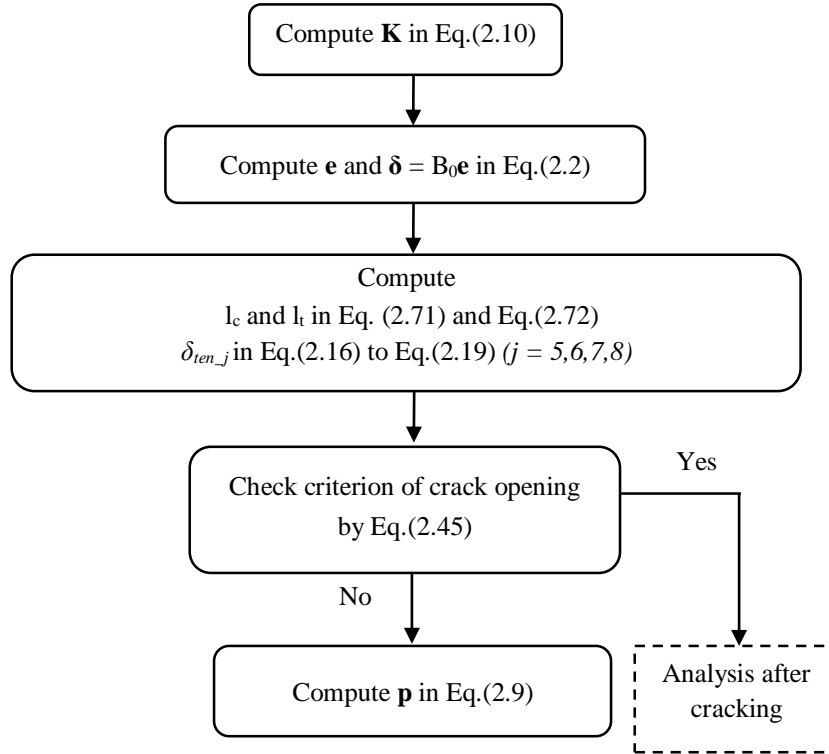
Figure 2.21. Computational procedure before cracking of the new interior joint element
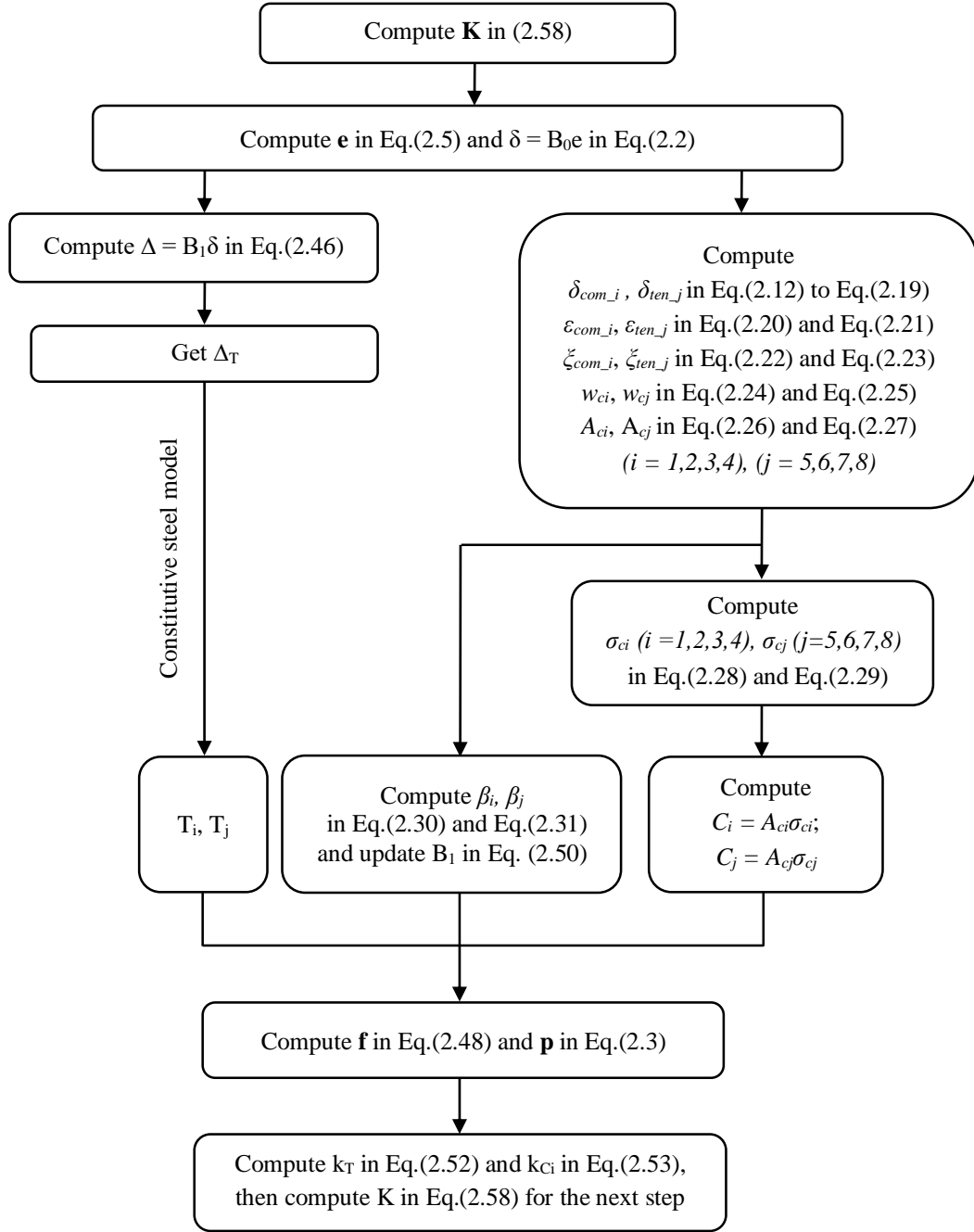
Figure 2.22. Chart of the computational procedure after cracking of the new joint element
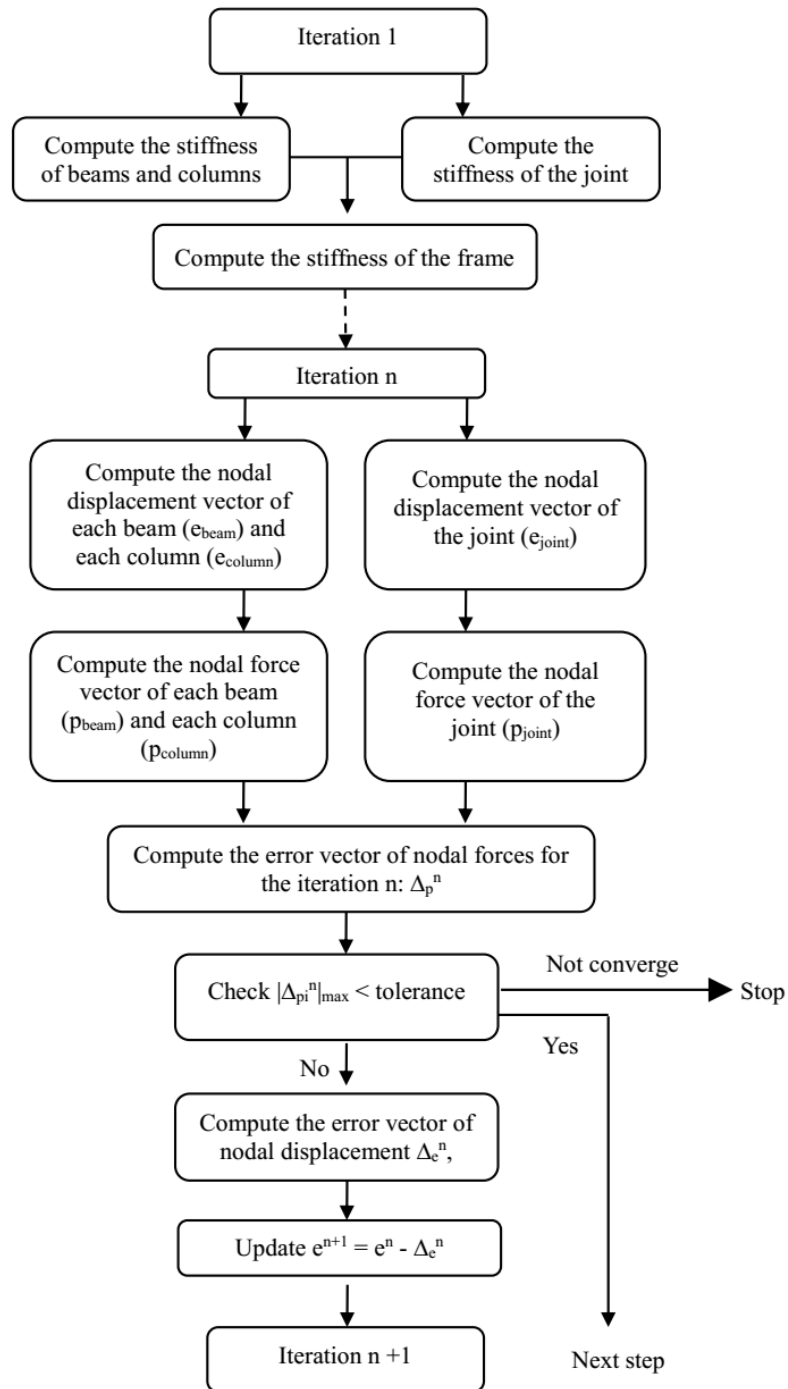
Figure 2.23. Chart of the Newton-Raphson iterative algorithm of the frame analysis at a step

2.3.8   Verification of experimental study

2.3.8.1 Specimens

A series of test of the reinforced concrete joint subassemblages with regard to specimen A01, B01, B02, B05, and C01 conducted by Shiohara and Kusuhara [43, 44] was adopted in this study for verification. The detailed properties of the materials of specimens are listed in Table 2.4 and illustrated geometrically in Figure 2.24. Specimen A01 had the section of 300x300 mm and was suffered from a constant axial compressive load of 216kN and a lateral load where the cyclic loading was applied in sequence at different story drifts as followings: a cycle at 0.0625%, 0.125%, and 0.25%, two cycles at 0.5% and 1.0%, a cycle at 0.5%, two cycles at 2.0%, a cycle at 0.5%, and two cycles at 3.0% and 4.0%. Specimen from B01 to C01 had the same cross-section of 240 x 240 mm for both beams and columns and suffered only a lateral load. At each story drift of 0.25%, 0.5%, 1.0%, 1.5%, 2.0%, and 3.0%, two cyclic loadings were applied horizontally.
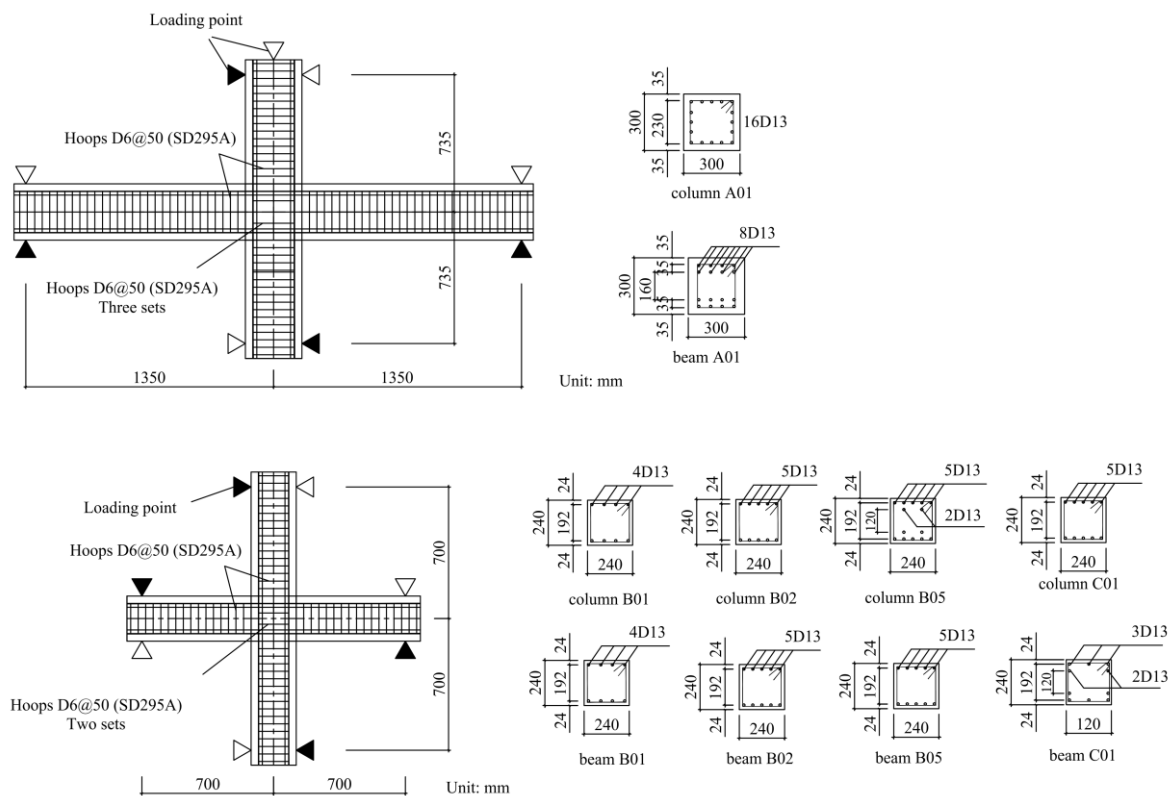
Figure 2.24. Test specimen of interior joints specimens with identical depth of beams and columns

43

Table 2.4. Properties of interior joint specimens with identical depth of beams and columns

Specimen	A01	B01	B02	B05	C01
Concrete compressive strength (MPa)	28.3	29	29.0	29.0	31.0
Beam width x depth (mm)	300 x 300	240 x 240	240 x 240	240 x 240	240 x 240
Longitudinal beam bars	8-D13 8-D13	4-D13	5-D13	5-D13	3-D13 2-D13
Bar yielding strength (Mpa)	456	378	378	378	378
Bar distant ratio	0.77 0.53	0.8	0.8	0.8	0.8 0.5
Column width x depth (mm)	300 x 300	240 x 240	240 x 240	240 x 240	240 x 240
Longitudinal column bars	5-D13 2-D13 2-D13	4-D13	5-D13	5-D13 2-D13	5-D13
Column bar yielding strength (MPa)	357	378	378	378	378
Column bar distant ratio	0.77 0.57 0	0.8	0.8	0.8 0.5	0.8
Joint hoops	D6 (three sets)	D6 (two sets)			
Yielding strength of hoops (MPa)	326	399			

2.3.9 Discussion of results

2.3.9.1 Load deflection relationship

The relationship of the story shear versus the story drift of all specimens is shown in Figure 2.25. Beside the test data and the analysis, the response of specimen B02 and B05 carried out by Kusuhara joint model [10] was also used for comparison. Because the specific results of the response given by Kusuhara joint model was not available, the comparison with regard to the difference of the backbone shape was considered. Table 2.5 compares the maximum story shear predicted by the new joint model ($V_{u\_Analysis}$) to that of the experimental results, at the flexural strength of beam (V_{u_ACI}) by ACI 318 – 08 [2], and computed at the nominal joint shear strength (V_{u_AIJ}) by AIJ 1999 [1].

The monotonic response in this study was expected to capture the backbone of the cyclic response of each specimen with refer to the story shear versus the story drift relationship. The degradations of the backbones were computed at the story drift of 2.6%, 3.3%, 2.7%, 2.6%, and 2.55% for specimen A01, B01, B02, B05, and C01 respectively. The results from Figure 2.25 and Table 2.5 showed a good agreement between the test and the analysis. The computed maximum story shears were close to the observed maximum story shears with the different ratio 1.00 in A01, 1.02 in B01 and B02, 1.01 in B05, and 0.95 in C01. The maximum story shears from the analysis were also close to those determined at the flexural strength of beam derived from ACI 318-08 and at the nomial joint shear strength recommended by AIJ 1999 except in specimen B01 where the different ratio between $V_{u\_Analysis}$ and V_{u_AIJ} was 0.84.

In Kusuhara's model, the diagonal-, vertical-, and horizontal springs were used to represent concrete. Kusuhara model showed a good prediction of the cyclic behaviors of specimen B02 and B05 in Figure 2.25, which were also captured well by the monotonic backbone of the new joint model. However, the present model aimed to model the original aspect of SMM. That was the use of concrete strut to represent the flow compressive forces transferred through concrete. Beside the load-deflection relationship, the present model provided various properties which could not be given by the multi-spring models. They included the changes of the strain distribution and stress distribution of concrete on the joint diagonals in consistent with the rotations of the four free bodies. These changes, as discussed in an overlook mechanism by Shiohara [6], were useful to explain the consistent relationship of the opening of diagonal cracks, the stress redistribution, and the loss of tensile resistance.

2.3.9.2 Comparison to Shiohara's numerical method

A comparison between the computation by the new model and Shiohara's numerical method [5] at the ultimate stage is shown in Figure 2.26. All of the forces were normalized by *0.85tf'$_c$*. There was a good agreement between the results of the new model and those of the Shiohara's numerical method in which the story shear and forces in reinforcements and concrete were mostly the same in the two cases. The slight difference in the concrete resultant forces was attributed to the location of the concrete resultant forces and the stress at yielding of reinforcing bars. In Shiohara's numerical method, concrete resultant forces were placed at the middle of the stress distribution on the diagonals while the location of the resultant forces in concrete was determined by coefficient β_i in Equation (2.30) and β_j in Equation (2.31). The stress at yielding of reinforcement in Shiohara's numerical method was the corresponding yielding strength. In the computation by the new model, the stress at reinforcement yielding was greater than the corresponding yielding strength due to the additional strength caused by the strain hardening illustrated by the stiffness of $0.01E_s$ in Figure 2.19.

Table 2.5. Analytical results of the maximum story shear of the five specimens

	Results	A01	B01	B02	B05	C01
Maximum story shear (kN)	At the flexural strength of beam by ACI 318 - 08[2] (V_{bu})	135.5	66.1	79.2	81.0	81.5
	Computed at the nominal joint shear strength by AIJ 1999 (V_{ju})	137.1	80.5	80.5	80.5	80.5
	Test (V_{cmax_Test})	126.6	65.2	76.7	79.3	75.3
	Analysis ($V_{u\_Analysis}$)	135.8	67.6	81.0	81.6	77.6
	$V_{cmax\_Analysis} / V_{bu}$	1.00	1.02	1.02	1.01	0.95
	$V_{cmax\_Analysis} / V_{ju}$	0.99	0.84	1.01	1.01	0.96
	$V_{cmax\_Analysis} / V_{cmax\_Test}$	1.07	1.04	1.06	1.03	1.03
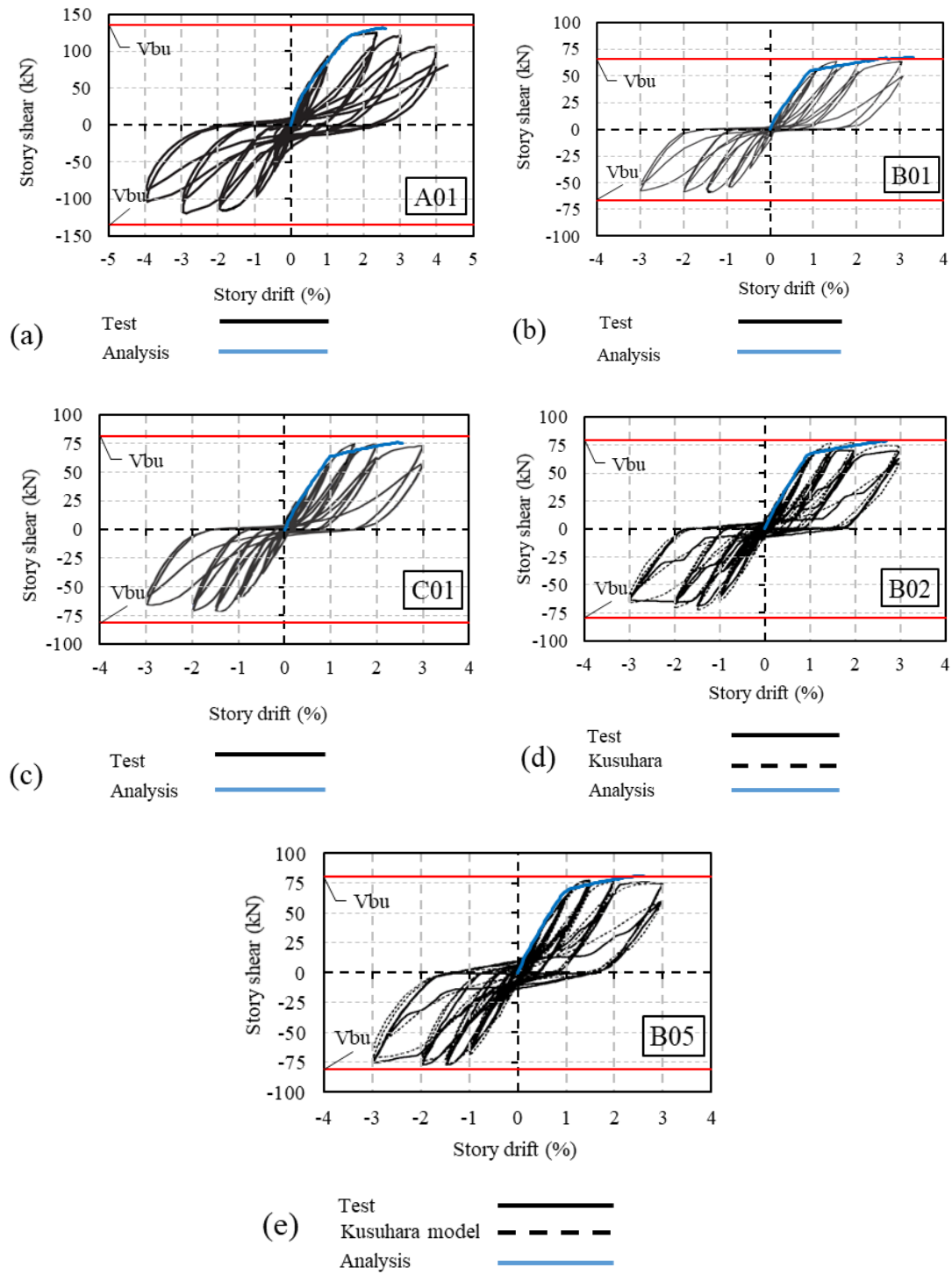
Figure 2.25. Comparison between experiment and monotonic response of the five specimens with perfect bond condition
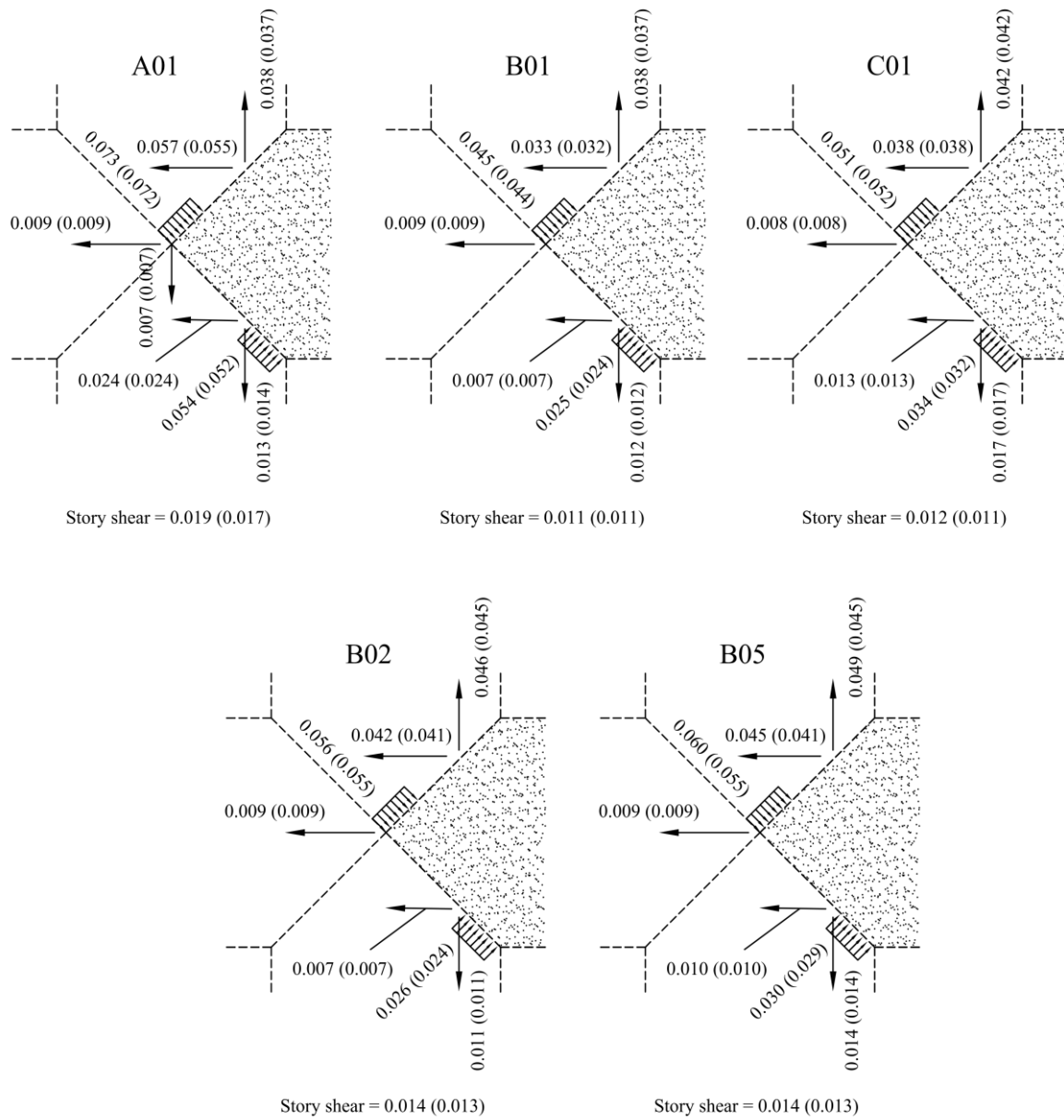
Figure 2.26. Predicted story shear in of the five specimens by the new joint model with

perfect bond condition

(number in parentheses is determined by Shiohara's numerical method)

2.4   Modification of the new model to investigate the monotonic response of the interior beam-column joints with an identical depth of beams and columns and normal bond condition

Bond-slip springs were included to consider the normal bond-condition. There were changes of bar springs and suggestions of bond-slip springs as below.

48

2.4.1 Bar springs and bond-slip springs

To simulate the anchorage loss along the longitudinal bar, four bond-slip springs (S_A, S_B, S_C, and S_D) were placed between two adjacent bar springs, as shown in Figure 2.27. The deformations of the bar springs and bond-slip springs related to the axial force of the corresponding springs through their tangent stiffness as follows:

$$T_i = k_{Ti}\Delta_{Ti} \quad with \ i = 1 \ to \ 10 \tag{2.91}$$

$$S_r = k_{Sr}\Delta_{Sr} \quad with \ r = A, \ B, \ C, \ D \tag{2.92}$$

where k_{Ti} and k_{Sr} are the stiffness values of bar spring i and bond-slip spring r, and Δ_{Ti} and Δ_{Sr} are the deformations of these springs, respectively. k_{Sr} is defined as follows:

$$k_{Sr} = \rho_{Sr}l_{Sr}k_{\tau_r} \quad with \ r = A, \ B, \ C, \ D \tag{2.93}$$

where ρ_{Sr} is the total section perimeter of the bars including in bond-spring S_r, l_{Sr} is the anchorage bond length, and $k\tau_{Sr}$ is the tangent stiffness regarding the relationship of the bond stress versus the slip of bond-spring S_r. Bond stress τ_{Sr} is computed by bond force S_r as follows:

$$\tau_{Sr} = \frac{S_r}{\rho_{Sr}l_{Sr}} \quad with \ r = A, \ B, \ C, \ D \tag{2.94}$$

In this study, S_A, S_B, S_C, and S_D were assumed to be positive $(+)$ when the bars slipped toward the bar springs T_2, T_4, T_8 and T_6, respectively.

A relationship between the forces in the bar springs and the deformations of the bar and bond-slip springs was established in a combined form, as follows:

$$\mathbf{T} = \mathbf{k_{TS}\Delta_{TS}} \tag{2.95}$$

where:

$\mathbf{T}$ is the vector of forces in the bar springs, as follows:

$$\mathbf{T} = \{T_1, T_2, T_3, T_4, T_5, T_6, T_7, T_8, T_9, T_{10}\} \tag{2.96}$$

$\Delta_{\mathbf{TS}}$ is the vector of the combined spring deformation and is defined as follows:

$$\Delta_{TS} = \left\{ \Delta_{TS_1}, \Delta_{TS_2}, \Delta_{TS_3}, \Delta_{TS_4}, \Delta_{T_5}, \Delta_{TS_6}, \Delta_{TS_7}, \Delta_{TS_8}, \Delta_{TS_9}, \Delta_{T_{10}} \right\} \tag{2.97}$$

Vector Δ_{TS} was used because of its compatibility with joint deformations.

k_{TS} is the matrix of the combined tangent stiffness of the bar springs and bond-slip springs:

$$\mathbf{k_{TS}} = \begin{bmatrix}
k_{T_{1-1}} & k_{T_{1-2}} & 0 & 0 & 0 & 0 & 0 & 0 & 0 & 0 \\
k_{T_{2-1}} & k_{T_{2-2}} & 0 & 0 & 0 & 0 & 0 & 0 & 0 & 0 \\
0 & 0 & k_{T_{3-3}} & k_{T_{3-4}} & 0 & 0 & 0 & 0 & 0 & 0 \\
0 & 0 & k_{T_{4-3}} & k_{T_{4-4}} & 0 & 0 & 0 & 0 & 0 & 0 \\
0 & 0 & 0 & 0 & k_{T_5} & 0 & 0 & 0 & 0 & 0 \\
0 & 0 & 0 & 0 & 0 & k_{T_{6-6}} & k_{T_{6-7}} & 0 & 0 & 0 \\
0 & 0 & 0 & 0 & 0 & k_{T_{7-6}} & k_{T_{7-7}} & 0 & 0 & 0 \\
0 & 0 & 0 & 0 & 0 & 0 & 0 & k_{T_{8-8}} & k_{T_{8-9}} & 0 \\
0 & 0 & 0 & 0 & 0 & 0 & 0 & k_{T_{9-8}} & k_{T_{9-9}} & 0 \\
0 & 0 & 0 & 0 & 0 & 0 & 0 & 0 & 0 & k_{T_{10}}
\end{bmatrix} \tag{2.98}$$

$$\text{with} \quad k_{T_{i-i}} = \frac{k_{T_i}(k_{T_j} + k_{S_r})}{k_{T_i} + k_{T_j} + k_{S_r}} \tag{2.99}$$

$$\text{and} \quad k_{T_{i-j}} = \frac{k_{T_i} k_{T_j}}{k_{T_i} + k_{T_j} + k_{S_r}} \tag{2.100}$$

(i, j = 1, 2, 3, 4, 6, 7, 8, 9; r = A, B, C, D)

(a) Location of springs; (b) Axial forces of springs; (c) Deformations of springs
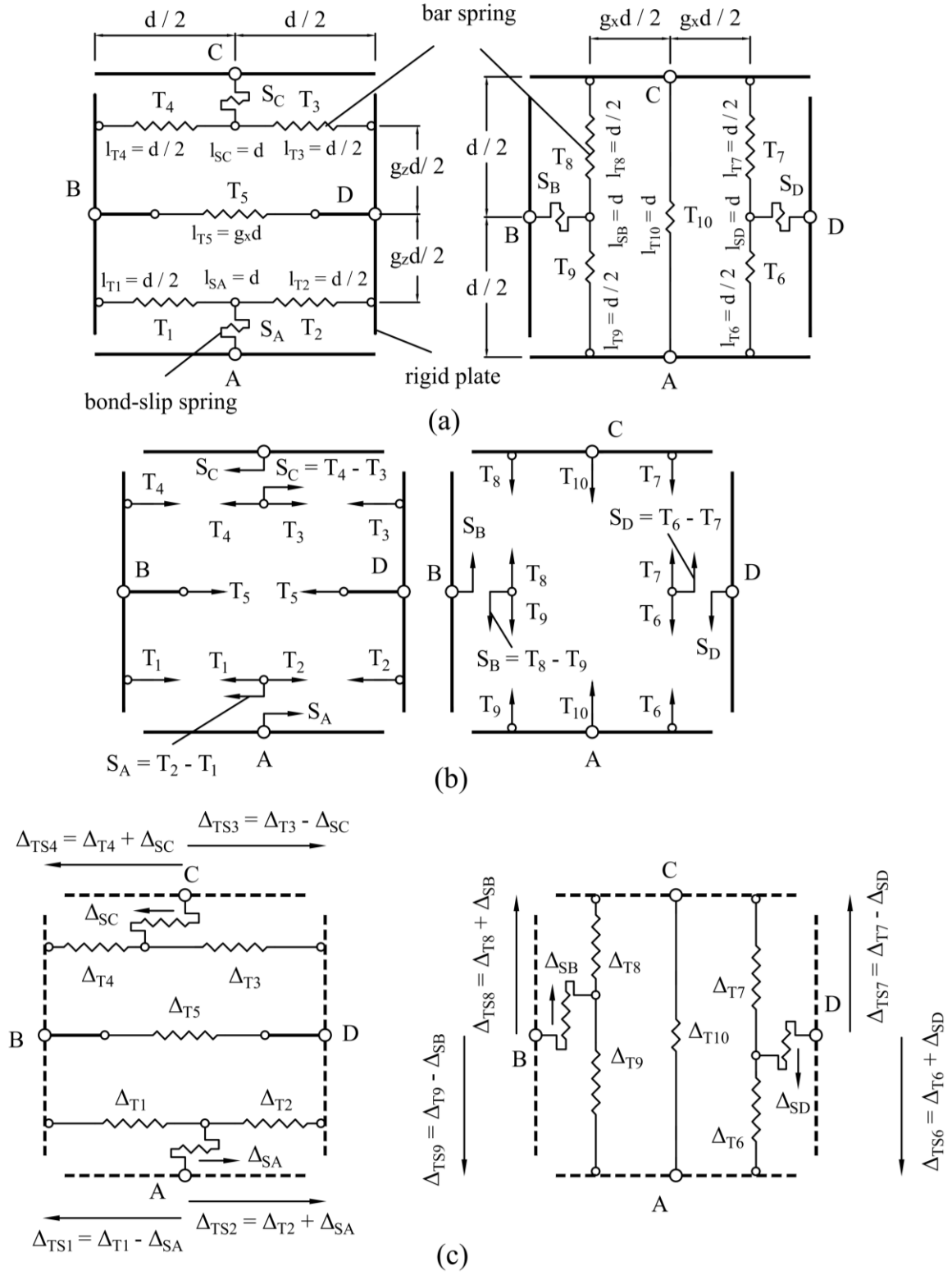
Figure 2.27. Definition of bar springs and bond-slip springs of the interior joint element

2.4.2 Joint compatibility and stiffness

The computation of the joint compatibility and the joint stiffness in Section 2.3.4 had some modification regarding vector Δ in Equation (2.47) and matrix $\mathbf{k_1}$ in (2.52) as follows:

$$\Delta = \left\{ \Delta_{C_1}, \Delta_{C_2}, ..., \Delta_{C_7}, \Delta_{C_8}, \Delta_{TS_1}, \Delta_{TS_2}, ..., \Delta_{T_5}, ..., \Delta_{TS_9}, \Delta_{T_{10}} \right\} \tag{2.101}$$

$$\mathbf{k}_1 = \begin{bmatrix} \mathbf{k_C} & 0 \\ 0 & \mathbf{k_{TS}} \end{bmatrix} \tag{2.102}$$

where $\mathbf{k_{TS}}$ is defined in Equation (2.98).

2.4.3 Constitutive material model

Constitutive bond-slip model

The bond slip model of CEB-FIP Model Code 1990 [37] was adopted along with the rules of the unloading and reloading path defined by Eligehausen et al.[25], as shown in Figure 2.28. Here, τ is the bond stress, s is the slip, $s_1 = 0.1s_3$, $s_2 = 0.5s_3$, $s_3 = 1$mm, $s_4 = s_3 + 2$ (mm), $s_5 = s_3 + 10.5$ (mm), $\tau_3 = 2.5f'_c$ (MPa), $\tau_5 = \tau_1 = 0.398\,\tau_3$, $\tau_2 = 0.758\tau_3$, $\tau_4 = \tau_3$.
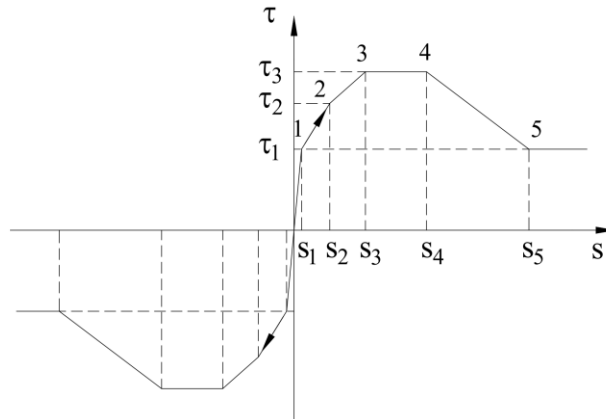
Figure 2.28. Monotonic constitutive bond-slip model

2.4.4 Computational procedure

Chart of the computation procedure for a joint element after cracking was modified as shown in Figure 2.29.
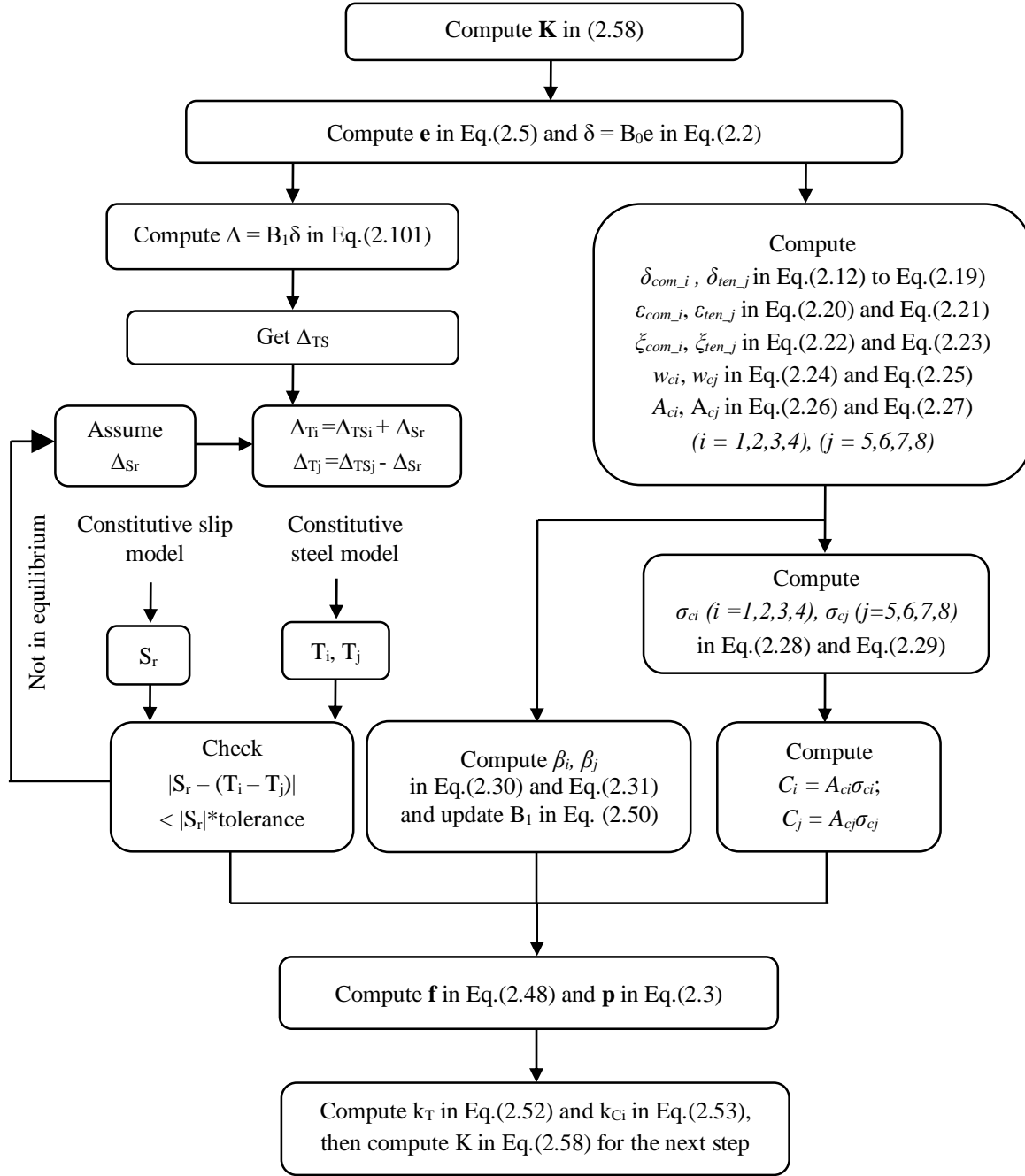
Figure 2.29. Chart of the computational procedure after cracking for a joint element with normal bond condition

2.4.5 Verification of experimental study

2.4.5.1 Specimens

The analysis was carried out on the five specimens described in section 2.3.8.

53

2.4.5.2 Load deflection relationship

Table 2.6 compares the maximum story shear predicted by the new joint model ($V_{u\_Analysis}$) to that of the experimental results, at the flexural strength of beam (V_{u_ACI}) by ACI 318 – 08 [2], and computed at the nominal joint shear strength (V_{u_AIJ}) by AIJ 1999 [1]. The relationship of the story shear versus the story drift of all specimens is shown in Figure 2.30.

The analytical result captured well the backbone of the cyclic response of each specimen with refer to the story shear versus the story drift relationship. The degradations of the backbones were computed at the story drift of 2.6%, 3.3%, 3.0%, 2.6%, and 2.5% for specimen A01, B01, B02, B05, and C01 respectively. In B02 and B05, the predicted curves by the new model were also in a good correlation with the backbone of the cyclic response computed by Kusuhara's model. There was not considerable difference of the analytical results between the case with perfect bond condition and the case without perfect bond condition. This agreed well with a conclusion of Shiohara [33] that the bond capacity does not affect significantly joint strength with J-mode. However, it makes sense in explaining the case of 3D joint in which transverse beam exists and reinforces bond capacity, as a result, there is observed increase of joint strength.

2.4.5.3 Comparison to Shiohara's numerical method

A comparison between the computation by the new model and Shiohara's numerical method at the ultimate stage is shown in Figure 2.31. All of the forces were normalized by *0.85tf'$_c$*. Similar to the case with perfect bond condition, there was also a good agreement between the results of the new model and those of the Shiohara's numerical method in which the story shear and forces in reinforcements and concrete were mostly the same in the two cases.

Table 2.6. Analytical results of the maximum story shear of the five specimens with normal bond condition

	Results	A01	B01	B02	B05	C01
Maximum story shear (kN)	At the flexural strength of beam by ACI 318 - 08[2] (V_{bu})	135.5	66.1	79.2	81.0	81.5
	Computed at the nominal joint shear strength by AIJ 1999 (V_{ju})	137.1	80.5	80.5	80.5	80.5
	Test (V_{cmax_Test})	126.6	65.2	76.7	79.3	75.3
	Analysis ($V_{u\_Analysis}$)	131.3	67.3	78.5	81.2	75.9
	$V_{cmax\_Analysis} / V_{bu}$	0.97	1.02	0.99	1.00	0.93
	$V_{cmax\_Analysis} / V_{ju}$	0.96	0.84	0.98	1.01	0.94
	$V_{cmax\_Analysis} / V_{cmax\_Test}$	1.04	1.03	1.02	1.02	1.01
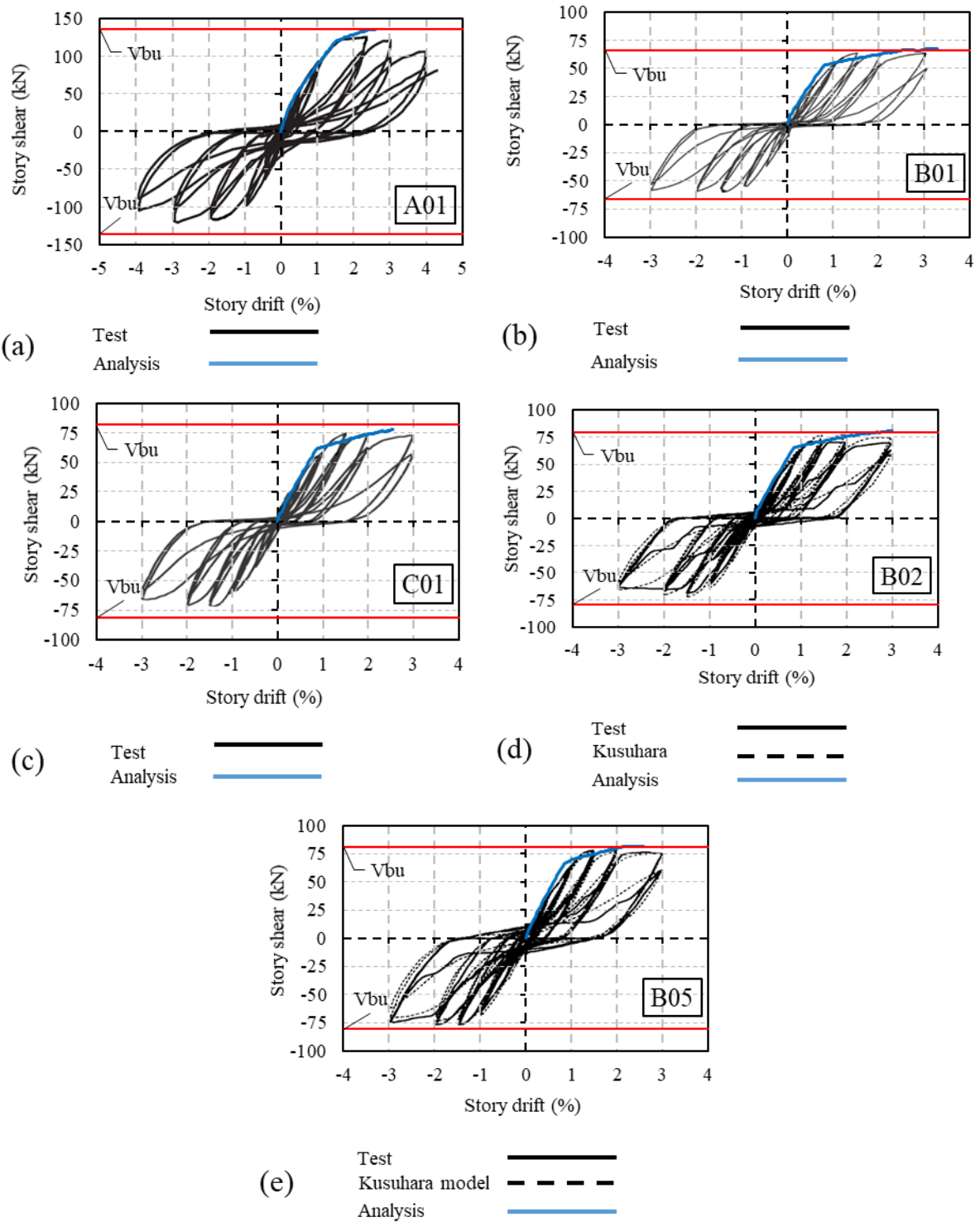
Figure 2.30. Comparison between experiment and monotonic response of the five specimens with normal bond condition

A01 · B01 · C01

Story shear = 0.018 (0.017) · Story shear = 0.011 (0.011) · Story shear = 0.012 (0.011)

B02 · B05

Story shear = 0.013 (0.013) · Story shear = 0.014 (0.013)
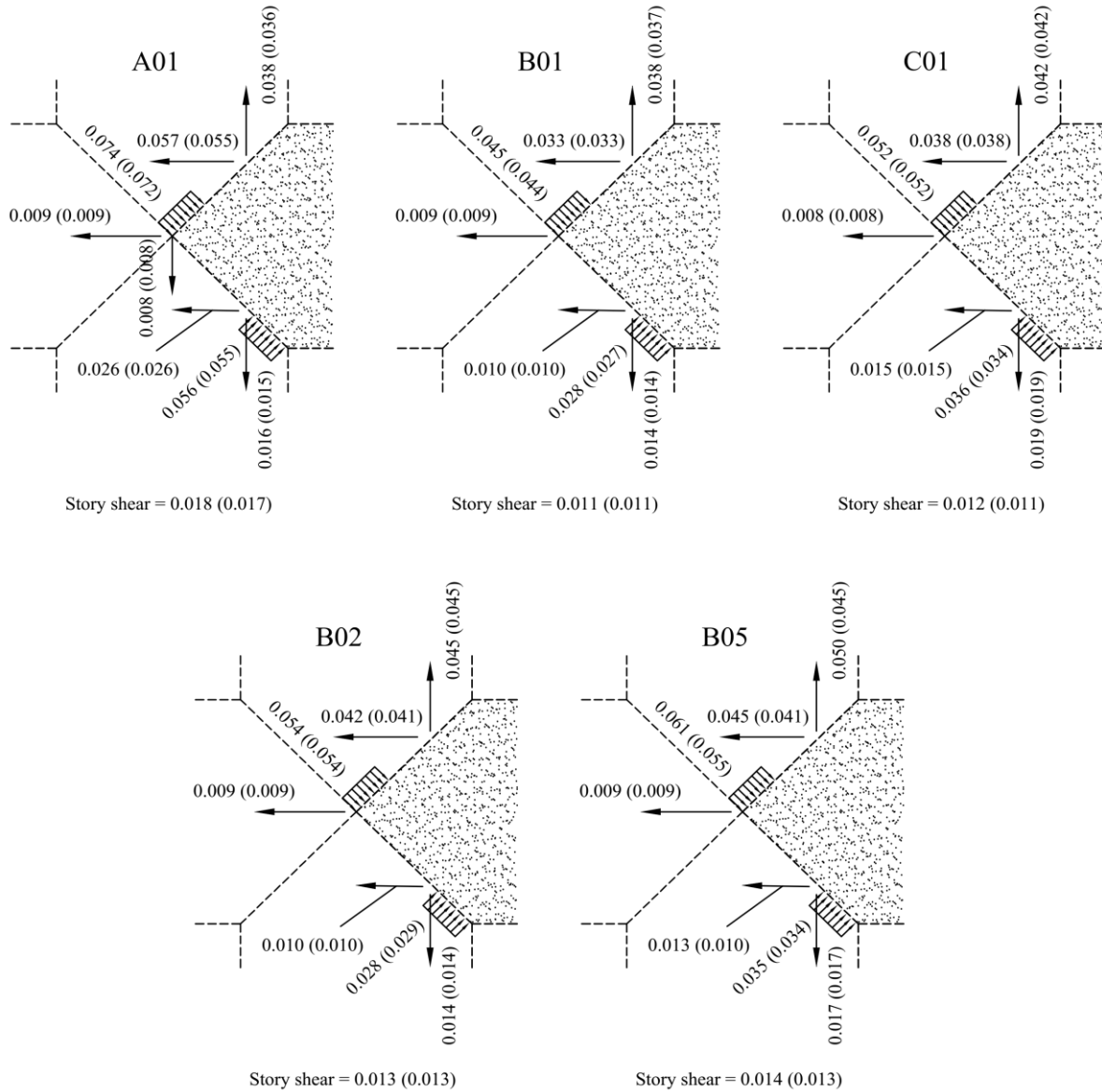
Figure 2.31. Predicted story shear of the five specimens with normal bond condition

(number in parentheses is determined by Shiohara's numerical method)

2.5 Modification of the new model to investigate the monotonic response of the interior beam-column joints with different depth and width of beams and columns and normal bond condition

The procedure in this section is similar to that of section 2.2 except the following modifications:

2.5.1 Concrete struts

Displacements in Figure 2.32 named as δ_{com_1}, δ_{com_3}, δ_{ten_6}, δ_{ten_8} are used for determining strain distribution in diagonal orientation, can be calculated as below:

$$\delta_{com\_1} = \frac{d_x d_z}{\sqrt{d_x^2 + d_z^2}} \left(\frac{\Delta_{x1}}{d_z} + \frac{\Delta_{z1}}{d_x} - \frac{\varphi_{x1}}{2} + \frac{\varphi_{z1}}{2} + \varphi_0 \right) \tag{2.103}$$

$$\delta_{com\_3} = \frac{d_x d_z}{\sqrt{d_x^2 + d_z^2}} \left(\frac{\Delta_{x2}}{d_z} + \frac{\Delta_{z2}}{d_x} + \frac{\varphi_{x2}}{2} - \frac{\varphi_{z2}}{2} + \varphi_0 \right) \tag{2.104}$$

$$\delta_{ten\_6} = \frac{d_x d_z}{\sqrt{d_x^2 + d_z^2}} \left(\frac{\Delta_{x1}}{d_z} + \frac{\Delta_{z1}}{d_x} + \frac{\varphi_{x1}}{2} - \frac{\varphi_{z1}}{2} \right) \tag{2.105}$$

$$\delta_{ten\_8} = \frac{d_x d_z}{\sqrt{d_x^2 + d_z^2}} \left(\frac{\Delta_{x2}}{d_z} + \frac{\Delta_{z2}}{d_x} - \frac{\varphi_{x2}}{2} + \frac{\varphi_{z2}}{2} \right) \tag{2.106}$$

Similarly, displacements in Figure 2.33 named as δ_{com_2}, δ_{com_4}, δ_{ten_5}, δ_{ten_7} are used for determining strain in directions perpendicular to diagonals, can be calculated as below:

$$\delta_{com\_2} = \frac{2d_z \Delta_{x1} + 2d_x \Delta_{z2} - d_z^2 \varphi_{x1} - d_x^2 \varphi_{z2}}{2\sqrt{d_x^2 + d_z^2}} \tag{2.107}$$

$$\delta_{com\_4} = \frac{2d_z \Delta_{x2} + 2d_x \Delta_{z1} + d_z^2 \varphi_{x2} + d_x^2 \varphi_{z1}}{2\sqrt{d_x^2 + d_z^2}} \tag{2.108}$$

$$\delta_{ten\_5} = \frac{2d_z \Delta_{x1} + 2d_x \Delta_{z2} + d_x^2 \varphi_{x1} + d_z^2 \varphi_{z2} - (d_x^2 + d_z^2)\varphi_0}{2\sqrt{d_x^2 + d_z^2}} \tag{2.109}$$

$$\delta_{ten\_7} = \frac{2d_z \Delta_{x2} + 2d_x \Delta_{z1} - d_x^2 \varphi_{x2} - d_z^2 \varphi_{z1} - (d_x^2 + d_z^2)\varphi_0}{2\sqrt{d_x^2 + d_z^2}} \tag{2.110}$$
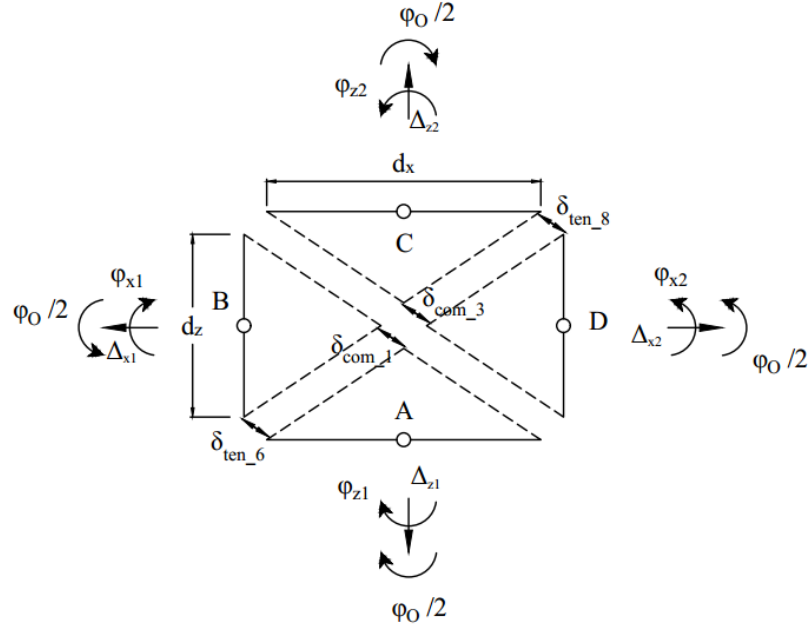
Figure 2.32. Displacement of the center point and corner points in diagonal direction
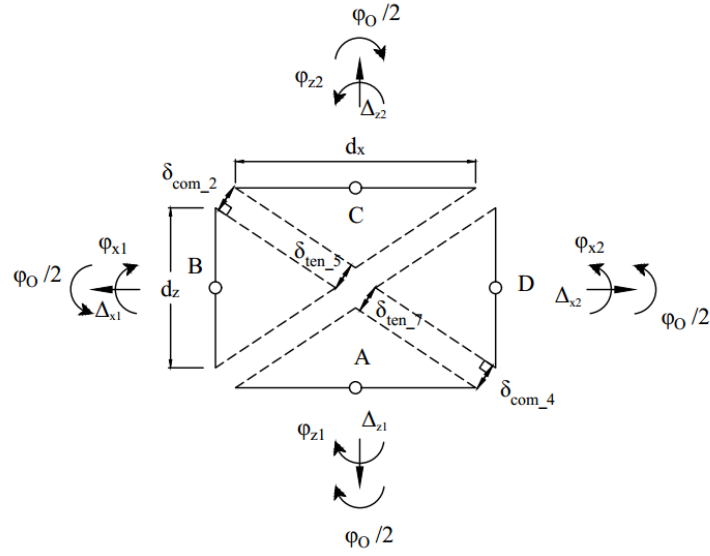
Figure 2.33. Displacement of the center point and corner points in orientation perpendicular-to-diagonal direction

Length of concrete struts (l_c and l_t) were determined in (2.71 and (2.72).
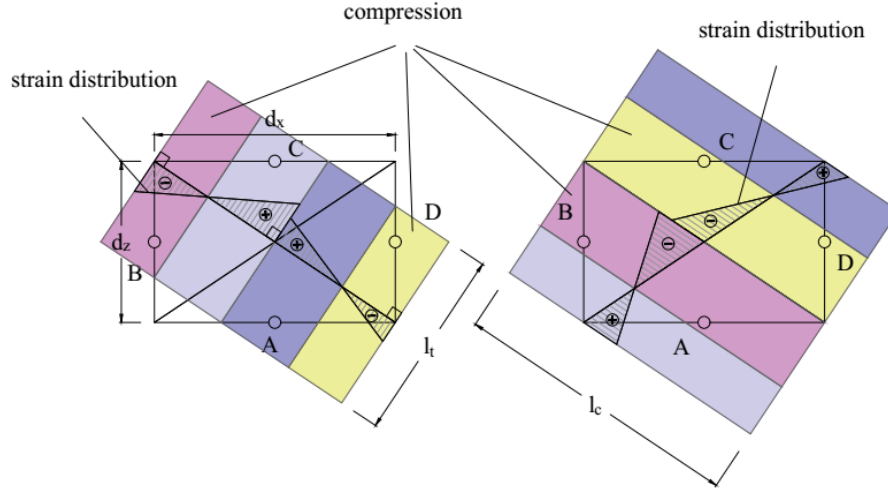
Figure 2.34. Illustration of concrete strut length

These coefficients are utilized to compute strut widths w_{Ci} and w_{Cj} depicted in Figure 2.35 as below if the struts are perpendicular to diagonals:

$$w_{Ci} = \xi_i \frac{d_{dia}}{2} \qquad (2.111)$$

$$w_{Cj} = \xi_j \frac{d_{dia}}{2} \qquad (2.112)$$

If the struts are parallel to diagonals, then:

$$w_{Ci} = \xi_i \frac{d_x d_z}{d_{dia}} \qquad (2.113)$$

$$w_{Cj} = \xi_j \frac{d_x d_z}{d_{dia}} \qquad (2.114)$$
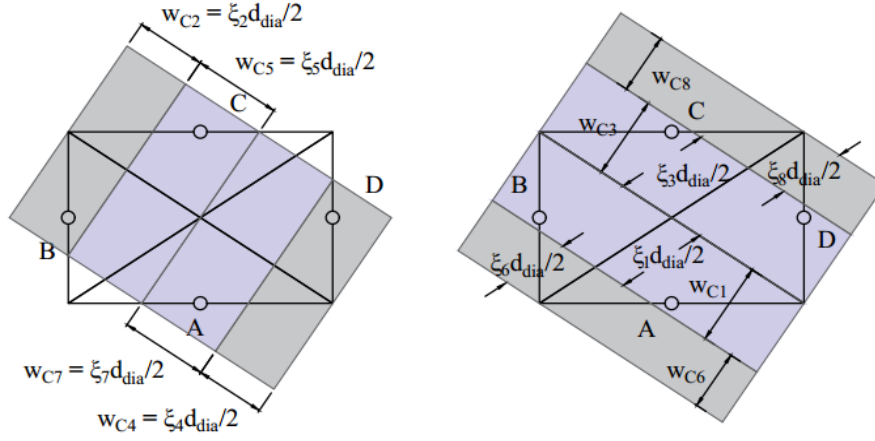
Figure 2.35. Width of concrete struts

2.5.2   Bar springs

Lengths of bar springs were defined as follows:

$$l_{T1} = l_{T2} = l_{T3} = l_{T4} = \frac{d_x}{2} \tag{2.115}$$

$$l_{T6} = l_{T7} = l_{T8} = l_{T9} = \frac{d_z}{2} \tag{2.116}$$

$$l_{T5} = g_x d_x \tag{2.117}$$

$$l_{T10} = d_z \tag{2.118}$$

where l_{T1}, l_{T2}, l_{T3}, l_{T4}, l_{T5}, l_{T6}, l_{T7}, l_{T8}, l_{T9}, and l_{T10} are length of bar spring T_1, T_2, T_3, T_4, T_5, T_6, T_7, T_8, T_9, and T_{10} respectively, as shown in Figure 2.36.
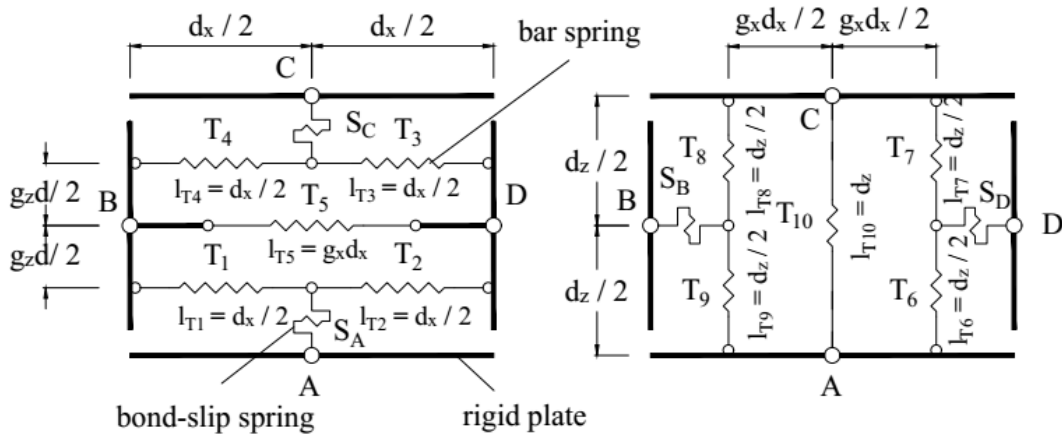
Figure 2.36. Definition of bar springs of the joint element with normal geometric properties

61

2.5.3 Joint compatibility and stiffness

The definition of the joint compatibility and stiffness is the same with that defined in section 2.3.4 except the following changes in matrix $\mathbf{B_1}$.

$$\mathbf{B_1} = \begin{bmatrix}
\cos\alpha & 0 & \sin\alpha & 0 & \eta_{15} & 0 & \eta_{17} & 0 & \eta_{19} \\
\sin\alpha & 0 & 0 & \cos\alpha & \eta_{25} & 0 & 0 & \eta_{28} & \eta_{29} \\
0 & \cos\alpha & 0 & \sin\alpha & 0 & \eta_{36} & 0 & \eta_{38} & \eta_{39} \\
0 & \sin\alpha & \cos\alpha & 0 & 0 & \eta_{46} & \eta_{47} & 0 & \eta_{49} \\
\sin\alpha & 0 & 0 & \cos\alpha & \eta_{55} & 0 & 0 & \eta_{58} & \eta_{59} \\
\cos\alpha & 0 & \sin\alpha & 0 & \eta_{65} & 0 & \eta_{67} & 0 & \eta_{69} \\
0 & \sin\alpha & \cos\alpha & 0 & 0 & \eta_{76} & \eta_{77} & 0 & \eta_{79} \\
0 & \cos\alpha & 0 & \sin\alpha & 0 & \eta_{86} & 0 & \eta_{88} & \eta_{89} \\
1 & 0 & 0 & 0 & \dfrac{g_z d_z}{2} & 0 & \dfrac{(1-g_z)d_z}{2} & 0 & \dfrac{(1-g_z)d_z}{2} \\
0 & 1 & 0 & 0 & 0 & \dfrac{g_z d_z}{2} & -\dfrac{(1-g_z)d_z}{2} & 0 & -\dfrac{(1-g_z)d_z}{2} \\
0 & 1 & 0 & 0 & 0 & -\dfrac{g_z d_z}{2} & 0 & -\dfrac{(1-g_z)d_z}{2} & \dfrac{(1-g_z)d_z}{2} \\
1 & 0 & 0 & 0 & -\dfrac{g_z d_z}{2} & 0 & 0 & \dfrac{(1-g_z)d_z}{2} & -\dfrac{(1-g_z)d_z}{2} \\
1 & 1 & 0 & 0 & 0 & 0 & 0 & 0 & 0 \\
0 & 0 & 1 & 0 & 0 & -\dfrac{(1-g_x)d_x}{2} & \dfrac{g_x d_x}{2} & 0 & -\dfrac{(1-g_x)d_x}{2} \\
0 & 0 & 0 & 1 & 0 & \dfrac{(1-g_x)d_x}{2} & 0 & \dfrac{g_x d_x}{2} & \dfrac{(1-g_x)d_x}{2} \\
0 & 0 & 0 & 1 & \dfrac{(1-g_x)d_x}{2} & 0 & 0 & -\dfrac{g_x d_x}{2} & -\dfrac{(1-g_x)d_x}{2} \\
0 & 0 & 1 & 0 & -\dfrac{(1-g_x)d_x}{2} & 0 & -\dfrac{g_x d_x}{2} & 0 & \dfrac{(1-g_x)d_x}{2} \\
0 & 0 & 1 & 1 & 0 & 0 & 0 & 0 & 0
\end{bmatrix} \quad (2.119)$$

where α is the are the angle with respect to the orientation of the joint diagonals:

$$\alpha = \arctan\left(\frac{d_z}{d_x}\right) \quad (2.120)$$

and:

$$\eta_{15} = \frac{\beta_1 d_z}{2}\cos\alpha - (1-\beta_1)\frac{d_x}{2}\sin\alpha \quad (2.121)$$

$$\eta_{17} = \left(1 - \beta_1\right)\frac{d_z}{2}\cos\alpha - \frac{\beta_1 d_x}{2}\sin\alpha \tag{2.122}$$

$$\eta_{19} = \left(1 - \beta_1\right)\frac{d_{dia}}{2}\sin 2\alpha \tag{2.123}$$

$$\eta_{25} = -\left(1 - \beta_2\right)\frac{d_z}{2}\sin\alpha + \frac{\beta_2 d_x}{2}\cos\alpha \tag{2.124}$$

$$\eta_{28} = \frac{\beta_2 d_z}{2}\sin\alpha - \left(1 - \beta_2\right)\frac{d_x}{2}\cos\alpha \tag{2.125}$$

$$\eta_{29} = -\beta_2\frac{d_{dia}}{2} + \left(1 - \eta_C\right)d_x\cos\alpha \tag{2.126}$$

$$\eta_{36} = -\frac{\beta_3 d_z}{2}\cos\alpha + \left(1 - \beta_3\right)\frac{d_x}{2}\sin\alpha \tag{2.127}$$

$$\eta_{38} = -\left(1 - \beta_3\right)\frac{d_z}{2}\cos\alpha + \frac{\beta_3 d_x}{2}\sin\alpha \tag{2.128}$$

$$\eta_{39} = \left(1 - \beta_3\right)\frac{d_{dia}}{2}\sin 2\alpha \tag{2.129}$$

$$\eta_{46} = \left(1 - \beta_4\right)\frac{d_z}{2}\sin\alpha - \frac{\beta_4 d_x}{2}\cos\alpha \tag{2.130}$$

$$\eta_{47} = -\frac{\beta_4 d_z}{2}\sin\alpha + \left(1 - \beta_4\right)\frac{d_x}{2}\cos\alpha \tag{2.131}$$

$$\eta_{49} = -\beta_4\frac{d_{dia}}{2} \tag{2.132}$$

$$\eta_{55} = -\frac{\beta_5 d_z}{2}\sin\alpha + \left(1 - \beta_5\right)\frac{d_x}{2}\cos\alpha \tag{2.133}$$

$$\eta_{58} = \left(1 - \beta_5\right)\frac{d_z}{2}\sin\alpha - \frac{\beta_5 d_x}{2}\cos\alpha \tag{2.134}$$

$$\eta_{59} = -\left(1 - \beta_5\right)\frac{d_{dia}}{2} \tag{2.135}$$

$$\eta_{65} = \left(1 - \beta_6\right)\frac{\mathrm{d}_z}{2}\cos\alpha - \frac{\beta_6\,\mathrm{d}_x}{2}\sin\alpha \tag{2.136}$$

$$\eta_{67} = \frac{\beta_6\,\mathrm{d}_z}{2}\cos\alpha - \left(1 - \beta_6\right)\frac{\mathrm{d}_x}{2}\sin\alpha \tag{2.137}$$

$$\eta_{69} = \beta_6\,\frac{\mathrm{d}_{dia}}{2}\sin 2\alpha \tag{2.138}$$

$$\eta_{76} = \frac{\beta_7\,\mathrm{d}_z}{2}\sin\alpha - \left(1 - \beta_7\right)\frac{\mathrm{d}_x}{2}\cos\alpha \tag{2.139}$$

$$\eta_{77} = -\left(1 - \beta_7\right)\frac{\mathrm{d}_z}{2}\sin\alpha + \frac{\beta_7\,\mathrm{d}_x}{2}\cos\alpha \tag{2.140}$$

$$\eta_{79} = -\left(1 - \beta_7\right)\frac{\mathrm{d}_{dia}}{2} \tag{2.141}$$

$$\eta_{86} = -\left(1 - \beta_8\right)\frac{\mathrm{d}_z}{2}\cos\alpha + \frac{\beta_8\,\mathrm{d}_x}{2}\sin\alpha \tag{2.142}$$

$$\eta_{88} = -\frac{\beta_8\,\mathrm{d}_z}{2}\cos\alpha + \left(1 - \beta_8\right)\frac{\mathrm{d}_x}{2}\sin\alpha \tag{2.143}$$

$$\eta_{89} = \beta_8\,\frac{\mathrm{d}_{dia}}{2}\sin 2\alpha \tag{2.144}$$

2.5.4   Verification of experimental study

2.5.4.1 Specimens

Two specimens with regard to C03 and D05 from a series of test of the reinforced concrete joint subassemblages conducted by Shiohara and Kusuhara [43] was adopted in this study for verification. The detailed properties of the materials of specimens are listed in Table 2.7 and illustrated geometrically in Figure 2.37. In specimen C03, the width of the beams was different from that of the columns. In specimen D05, there was a difference between the depth of beams and that of the columns. At each story drift of 0.25%, 0.5%, 1.0%, 1.5%, 2.0%, and 3.0%, two cyclic loadings were applied horizontally.

Table 2.7. Properties of interior joint specimens

Specimen	C03	D05
concrete compressive strength (MPa)	31.0	32.4
beam width x depth (mm)	120 x 240	240 x 170
longitudinal beam bars	3-D13 2-D13	7-D13
bar yielding strength (Mpa)	378	378
bar distant ratio	0.8 0.5	0.72
column width x depth (mm)	240 x 240	240 x 340
longitudinal column bars	5-D13	3-D13
column bar yielding strength (Mpa)	378	378
column bar distant ratio	0.8	0.86
Joint hoops	D6 (two sets)	
Yielding strength of hoops (MPa)	399	
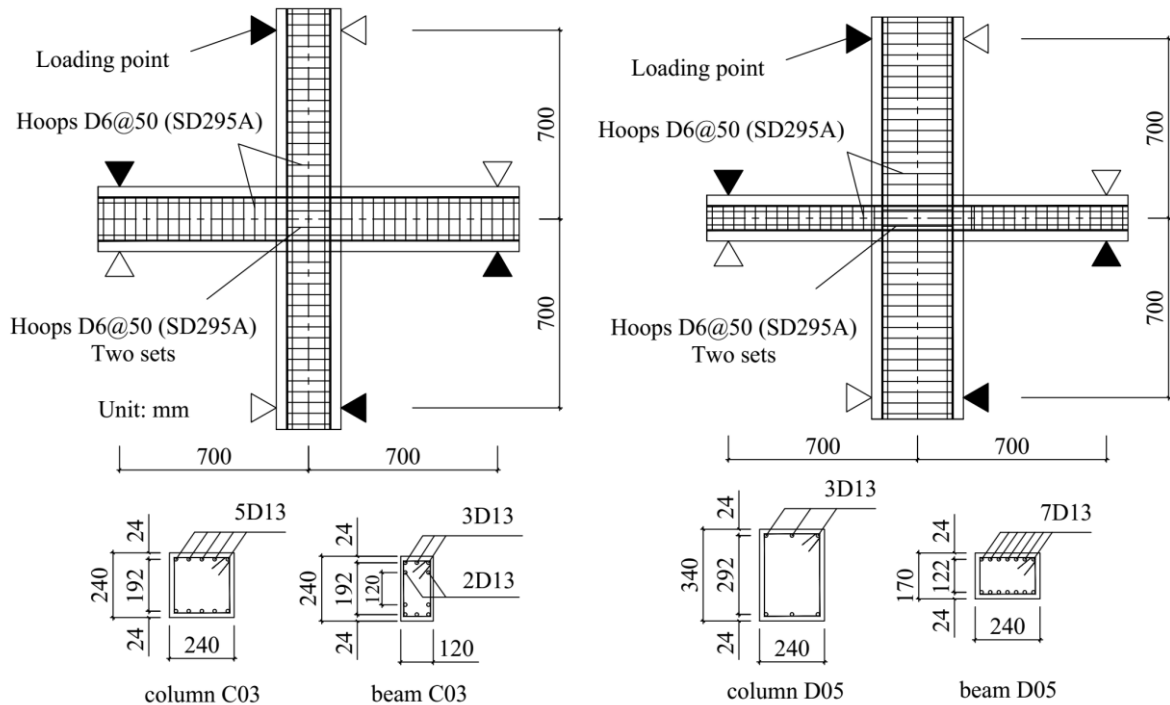
Figure 2.37. Geometric properties of specimen C03 and D05

2.5.5   Discussion of results

2.5.5.1 Load deflection relationship

Table 2.8 compares the maximum story shear predicted by the new joint model ($V_{u\_Analysis}$) to that of the experimental results, at the flexural strength of beam (V_{u_ACI}) by ACI 318 – 08 [2], and computed at the nominal joint shear strength (V_{u_AIJ}) by AIJ 1999 [1]. The relationship of the story shear versus the story drift of all specimens is shown in Figure 2.38.

The analytical result captured well the backbone of the cyclic response of specimen C03 with refer to the story shear versus the story drift relationship. In specimen C03, the maximum story shear from prediction was closer to that from test data than others computed at the flexural strength of beam or at the nominal joint strength. In computation of specimen D05, two cases were analyzed: concrete struts with the orientation followed diagonal direction and concrete struts with the orientation of 45°. The analysis with 45-degree orientation of concrete struts returned in a better correlation with the observed backbone of the cyclic response of specimen D05 than that with diagonal orientation of concrete struts.

2.5.5.2 Comparison to Shiohara's numerical method

A comparison between the computation by the new model and Shiohara's numerical method at the ultimate stage is shown in Figure 2.39. All of the forces were normalized by *0.85tf'$_c$*. In specimen C03, there was a good agreement between the results of the new model and those of Shiohara's numerical method in which the story shear and forces in reinforcements and concrete were mostly the same in the two cases. In specimen D05, in comparison to Shiohara's numerical method, the analysis with diagonal orientation of concrete struts showed a better correlation than that with 45-degree orientation. Difference from Shiohara's numerical method was attributed to the predicted stress in the joint hoop at the ultimate stage which was a half of the joint hoop's yielding strength. In Shiohara's numerical method, the joint hoop was always assumed to yield at the ultimate stage.

Table 2.8. Analytical results of the maximum story shear

	Results	C03	D05[*]	D05[**]
Maximum story shear (kN)	At the flexural strength of beam (column) by ACI 318 - 08[2] (V_{bu})	69.4	75.2	75.2
	Computed at the nominal joint shear strength by AIJ 1999 (V_{ju})	80.4	55.6	55.6
	Test (V_{cmax_Test})	67.4	59.3	59.3
	Analysis ($V_{u\_Analysis}$)	66.0	69.2	58.8
	$V_{cmax\_Analysis} / V_{bu}$	0.95	0.92	0.78
	$V_{cmax\_Analysis} / V_{ju}$	0.82	1.24	1.06
	$V_{cmax\_Analysis} / V_{cmax\_Test}$	0.98	1.17	0.99

[*]: orientation of concrete struts follows diagonal direction

[**]: orientation of concrete struts is 45°
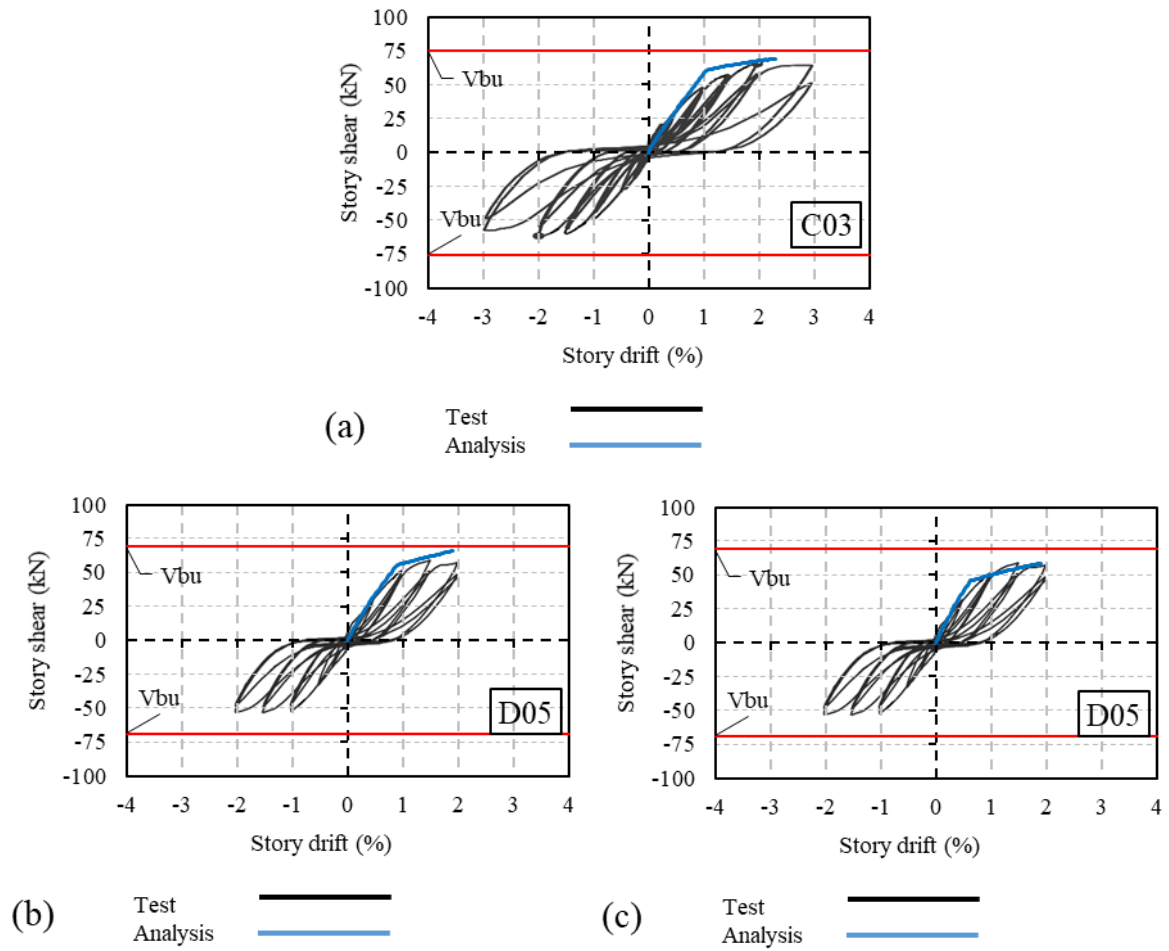
(a) Specimen C03; (b) Specimen D05 with the orientation of concrete struts followed diagonal direction; (c) Specimen D05 with the orientation of concrete struts followed 45°

Figure 2.38. Comparison between experiment and monotonic response of specimen C03 and D05
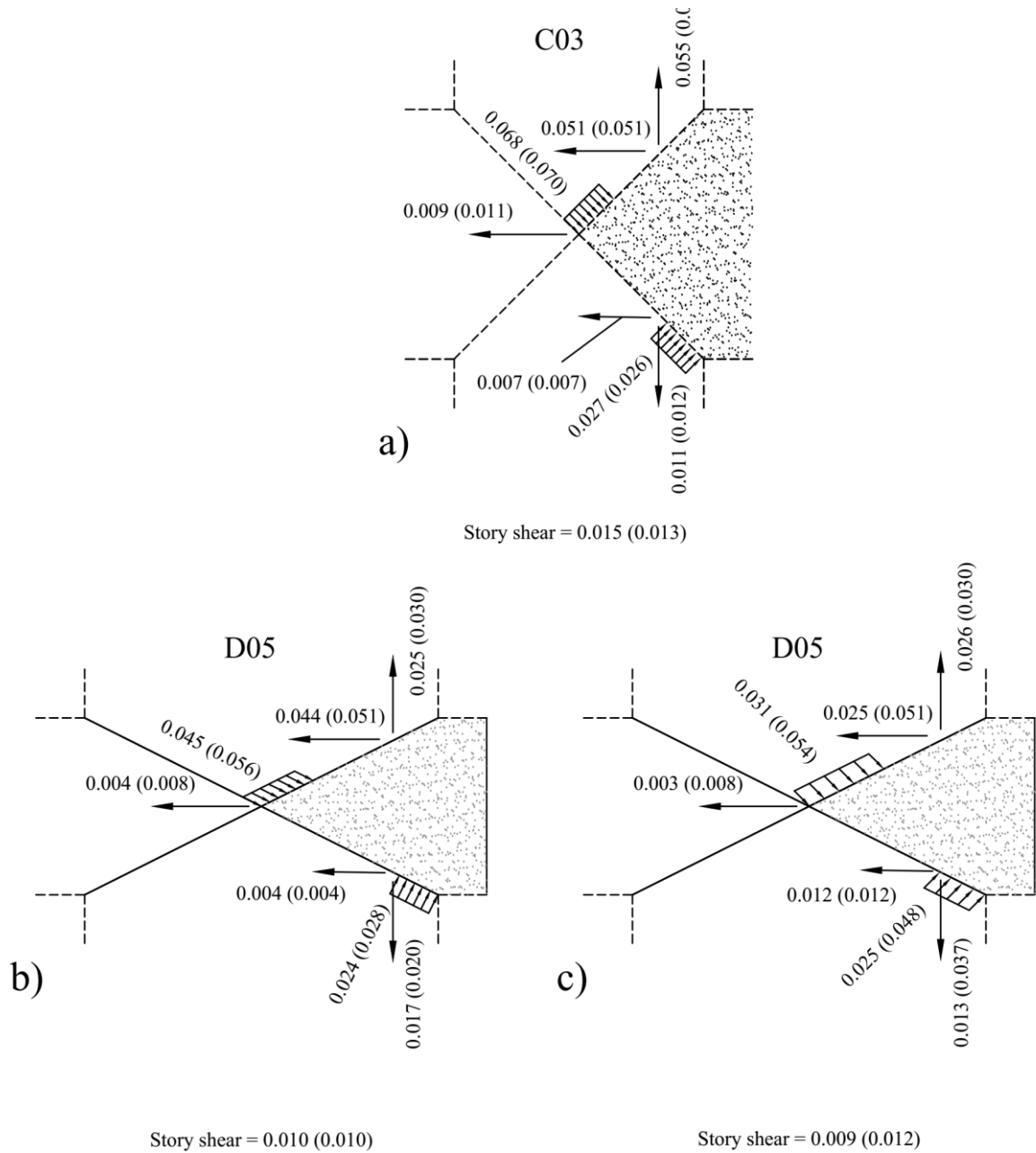
(a) Specimen C03; (b) Specimen D05 with the orientation of concrete struts followed diagonal direction; (c) Specimen D05 with the orientation of concrete struts followed 45°

Figure 2.39. Predicted story shear by new model with perfect bond condition (number in parentheses is determined by Shiohara's numerical method)

2.6   Modification of the new model to investigate the cyclic response of the interior beam-column joints with different depth of beam and column and normal bond condition

There were changes of definition of deformation of concrete struts and constitutive rules of materials under cyclic loadings as below.

2.6.1   Concrete struts

In Shiohara's mechanical model, the rotation of four triangular bodies causes compression and tension zone in concrete as well as generate joint deformations. Strain distribution on diagonal-orientation section of concrete struts in the study is, therefore, determined from displacements of corner points and the joint center. It is noticed that when longitudinal reinforcements in beam and column yield during loading stages, plastic deformation in tensile bars prevent tensile concrete struts near joint corners from returning compression in the next unloading stage. In other word, triangular bodies in the mechanical model cannot close after unloading and even during reverse loading, thus fails to resemble Shiohara failure mode. To solve this problem, it is assumed that during loading stages, four triangular segments expand towards yielding reinforcements as described in Figure 2.40. The expanding lengths are defined from deformation of respective tensile reinforcement as followings:

$$\Delta_{ei} = \frac{1}{g_z}\left(\Delta_{Ti} - \Delta_{Ti}^{P}\right)\ \ (\geq 0)\ \ \ with\ i = 1,2,3,4 \tag{2.145}$$

$$\Delta_{ej} = \frac{1}{g_x}\left(\Delta_{Tj} - \Delta_{Tj}^{P}\right)\ \ (\geq 0)\ \ \ with\ j = 6,7,8,9 \tag{2.146}$$

where Δ_{ei} and Δ_{ej} are expanding lengths towards yielding bar T_i and T_j, and Δ^{P}_{Ti} and Δ^{P}_{Tj} are deformation at yielding strength of those bars respectively.
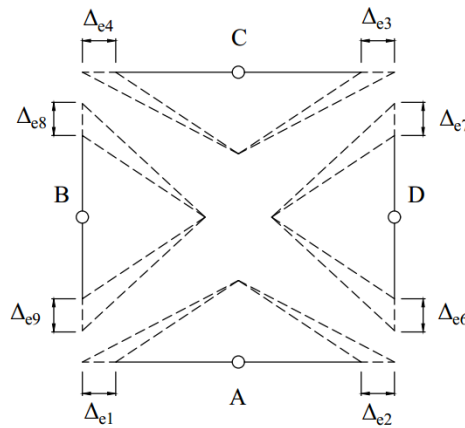
Figure 2.40. Expansion of triangular segments after bar yielding

Displacements in Figure 2.32 named as δ_{com_1}, δ_{com_3}, δ_{ten_6}, δ_{ten_8} are used for determining strain distribution in diagonal orientation, can be calculated as below:

$$\delta_{com\_1} = \frac{d_x d_z}{\sqrt{d_x^2 + d_z^2}} \left(\frac{\Delta_{x1}}{d_z} + \frac{\Delta_{z1}}{d_x} - \frac{\varphi_{x1}}{2} + \frac{\varphi_{z1}}{2} + \varphi_0 \right) \tag{2.147}$$

$$\delta_{com\_3} = \frac{d_x d_z}{\sqrt{d_x^2 + d_z^2}} \left(\frac{\Delta_{x2}}{d_z} + \frac{\Delta_{z2}}{d_x} + \frac{\varphi_{x2}}{2} - \frac{\varphi_{z2}}{2} + \varphi_0 \right) \tag{2.148}$$

$$\delta_{ten\_6} = \frac{d_x d_z}{\sqrt{d_x^2 + d_z^2}} \left(\frac{\Delta_{x1} - \Delta_{e1}}{d_z} + \frac{\Delta_{z1} - \Delta_{e9}}{d_x} + \frac{\varphi_{x1}}{2} - \frac{\varphi_{z1}}{2} \right) \tag{2.149}$$

$$\delta_{ten\_8} = \frac{d_x d_z}{\sqrt{d_x^2 + d_z^2}} \left(\frac{\Delta_{x2} - \Delta_{e3}}{d_z} + \frac{\Delta_{z2} - \Delta_{e7}}{d_x} - \frac{\varphi_{x2}}{2} + \frac{\varphi_{z2}}{2} \right) \tag{2.150}$$

Similarly, displacements in Figure 2.33 named as δ_{com_2}, δ_{com_4}, δ_{ten_5}, δ_{ten_7} are used for determining strain in directions perpendicular to diagonals, can be calculated as below:

$$\delta_{com\_2} = \frac{2d_z \left(\Delta_{x1} - \Delta_{e4} \right) + 2d_x \left(\Delta_{z2} - \Delta_{e8} \right) - d_z^2 \varphi_{x1} - d_x^2 \varphi_{z2}}{2\sqrt{d_x^2 + d_z^2}} \tag{2.151}$$

$$\delta_{com\_4} = \frac{2d_z \left(\Delta_{x2} - \Delta_{e2} \right) + 2d_x \left(\Delta_{z1} - \Delta_{e6} \right) + d_z^2 \varphi_{x2} + d_x^2 \varphi_{z1}}{2\sqrt{d_x^2 + d_z^2}} \tag{2.152}$$

$$\delta_{ten\_5} = \frac{2d_z \Delta_{x1} + 2d_x \Delta_{z2} + d_x^2 \varphi_{x1} + d_z^2 \varphi_{z2} - (d_x^2 + d_z^2)\varphi_0}{2\sqrt{d_x^2 + d_z^2}} \tag{2.153}$$

$$\delta_{ten\_7} = \frac{2d_z \Delta_{x2} + 2d_x \Delta_{z1} - d_x^2 \varphi_{x2} - d_z^2 \varphi_{z1} - (d_x^2 + d_z^2)\varphi_0}{2\sqrt{d_x^2 + d_z^2}} \tag{2.154}$$

2.6.2 Constitutive material model

2.6.2.1 Constitutive steel model

At the unloading point $(\sigma_i, \varepsilon_i)$, the skeleton path employs the initial stiffness E_s again, as shown in Figure 2.41.
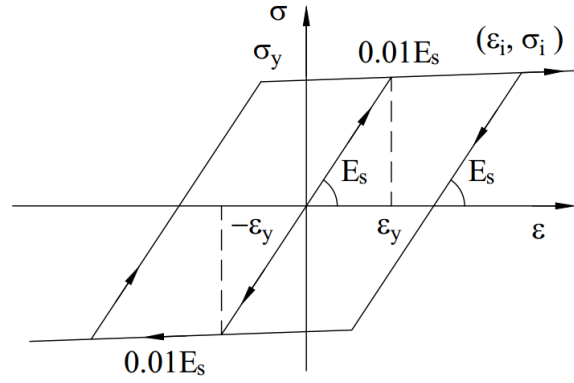
Figure 2.41. Steel hysteresis rule

2.6.2.2 Constitutive bond-slip model

The rules of the unloading and reloading path defined by Eligehausen et al.[25], as shown in Figure 2.42. Here, τ is the bond stress, s is the slip, and τ_{f0} and τ_f are the frictional bond resistance at the first cycle and later cycles respectively.
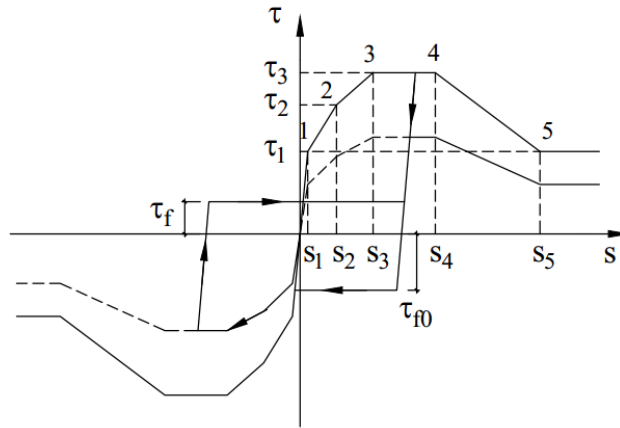
Figure 2.42. Bond-slip hysteresis rule

2.6.2.3 Constitutive concrete model

Unloading paths

The unloading paths were assumed to comprise of two linear lines with the Young modulus of concrete (E_c) used in the slope of the first line, while the second line used a slope equal to $0.071E_c$, as suggested by Palermo and Vecchio [45]. The plastic offset strain ε^c_p at the end of the unloading paths in compression is defined as follows:

72

$$\varepsilon_p^c = \varepsilon_{\max}\left(1 - e^{-\frac{\varepsilon_{\max}}{\varepsilon_{c0}}\alpha_c}\right) \tag{2.155}$$

where ε_{max} is the previously obtained maximum compressive strain in the material, and α_c is a parameter related to the plastic strain amount, which was set to be *0.32* in the analysis carried out in this study.

Coordinates of the deflection point $(\varepsilon_{2i},\ \sigma_{2i})$ were calculated as follows:

$$\varepsilon_{2i} = \frac{\varepsilon_{1i} - 0.071\varepsilon_{pi}^c}{0.929} - \frac{\sigma_{1i}}{0.929E_c} \tag{2.156}$$

$$\sigma_{2i} = \left(\varepsilon_{2i} - \varepsilon_{1i}\right)E_c + \sigma_{1i} \tag{2.157}$$

Similarly, at an arbitrary point in the strut's section with strain ε between ε_{com_i} and zero $(\varepsilon_{com\_i} \le \varepsilon \le 0)$, the unloading path went from the unloading point $(\varepsilon_1,\ \sigma_1)$, point $(\varepsilon_2,\ \sigma_2)$, and point $(\varepsilon_p^c,\ 0)$ correspondingly.

Strain ε_1 was determined from strain ε_{1i} as follows:

$$\varepsilon_1 = \frac{\varepsilon}{\varepsilon_{com\_i}}\varepsilon_{1i} \tag{2.158}$$

σ_1 was computed from ε_1 by the loading skeleton.

It was assumed that when strain ε reached ε_{com_i}, ε_2 and ε_p^c also reached ε_{2i} and ε_{pi}^c respectively. When ε decreased to zero, ε_2 and ε_p^c also decreased to zero. ε_2 and ε_p^c were determined from these assumptions as follows:

$$\varepsilon_p^c = \frac{\varepsilon}{\varepsilon_{com\_i}}\varepsilon_{pi}^c \tag{2.159}$$

$$\varepsilon_2 = \frac{\varepsilon}{\varepsilon_{com\_i}} \varepsilon_{2i} \tag{2.160}$$

σ_2 was also assumed to be proportional to σ_{2i} as follows:

$$\sigma_2 = \frac{\varepsilon}{\varepsilon_{com\_i}} \sigma_{2i} \tag{2.161}$$

In the unloading path with slope Ec, as shown in Figure 2.43(a):

σ_{com_i} was determined from ε_{com_i} as follows:

$$\sigma_{com\_i} = \left(\varepsilon_{com\_i} - \varepsilon_{1i} \right) E_c + \sigma_{1i} \tag{2.162}$$

Stress σ corresponding to strain ε $(\varepsilon_{com\_i} \leq \varepsilon \leq 0)$ of an arbitrary point in the strut's compression section was interpolated so that when σ_{com_i} reached σ_{1i} or σ_{2i}, σ also reached σ_1 or σ_2 respectively, as described in the following equation:

$$\sigma = \frac{\sigma_{com\_i} - \sigma_{2i}}{\sigma_{1i} - \sigma_{2i}} (\sigma_1 - \sigma_2) + \sigma_2 \tag{2.163}$$

If $K_c \varepsilon_{c0} \leq \varepsilon_{1i} < 0$

$$\sigma_{Ci} = \int_0^{\varepsilon_{com\_i}} \left(\frac{\sigma_{com\_i} - \sigma_{2i}}{\sigma_{1i} - \sigma_{2i}} \left\{ \frac{K_c f_c{'}}{\varepsilon_{com\_i}} \left[-\frac{2\varepsilon}{K_c \varepsilon_{c0}} + \left(\frac{\varepsilon}{K_c \varepsilon_{c0}} \right)^2 \right] - \frac{\sigma_{2i} \varepsilon}{\varepsilon_{com\_i}} \right\} + \frac{\sigma_{2i} \varepsilon}{\varepsilon_{com\_i}} \right) d\varepsilon \tag{2.164}$$

$$\beta_{Ci} = \xi_i \left[1 - \frac{\displaystyle\int_0^{\varepsilon_{com\_i}} \left(\frac{\sigma_{com\_i} - \sigma_{2i}}{\sigma_{1i} - \sigma_{2i}} \left\{ K_c f_c{'} \left[-\frac{2\varepsilon^2}{K_c \varepsilon_{c0}} + \frac{\varepsilon^3}{\left(K_c \varepsilon_{c0} \right)^2} \right] - \sigma_{2i} \varepsilon^2 \right\} + \sigma_{2i} \varepsilon^2 \right) d\varepsilon}{\varepsilon_{com\_i} \displaystyle\int_0^{\varepsilon_{com\_i}} \left(\frac{\sigma_{com\_i} - \sigma_{2i}}{\sigma_{1i} - \sigma_{2i}} \left\{ K_c f_c{'} \left[-\frac{2\varepsilon}{K_c \varepsilon_{c0}} + \left(\frac{\varepsilon}{K_c \varepsilon_{c0}} \right)^2 \right] - \sigma_{2i} \varepsilon \right\} + \sigma_{2i} \varepsilon \right) d\varepsilon} \right] \tag{2.165}$$

If $\varepsilon_{1i} < K_c \varepsilon_{c0}$: consider $K_c \varepsilon_{c0} < \varepsilon_1$ or $\varepsilon > \dfrac{K_c \varepsilon_{c0} \varepsilon_{com\_i}}{\varepsilon_{1i}}$ and $\varepsilon_1 < K_c \varepsilon_{c0}$ or $\varepsilon < \dfrac{K_c \varepsilon_{c0} \varepsilon_{com\_i}}{\varepsilon_{1i}}$

$$
\sigma_{Ci} = \int_{0}^{\frac{K_c \varepsilon_{c0} \varepsilon_{com\_i}}{\varepsilon_{1i}}} \left(\frac{\sigma_{com\_i} - \sigma_{2i}}{\sigma_{1i} - \sigma_{2i}} \left\{ \frac{K_c f_c{'}}{\varepsilon_{com\_i}} \left[-\frac{2\varepsilon}{K_c \varepsilon_{c0}} + \left(\frac{\varepsilon}{K_c \varepsilon_{c0}} \right)^2 \right] - \frac{\sigma_{2i} \varepsilon}{\varepsilon_{com\_i}} \right\} + \frac{\sigma_{2i} \varepsilon}{\varepsilon_{com\_i}} \right) d\varepsilon
$$

$$
+ \int_{\frac{K_c \varepsilon_{c0} \varepsilon_{com\_i}}{\varepsilon_{1i}}}^{\varepsilon_{com\_i}} \left(\frac{\sigma_{com\_i} - \sigma_{2i}}{\sigma_{1i} - \sigma_{2i}} \left\{ \frac{K_c f_c{'}}{\varepsilon_{com\_i}} \left[1 + Z_m \left(\varepsilon - K_c \varepsilon_{c0} \right) \right] - \frac{\sigma_{2i} \varepsilon}{\varepsilon_{com\_i}} \right\} + \frac{\sigma_{2i} \varepsilon}{\varepsilon_{com\_i}} \right) d\varepsilon
$$

(2.166)

$$
\beta_{Ci} = \xi_i \left[1 - \frac{\displaystyle\int_{0}^{\frac{K_c \varepsilon_{c0} \varepsilon_{com\_i}}{\varepsilon_{1i}}} \left(\frac{\sigma_{com\_i} - \sigma_{2i}}{\sigma_{1i} - \sigma_{2i}} \left\{ K_c f_c{'} \left[-\frac{2\varepsilon^2}{K_c \varepsilon_{c0}} + \frac{\varepsilon^3}{(K_c \varepsilon_{c0})^2} \right] - \sigma_{2i} \varepsilon^2 \right\} + \sigma_{2i} \varepsilon^2 \right) d\varepsilon + \displaystyle\int_{\frac{K_c \varepsilon_{c0} \varepsilon_{com\_i}}{\varepsilon_{1i}}}^{\varepsilon_{com\_i}} \left(\frac{\sigma_{com\_i} - \sigma_{2i}}{\sigma_{1i} - \sigma_{2i}} \left\{ K_c f_c{'} \left[\varepsilon + Z_m \left(\varepsilon^2 - K_c \varepsilon_{c0} \varepsilon \right) \right] - \sigma_{2i} \varepsilon^2 \right\} + \sigma_{2i} \varepsilon^2 \right) d\varepsilon}{\varepsilon_{com\_i} \left(\displaystyle\int_{0}^{\frac{K_c \varepsilon_{c0} \varepsilon_{com\_i}}{\varepsilon_{1i}}} \left(\frac{\sigma_{com\_i} - \sigma_{2i}}{\sigma_{1i} - \sigma_{2i}} \left\{ K_c f_c{'} \left[-\frac{2\varepsilon}{K_c \varepsilon_{c0}} + \left(\frac{\varepsilon}{K_c \varepsilon_{c0}} \right)^2 \right] - \sigma_{2i} \varepsilon \right\} + \sigma_{2i} \varepsilon \right) d\varepsilon + \displaystyle\int_{\frac{K_c \varepsilon_{c0} \varepsilon_{com\_i}}{\varepsilon_{1i}}}^{\varepsilon_{com\_i}} \left(\frac{\sigma_{com\_i} - \sigma_{2i}}{\sigma_{1i} - \sigma_{2i}} \left\{ K_c f_c{'} \left[1 + Z_m \left(\varepsilon - K_c \varepsilon_{c0} \right) \right] - \sigma_{2i} \varepsilon \right\} + \sigma_{2i} \varepsilon \right) d\varepsilon \right)} \right]
$$

(2.167)

Unloading path with slope 0.071E_c, as shown in Figure 2.43*(b):*

σ_{com_i} was determined from ε_{com_i} as follows:

$$
\sigma_{com\_i} = \left(\varepsilon_{com\_i} - \varepsilon_{2i} \right) 0.071 E_c + \sigma_{2i}
$$

(2.168)

Stress σ corresponding to strain ε *($\varepsilon_{com\_i} \leq \varepsilon \leq 0$)* of an arbitrary point in the strut's compression

section was computed as follows:

$$
\sigma = \left(\varepsilon - \varepsilon_2 \right) 0.071 E_c + \sigma_2 = \frac{\varepsilon}{\varepsilon_{com\_i}} \sigma_{com\_i}
$$

(2.169)

75

$$\sigma_{Ci} = \int_0^{\varepsilon_{com\_i}} \frac{\varepsilon}{\varepsilon_{com\_i}^2} \sigma_{com\_i} d\varepsilon \qquad (2.170)$$

Reloading from tension path

A shown in Figure 2.44, σ_{com_i} was determined from ε_{com_i} as follows:

$$\sigma_{com\_i} = \varepsilon_{com\_i} \frac{\sigma_{1i}}{\varepsilon_{1i}} \qquad (2.171)$$

Stress σ corresponding to strain ε $(\varepsilon_{com\_i} \leq \varepsilon \leq 0)$ of an arbitrary point in the strut's compression section was computed as follows:

$$\sigma = \frac{\sigma_{com\_i}}{\sigma_{1i}} \sigma_1 \qquad (2.172)$$

If $K_c \varepsilon_{c0} \leq \varepsilon_{1i} < 0$

$$\sigma_{Ci} = \int_0^{\varepsilon_{com\_i}} \frac{K_c f_c{}'}{\varepsilon_{1i}} \left[-\frac{2\varepsilon}{K_c \varepsilon_{c0}} + \left(\frac{\varepsilon}{K_c \varepsilon_{c0}} \right)^2 \right] d\varepsilon \qquad (2.173)$$

$$\beta_{Ci} = \xi_i \left[1 - \frac{\displaystyle\int_0^{\varepsilon_{com\_i}} \left(-\frac{2\varepsilon^2}{K_c \varepsilon_{c0}} + \frac{\varepsilon^3}{(K_c \varepsilon_{c0})^2} \right) d\varepsilon}{\varepsilon_{com\_i} \displaystyle\int_0^{\varepsilon_{com\_i}} \left(-\frac{2\varepsilon}{K_c \varepsilon_{c0}} + \left(\frac{\varepsilon}{K_c \varepsilon_{c0}} \right)^2 \right) d\varepsilon} \right] \qquad (2.174)$$

If $\varepsilon_{1i} < K_c \varepsilon_{c0}$: consider $K_c \varepsilon_{c0} < \varepsilon_1$ or $\varepsilon > \dfrac{K_c \varepsilon_{c0} \varepsilon_{com\_i}}{\varepsilon_{1i}}$ and $\varepsilon_1 < K_c \varepsilon_{c0}$ or $\varepsilon < \dfrac{K_c \varepsilon_{c0} \varepsilon_{com\_i}}{\varepsilon_{1i}}$

$$\sigma_{Ci} = \int_0^{\frac{K_c \varepsilon_{c0} \varepsilon_{com\_i}}{\varepsilon_{1i}}} \frac{K_c f_c{}'}{\varepsilon_{1i}} \left[-\frac{2\varepsilon}{K_c \varepsilon_{c0}} + \left(\frac{\varepsilon}{K_c \varepsilon_{c0}} \right)^2 \right] d\varepsilon + \int_{\frac{K_c \varepsilon_{c0} \varepsilon_{com\_i}}{\varepsilon_{1i}}}^{\varepsilon_{com\_i}} \frac{K_c f_c{}'}{\varepsilon_{1i}} \left[1 + Z_m (\varepsilon - K_c \varepsilon_{c0}) \right] d\varepsilon \qquad (2.175)$$

76

$$\beta_{Ci} = \xi_i \left[1 - \frac{\int\limits_0^{\frac{K_c \varepsilon_{c0} \varepsilon_{com\_i}}{\varepsilon_{1i}}} \left[-\frac{2\varepsilon^2}{K_c \varepsilon_{c0}} + \frac{\varepsilon^3}{\left(K_c \varepsilon_{c0}\right)^2} \right] d\varepsilon + \int\limits_{\frac{K_c \varepsilon_{c0} \varepsilon_{com\_i}}{\varepsilon_{1i}}}^{\varepsilon_{com\_i}} \left[\varepsilon + Z_m \left(\varepsilon^2 - K_c \varepsilon_{c0} \varepsilon \right) \right] d\varepsilon}{\varepsilon_{com\_i} \left(\int\limits_0^{\frac{K_c \varepsilon_{c0} \varepsilon_{com\_i}}{\varepsilon_{1i}}} \left[-\frac{2\varepsilon}{K_c \varepsilon_{c0}} + \left(\frac{\varepsilon}{K_c \varepsilon_{c0}} \right)^2 \right] d\varepsilon + \int\limits_{\frac{K_c \varepsilon_{c0} \varepsilon_{com\_i}}{\varepsilon_{1i}}}^{\varepsilon_{com\_i}} \left[1 + Z_m \left(\varepsilon - K_c \varepsilon_{c0} \right) \right] d\varepsilon \right)} \right] \tag{2.176}$$
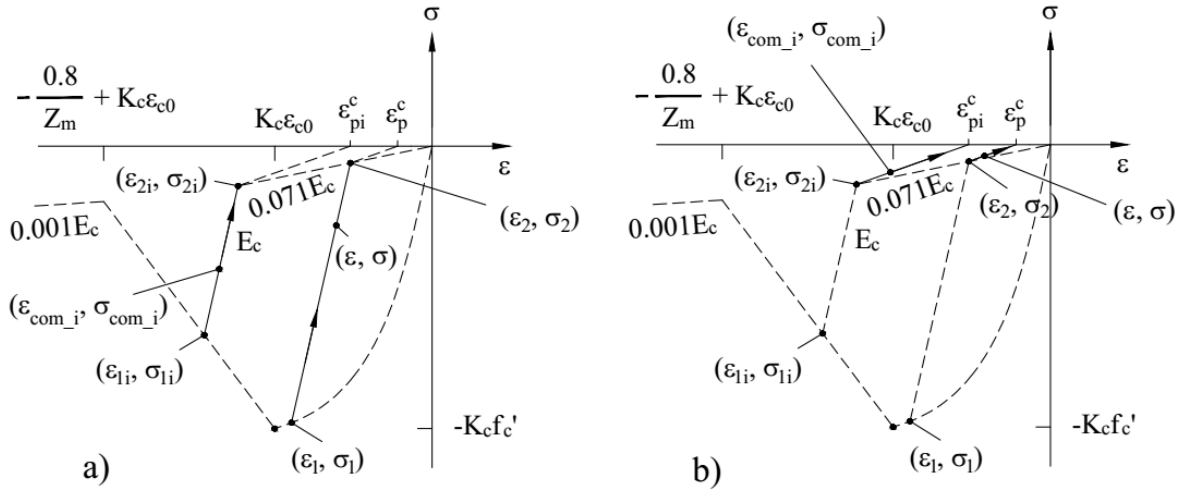
Figure 2.43. Constitutive rule of concrete under unloading in compression
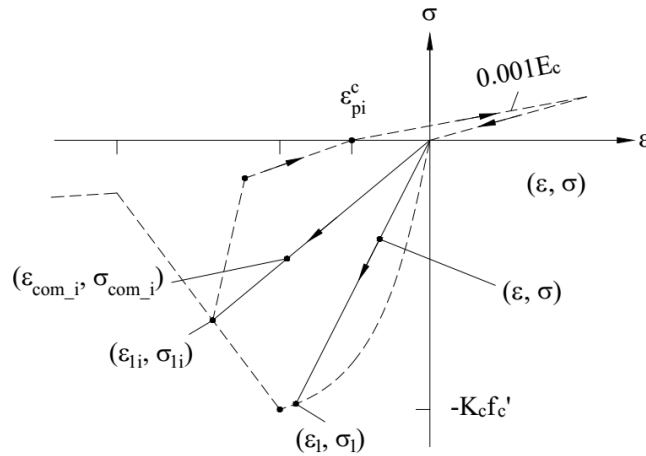
Figure 2.44. Constitutive rule of concrete under reloading from tension to compression

2.7 Verification of experimental study

2.7.1.1 Specimens

Five specimens (A01, B01, B02, B05, and C01) in section 2.3.8.1 and two specimens in section 2.5.4.1 (C03 and D05) were chosen for verification. In specimen D05, the orientation of the concrete struts followed the direction of the joint diagonals.

2.7.1.2 Load deflection relationship

Relationships of story shear versus story drift of five specimens are described in Figure 2.45 to Figure 2.47. Results indicated good correlations between maximum story shear predicted by the new model with observation. The differences of maximum story shear between observation and computation based on the new joint model were under 7% in all specimens. In specimen B02 and B05, the computed maximum story shear had a good agreement with the story shear established at the shear strength determined from AIJ 1999 and the observed maximum story shear. Degradation of story shear at 2% of A01, B02, B05, C01, C03 and D05 was predicted well although there was disagreement in B01 with the ultimate point at 3% of positive path instead of 2% like prediction.

2.7.1.3 Failure mode

Based on the observation, the failure of specimen B01 and B02 was the joint shear failure following beam yielding, and the failure of other specimens was the joint shear failure. The analysis captured well these aspects. To understand more specifically joint performance, failure modes of specimens are evaluated with considering failure of crushing concrete struts, yielding failure of reinforcements, and bond failure of reinforcing bars. The crushing of concrete struts was predicted when the computed concrete average stress degraded. The bond failure of reinforcement was captured when the bond stress exceeded $2.5f'_c$. The results of the joint failure modes were described in Table 2.9. In all specimen, there was no bond failure. The yielding of reinforcements in specimen A01 and C01 showed a good agreement with test data. The reinforcement yielding in specimen B01 was also predicted well although there was an overestimation of the story drift at the hoop yielding. For specimen B02, the failure of the system is due to yielding of longitudinal bars in beams, columns, and joint hoops. In specimen B05 with the same dimensions of B02, because of reinforcing two bars D13 in column, yielding of bars of columns at the failure mode disappears. Although the observation shows no yielding

in longitudinal bars in columns of specimen B02 but B05 which is different from calculation, prediction of yielding in longitudinal bars in beam and joint hoops is confirmed well. The analysis predicted only the yielding of the column bar in specimen D05 which was also confirmed by experiment.

2.7.1.4 Comparison to Shiohara's numerical method

A comparison between the computation by the new model and Shiohara's numerical method [5] at the ultimate stage is shown in Figure 2.48. All of the forces were normalized by *0.85tf'$_c$*. In most specimens except D05, there was a good agreement between the results of the new model and those of the Shiohara's numerical method in which the story shear and forces in reinforcements and concrete were mostly the same in the two cases. The significant differences in specimen D05 were attributed to the assumption of reinforcement yielding in Shiohara's numerical method which assumed yielding for bar spring T_3 and hoop spring T_5. However, the observation showed that there was only yielding of the column bars in specimen D05 which was similar to the prediction from the new model.
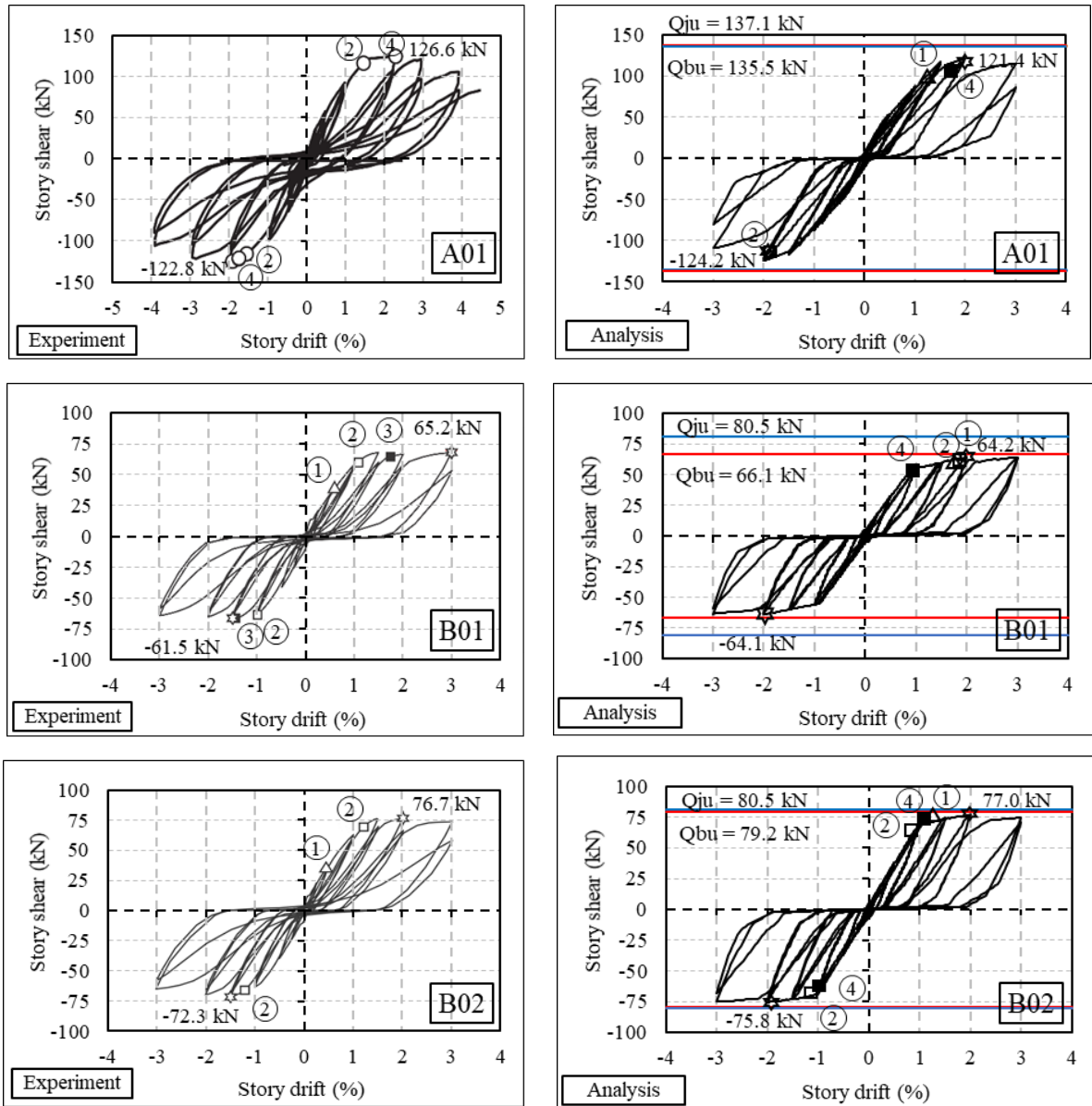
Figure 2.45. Story shear versus story drift relationship of specimen A01, B01, and B02
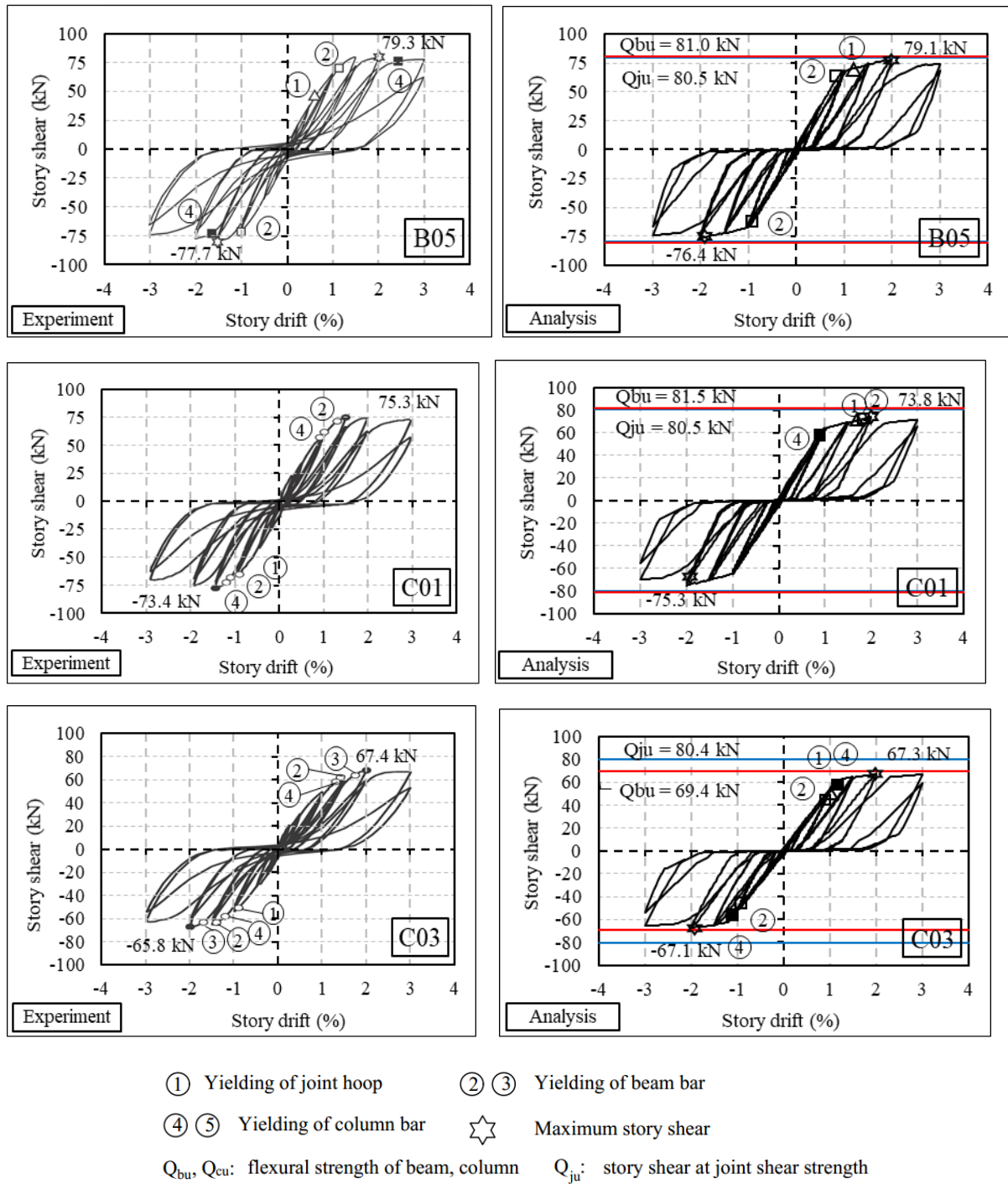
Figure 2.46. Story shear versus story drift relationship of specimen B05, C01, and C03
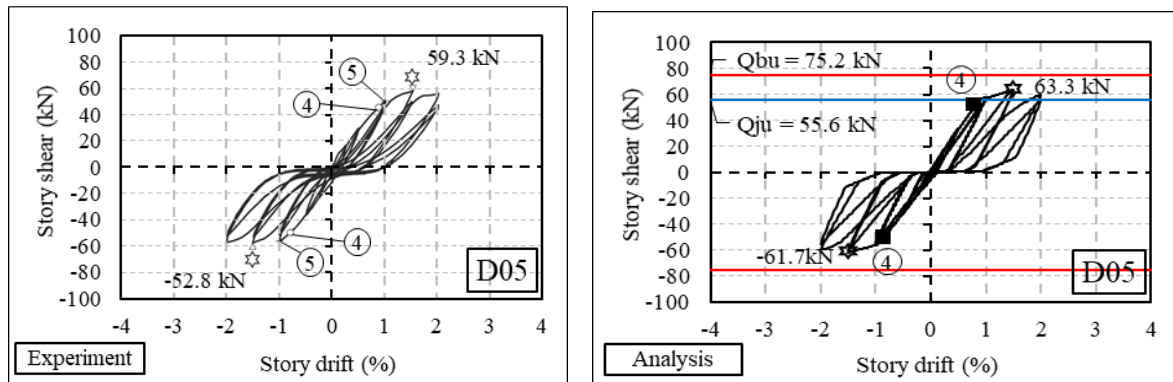
Figure 2.47. Story shear versus story drift relationship of specimen D05

Table 2.9. Failure modes of interior joint specimens under cyclic loadings

Specimen	Failure mode
A01	Yielding of beam longitudinal bars Yielding of column longitudinal bars Yielding of joint hoops
B01	Yielding of beam longitudinal bars Yielding of column longitudinal bars Yielding of joint hoops
B02	Yielding of bars of beam Yielding of bars of column Yielding of joint hoops
B05	Yielding of bars of beam Yielding of joint hoops Concrete strut crushing
C01	Yielding of beam longitudinal bars Yielding of column longitudinal bars Yielding of joint hoops Concrete strut crushing
C03	Yielding of bars of beam Yielding of bars of column Yielding of joint hoops
D05	Yielding of bars of column
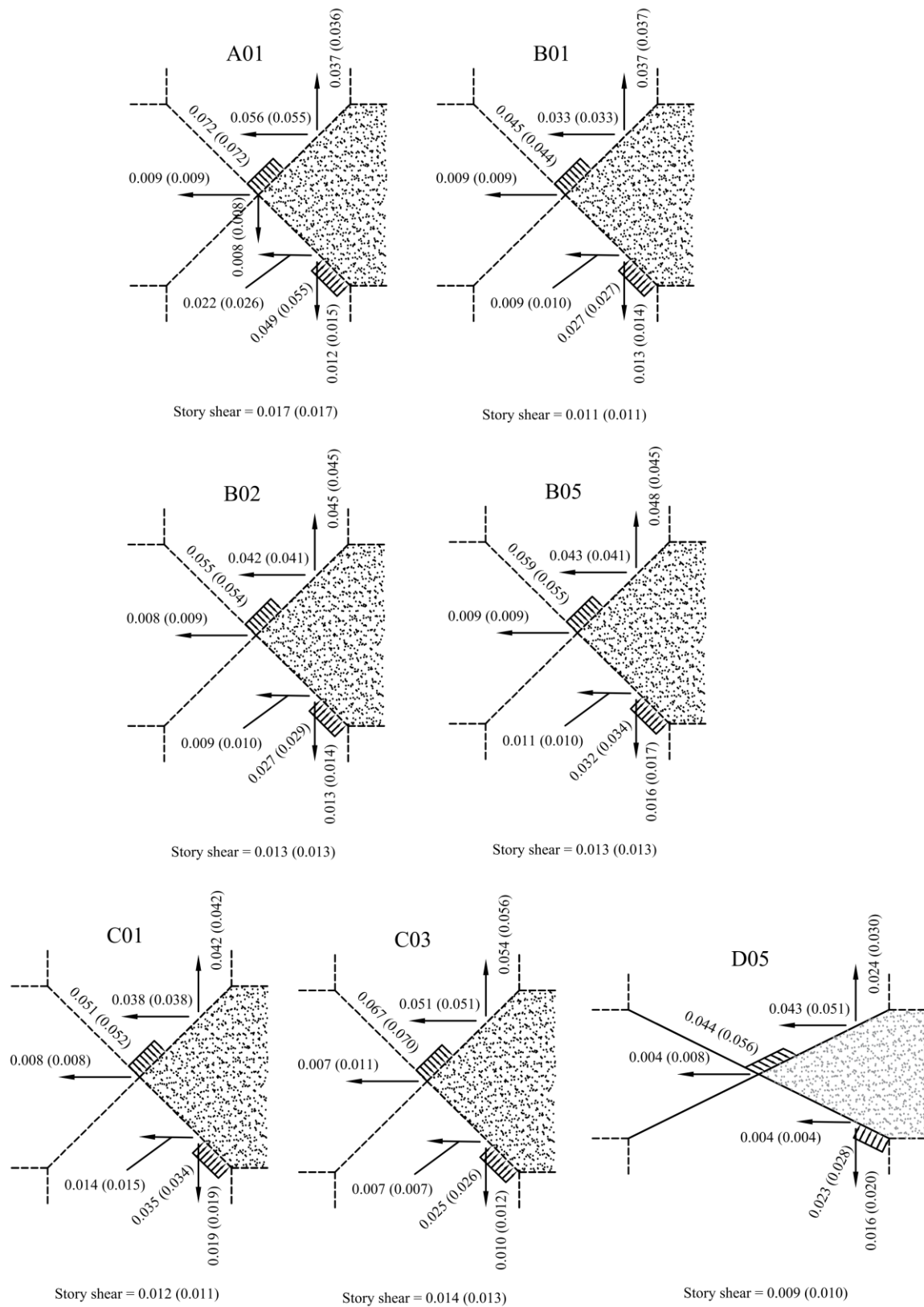
Figure 2.48. Predicted story shear of the seven specimens

(number in parentheses is determined by Shiohara's numerical method)

83

2.8   Conclusion

A new model has been proposed for simulating beam column connections under cyclic loadings. The model successfully develops SMM from predicting joint moment capacity into a practical joint element. Concrete struts and bar springs were defined from rotation of rigid bodies in Shiohara mechanism so that their deformation characterized this rotation while bond slip springs represented the anchorage loss along longitudinal bars within the joint region. The new joint element, thus, reserved the equilibrium relationships in SMM; furthermore, it established successfully a compatible relationship of joint deformations with deformations of joint components which was neglected in SMM. Employing concrete strut was an aspect which reserved the original idea of SMM and made the present model differ from other multi-spring joint elements. In the theory, stress in compressive concrete at the failure stage was assumed to attain 85% of concrete compressive strength (recommended by ACI 318); nonetheless, the proposed model developed this aspect generally since a linear distribution of strain on strut section was adopted and stress distribution was then determined based on a concrete constitutive law. A new set of joint deformations was also introduced for the new model with respect to nine independent components having a compatible relationship with deformation of bar springs and concrete struts. Bond-slip stiffness was considered and integrated into bar stiffness to establish the joint general stiffness.

The new joint model was verified in case of interior joints by simulating response of several interior subassemblage specimens with different sizes and reinforcing details under cases: the monotonic response of the interior joints with identical beam-column depth and perfect bond condition, the monotonic response of the interior joints with identical beam-column depth and normal bond condition, the monotonic response of the interior joints without identical beam-column depth, and the cyclic response of the interior joints with normal geometric properties and normal bond condition. In each case, failure mode of a joint was studied in details regarding failure caused by yielding of longitudinal bars in beams, columns, joint hoops, crushing of concrete, and bond failure of reinforcing bars. Comparison to Shiohara's numerical method in computing internal forces in a joint at the ultimate stage was also carried out to confirm the reliability of the new joint element.

Chapter 3 Application on Investigation Cyclic Response of Exterior Joints, Knee Joints and RC Frame

3.1 Abstract

In this chapter, applications of the new joint model on investigating cyclic response of the exterior joints, knee joint, and a two dimensional reinforced concrete frame were implemented. Firstly, a new model for exterior joints was built based on some modifications on the interior joint element proposed in Chapter 2. The cyclic response of four exterior joint specimens analyzed by the new exterior joint model was verified by test data. Secondly, the interior joint model in Chapter 2 was used without modifications to investigate the cyclic response of three knee joint specimens. The computational results were then evaluated by experimental data which indicated some disagreements. Several recommendations on future researches to improve the reliability of the new joint model on studying performance of knee joint were also proposed. Finally, an application of the new interior joint and exterior joint model on investigating the performance of a 2D RC frame under reversed loading was conducted. Results showed a good prediction of the new joint models in predicting the overall response of the frame.

3.2 Modification of the new model to investigate the cyclic response of exterior joints

3.2.1 The hinging model for exterior joint

Experiments on RC beam-column exterior joints by Shiohara and Kusuhara [46] indicated the existence of diagonal cracks on the joint surface for joint failure mode, as shown in Figure 3.1. The location of the diagonal cracks was governed by the anchorage length of the longitudinal reinforcing bars in the beams for both anchorage type U or type plate as shown in Figure 3.2(a). As illustrated in Figure 3.2(b), cracks developed from the top and bottom edge of the contacting face between the joint and the beam to the anchorage points which were located by the distance $\eta_T d_x$ from the beam face. The extension of crack on the contacting face between the columns and the joint was represented by the length $\eta_C d_x$.
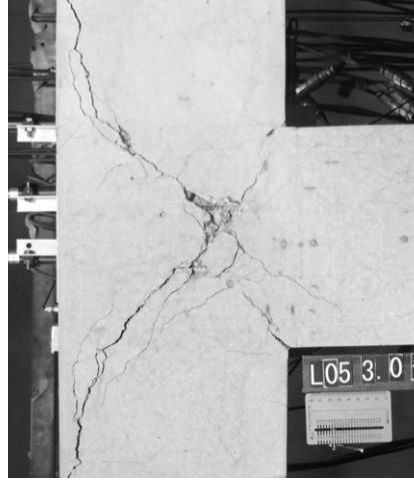
Figure 3.1. Observed crack after test of an exterior joint
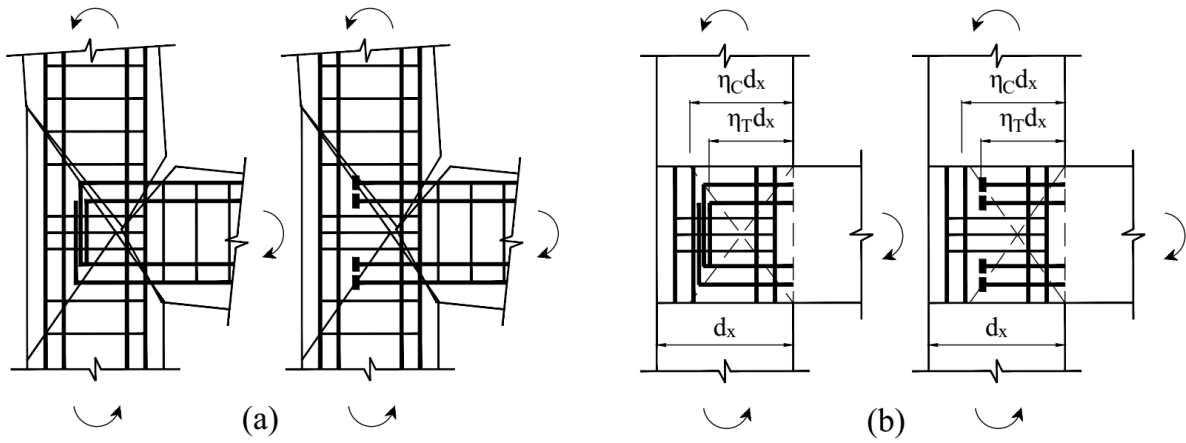
Figure 3.2. Crack pattern of exterior joint after failure
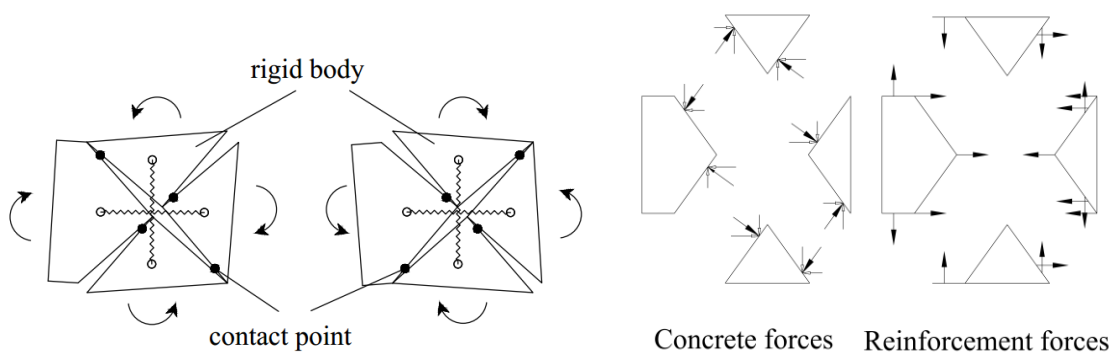
Figure 3.3. Hinging model of exterior joints and resultant forces in concrete and reinforcements

Shiohara's hinging model for interior joint was extended to exterior joint in which four free bodies connected to each other by reinforcements and there were equilibriums of forces on each

body as shown in Figure 3.3. Similar to section 2.2, the joint was considered to be elastic before cracking. After cracking, bar springs and concrete struts were used to simulate the resultant forces in reinforcements and concrete applied to the four free bodies that was represented as rigid plates. The deformation of bar springs and concrete struts, on the other hand, were computed by the rotation of the four free bodies of the hinging model.

3.2.2 Geometric properties of the joint element

Figure 3.4 shows the geometric properties of an exterior joint element. The other definition regarding the compatibility and the joint elastic stiffness is similar to the definition in Section 2.2.
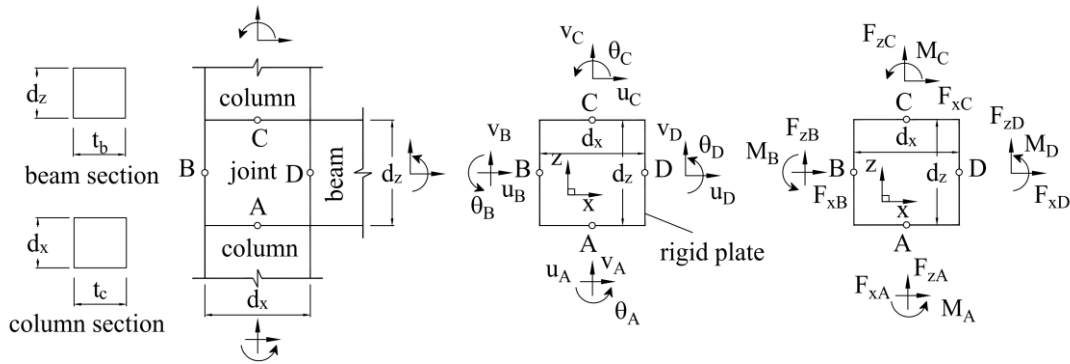
Figure 3.4. Geometric properties of the exterior joint model

3.2.3 Concrete struts

The four free bodies in the joint hinging model rotated and caused compressive zones and tensile zones in concrete under loading. Based on the observation of the cyclic tests and the idealized kinematic model at the ultimate stage of the exterior joints [46], these zones were illustrated in Figure 3.5(a). In this section, the "diagonal" referred to the diagonals of the rectangular with the length $\eta_C d_x$ and the height d_z where the cracks developed. The concept of the diagonal cracks of Shiohara's joint hinging mechanism [5, 6] for the interior joints was extended to the exterior joints in which there were flows of concrete compressive force in the diagonal direction. The flow of force near corners was assumed to be perpendicular to the diagonals. The width of the concrete tensile and compressive zones was determined by the displacement of the corners and the center of the rectangular ($\eta_C d_x$) x d_z in the direction of the abovementioned force flows.

In Figure 3.5(b), deformation δ_{com_1}, δ_{com_3}, δ_{com_6}, and δ_{com_8} in the diagonal direction and δ_{ten_2}, δ_{ten_4}, δ_{ten_5}, and δ_{ten_7} in the direction perpendicular to the diagonal were calculated as follows:

$$\delta_{com\_1} = \frac{d_x d_z}{\sqrt{\eta_C^2 d_x^2 + d_z^2}} \left(\frac{\eta_C \Delta_{x1}}{d_z} + \frac{\Delta_{z1}}{d_x} - \left(1 - \frac{\eta_C}{2}\right)\varphi_{x1} + \frac{\varphi_{z1}}{2} + \eta_C \varphi_0 \right) \tag{3.1}$$

$$\delta_{com\_2} = \frac{1}{2\sqrt{\eta_C^2 d_x^2 + d_z^2}} \left\{ \begin{array}{l} 2d_z \Delta_{x1} + 2\eta_C d_x \Delta_{z2} - \left(2\eta_C - 2\eta_C^2\right) d_x^2 \varphi_0 \\ -\left[d_z^2 - \left(2\eta_C - 2\eta_C^2\right) d_x^2 \right]\varphi_{x1} - \left(2\eta_C - \eta_C^2\right) d_x^2 \varphi_{z2} \end{array} \right\} \tag{3.2}$$

$$\delta_{com\_3} = \frac{d_x d_z}{\sqrt{\eta_C^2 d_x^2 + d_z^2}} \left(\frac{\eta_C \Delta_{x2}}{d_z} + \frac{\Delta_{z2}}{d_x} + \frac{\eta_C \varphi_{x2}}{2} - \left(1 - \frac{\eta_C}{2}\right)\varphi_{z2} + \eta_C \varphi_0 \right) \tag{3.3}$$

$$\delta_{com\_4} = \frac{2d_z \Delta_{x2} + 2d_x \eta_C \Delta_{z1} + d_z^2 \varphi_{x2} + \eta_C d_x^2 \varphi_{z1}}{2\sqrt{\eta_C^2 d_x^2 + d_z^2}} \tag{3.4}$$

$$\delta_{ten\_5} = \frac{1}{2\sqrt{\eta_C^2 d_x^2 + d_z^2}} \left\{ \begin{array}{l} 2d_z \Delta_{x1} + 2\eta_C d_x \Delta_{z2} + \left(2\eta_C - \eta_C^2\right) d_x^2 \varphi_{x1} \\ +\left[\left(\eta_C - \eta_C^2\right) d_x^2 + d_z^2\right]\varphi_{z2} - \left[\left(2\eta_C - \eta_C^2\right) d_x^2 + d_z^2\right]\varphi_0 \end{array} \right\} \tag{3.5}$$

$$\delta_{ten\_6} = \frac{d_x d_z}{\sqrt{\eta_C^2 d_x^2 + d_z^2}} \left(\frac{\Delta_{x1}}{d_z}\eta_C + \frac{\Delta_{z1}}{d_x} + \left(\frac{3\eta_C}{2} - 1\right)\varphi_{x1} - \left(\eta_C - \frac{1}{2}\right)\varphi_{z1} + \left(1 - \eta_C\right)\varphi_0 \right) \tag{3.6}$$

$$\delta_{ten\_7} = \frac{2d_z \Delta_{x2} + 2\eta_C d_x \Delta_{z1} - \eta_C^2 d_x^2 \varphi_{x2} - \left[d_z^2 - \left(\eta_C - \eta_C^2\right) d_x^2 \right]\varphi_{z1} - (\eta_C^2 d_x^2 + d_z^2)\varphi_0}{2\sqrt{\eta_C^2 d_x^2 + d_z^2}} \tag{3.7}$$

$$\delta_{ten\_8} = \frac{d_x d_z}{\sqrt{\eta_C^2 d_x^2 + d_z^2}} \left(\frac{\Delta_{x2}}{d_z}\eta_C + \frac{\Delta_{z2}}{d_x} - \frac{\varphi_{x2}\eta_C}{2} + \frac{\varphi_{z2}}{2} \right) \tag{3.8}$$

The displacement in the same direction of points on the diagonals distributed linearly as shown in Figure 3.5(c). The concrete tensile zones and compressive zones were separated by the zero displacement points. It was assumed that the strain distribution on the diagonals was also linear in which the zero strain points coincided with the corresponding zero displacement points. Eight concrete struts (C_1 to C_8) were used to define the four compressive zones and the four tensile zone in concrete so that the strain distribution on the section of struts was the same with the

foregoing strain distribution on the diagonals, as shown in Figure 3.5(d). At a loading stage, there were four concrete struts in compression and four concrete struts which did not carry any force in the tensile zone. Based on the flows of the compressive force along the diagonal in Figure 3.5(a), the diagonal length (d_{dia}) was assigned to the length of the concrete struts (C_1, C_3) parallel and next to this diagonal as shown in Figure 3.5(d). To keep the linear strain distribution on the diagonals and the coincidence of the zero displacement point and the corresponding zero strain point, the length of strut C_1 and C_3 was also assigned to that of C_6 and C_8. As a result, the concrete struts (C_1, C_3, C_6, C_8) in the diagonal direction had the same length (l_1). Similarly, the concrete struts (C_2, C_4, C_5, C_7) in the direction perpendicular to the diagonal also had the same length (l_2), as shown in Figure 3.5(d).

On the half-length of the diagonal, the typical distribution of the concrete strain is shown in Figure 3.5(e) with compressive strut i and tensile strut j. The strain at the end of the strut section regarding strut i (ε_{com_i}) and strut j (ε_{ten_j}) were determined as follows:

$$\varepsilon_{com\_i} = \frac{\delta_{com\_i}}{l_i} \tag{3.9}$$

$$\varepsilon_{ten\_j} = \frac{\delta_{ten\_j}}{l_i} \tag{3.10}$$

where $l_i = l_c$ or $l_i = l_t$ depends on the direction of the strut.

The width of strut i (w_{Ci}) and strut j (w_{Cj}) were governed by coefficient ξ_i and ξ_j, which were determined as follows:

$$\xi_i = \frac{\left|\varepsilon_{com\_i}\right|}{\left|\varepsilon_{com\_i}\right| + \left|\varepsilon_{ten\_j}\right|} \tag{3.11}$$

$$\xi_j = 1 - \xi_i \tag{3.12}$$

The joint thickness was assigned for the thickness of a strut, which was computed from the recommendation of AIJ [47]:

$$t = t_b + t_{c1} + t_{c2} \tag{3.13}$$

where t_b is beam width, t_{c1} and t_{c2} refer the smaller of ¼ column depth and ½ the distance between beam and column face on either side of the beam.

The average stress in the compressive strut i and the tensile strut j was calculated as follows:

$$\sigma_{Ci} = \frac{\int_0^{\varepsilon_{com\_i}} \sigma_{(\varepsilon)} d\varepsilon}{\varepsilon_{com\_i}} \tag{3.14}$$

$$\sigma_{Cj} = \frac{\int_0^{\varepsilon_{ten\_j}} \sigma_{(\varepsilon)} d\varepsilon}{\varepsilon_{\varepsilon_{ten\_j}}} \tag{3.15}$$

where $\sigma_{(\varepsilon)}$ is the function regarding the envelope of stress against strain.

The distance between the location of the strut axial force and the end of the strut section was computed by the coefficient β_1 to β_8 in Figure 3.5(f), which were determined as follows:

$$\beta_i = \xi_i \left(1 - \frac{\int_0^{\varepsilon_{com\_i}} \varepsilon \sigma_{(\varepsilon)} d\varepsilon}{\varepsilon_{com\_i} \int_0^{\varepsilon_{com\_i}} \sigma_{(\varepsilon)} d\varepsilon} \right) \quad \text{with } i = 1 \text{ to } 8 \tag{3.16}$$

$$\beta_j = \xi_j \left(1 - \frac{\int_0^{\varepsilon_{ten\_j}} \varepsilon \sigma_{(\varepsilon)} d\varepsilon}{\varepsilon_{ten\_j} \int_0^{\varepsilon_{ten\_j}} \sigma_{(\varepsilon)} d\varepsilon} \right) \quad \text{with } j = 1 \text{ to } 8 \tag{3.17}$$

In Equation (3.14) to Equation (3.17) if ε_{com_i} or ε_{ten_j} reaches zero, σ_{Ci}, σ_{Cj}, β_i, and β_j are also considered to be zero. Figure 3.5(f) shows the illustration of the eight concrete struts connected to the rigid plates.
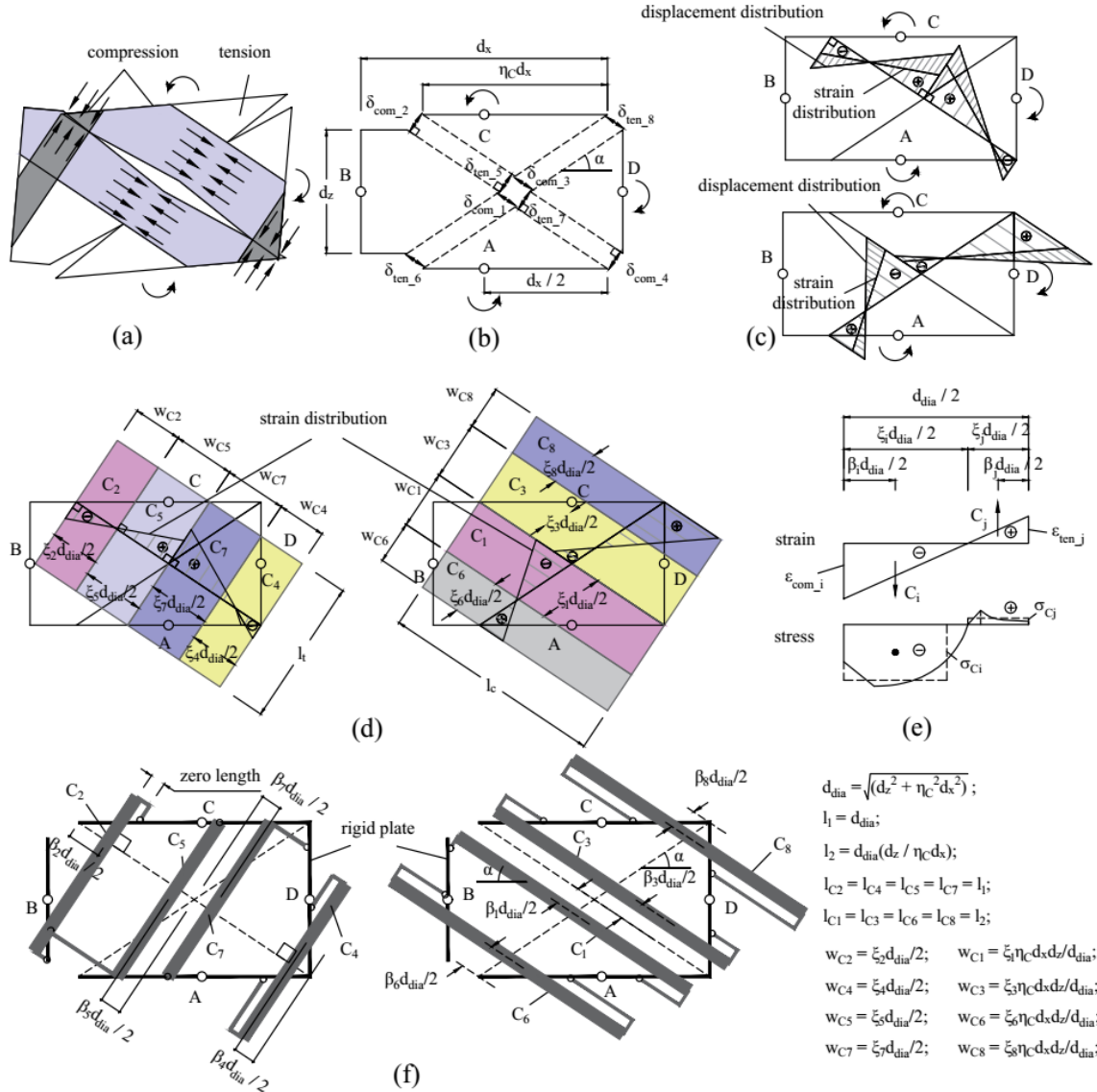
(a) Tensile zone and compressive zone in concrete; (b) Displacement of the center point and corner point; (c) Displacement and strain distribution on the joint diagonals; (d) Illustration of concrete strain distribution and the width of the struts; (e) Typical stress distribution on a half of the joint diagonals; (f) Definition of concrete struts connecting to rigid plates;

Figure 3.5. Definition of concrete struts of the exterior joint element

3.2.4 Bar springs

The rotation of the four rigid plates simulated the rotation of the four free bodies of the hinging model. When the rigid plates rotated, there were following displacements (Δ_{T2}, Δ_{T3}, Δ_{T5}, Δ_{T5T}, Δ_{T5B}, Δ_{T6}, Δ_{T7}, Δ_{T8}, Δ_{T9}, Δ_{T10}) at the location of the reinforcements, as shown in Figure 3.6.
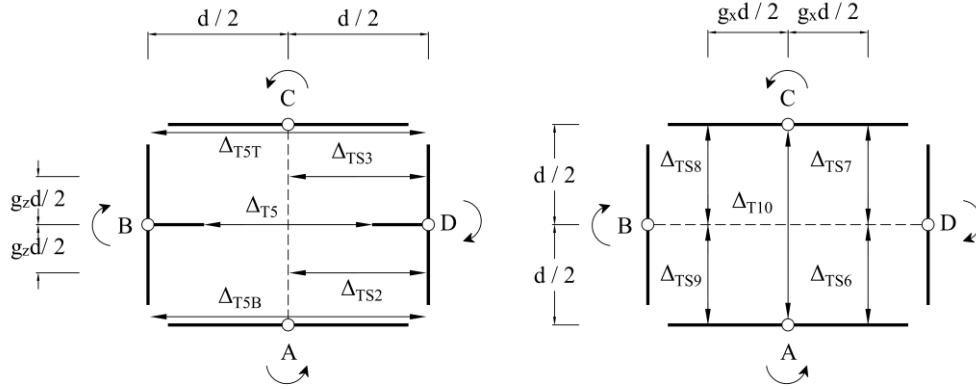
Figure 3.6. Deformation at the reinforcement location of the exterior joint element

These displacements could be computed by nine independent components of the joint deformations as follows:

$$\Delta_{TS2} = \Delta_{x2} + \frac{g_z d\varphi_{x2}}{2} - \frac{(1-g_z)d\varphi_{z1}}{2} - \frac{(1-g_z)d\varphi_0}{2} \tag{3.18}$$

$$\Delta_{TS3} = \Delta_{x2} - \frac{g_z d\varphi_{x2}}{2} - \frac{(1-g_z)d\varphi_{z2}}{2} + \frac{(1-g_z)d\varphi_0}{2} \tag{3.19}$$

$$\Delta_{T5} = \Delta_{x1} + \Delta_{x2} \tag{3.20}$$

$$\Delta_{T5T} = \Delta_{x1} + \Delta_{x2} - \frac{g_z d\varphi_{x1}}{2} - \frac{g_z d\varphi_{x2}}{2} \tag{3.21}$$

$$\Delta_{T5B} = \Delta_{x1} + \Delta_{x2} - \frac{g_z d\varphi_{x1}}{2} - \frac{g_z d\varphi_{x2}}{2} \tag{3.22}$$

$$\Delta_{TS6} = \Delta_{z1} + \frac{g_x d\varphi_{z1}}{2} - \frac{(1-g_x)d\varphi_{x2}}{2} - \frac{(1-g_x)d\varphi_0}{2} \tag{3.23}$$

$$\Delta_{TS7} = \Delta_{z2} + \frac{g_x d\varphi_{z2}}{2} + \frac{(1-g_x)d\varphi_{x2}}{2} + \frac{(1-g_x)d\varphi_0}{2} \tag{3.24}$$

92

$$\Delta_{TS8} = \Delta_{z2} - \frac{g_x d\varphi_{z2}}{2} + \frac{(1-g_x)d\varphi_{x1}}{2} - \frac{(1-g_x)d\varphi_0}{2} \tag{3.25}$$

$$\Delta_{TS9} = \Delta_{z1} - \frac{g_x d\varphi_{z1}}{2} - \frac{(1-g_x)d\varphi_{x1}}{2} + \frac{(1-g_x)d\varphi_0}{2} \tag{3.26}$$

$$\Delta_{T10} = \Delta_{z1} + \Delta_{z2} \tag{3.27}$$

In this section, bar springs were defined based on these displacements to represent reinforcements in joint core. Notation T_1 to T_4, T_6 to T_{10} were employed for the longitudinal beam bars and column bars respectively. T_5 represented the center joint hoops while T_{5T} and T_{5B} indicated the joint hoops at the contacting face of the joint and the columns, as shown in Figure 3.7. When slip was considered, the displacements in Figure 3.6 were used to define the deformation of bar springs and bond slip springs as illustrated in Figure 3.8. The axial forces of bar springs and bond-slip springs were shown in Figure 3.9.

The relationship between the force and the deformation of springs are expressed as follows:

$$\mathbf{T} = \mathbf{k_{TS}} \mathbf{\Delta_{TS}} \tag{3.28}$$

where:

$\mathbf{T}$ is the force vector of the bar springs, as follows:

$$\mathbf{T} = \left\{ T_2, T_3, T_5, T_{5T}, T_{5B}, T_6, T_7, T_8, T_9, T_{10} \right\} \tag{3.29}$$

$\mathbf{\Delta_{TS}}$ is the combined deformation vector of the springs:

$$\Delta_{TS} = \left\{ \Delta_{TS_2}, \Delta_{TS_3}, \Delta_{T_5}, \Delta_{T_{5T}}, \Delta_{T_{5B}}, \Delta_{TS_6}, \Delta_{TS_7}, \Delta_{TS_8}, \Delta_{TS_9}, \Delta_{T_{10}} \right\} \tag{3.30}$$

$\mathbf{k_{TS}}$ is the matrix of the combined tangent stiffness of all springs:

$$\mathbf{k_{TS}} = \begin{bmatrix} k_{T_{2-2}} & 0 & 0 & 0 & 0 & 0 & 0 & 0 & 0 & 0 \\ 0 & k_{T_{3-3}} & 0 & 0 & 0 & 0 & 0 & 0 & 0 & 0 \\ 0 & 0 & k_{T_5} & 0 & 0 & 0 & 0 & 0 & 0 & 0 \\ 0 & 0 & 0 & k_{T_{5A}} & 0 & 0 & 0 & 0 & 0 & 0 \\ 0 & 0 & 0 & 0 & k_{T_{5B}} & 0 & 0 & 0 & 0 & 0 \\ 0 & 0 & 0 & 0 & 0 & k_{T_{6-6}} & k_{T_{6-7}} & 0 & 0 & 0 \\ 0 & 0 & 0 & 0 & 0 & k_{T_{7-6}} & k_{T_{7-7}} & 0 & 0 & 0 \\ 0 & 0 & 0 & 0 & 0 & 0 & 0 & k_{T_{8-8}} & k_{T_{8-9}} & 0 \\ 0 & 0 & 0 & 0 & 0 & 0 & 0 & k_{T_{9-8}} & k_{T_{9-9}} & 0 \\ 0 & 0 & 0 & 0 & 0 & 0 & 0 & 0 & 0 & k_{T_{10}} \end{bmatrix} \quad (3.31)$$

with $\quad k_{T_{i-i}} = \dfrac{k_{T_i}(k_{T_j} + k_{S_r})}{k_{T_i} + k_{T_j} + k_{S_r}}$ \hfill (3.32)

and $\quad k_{T_{i-j}} = \dfrac{k_{T_i} k_{T_j}}{k_{T_i} + k_{T_j} + k_{S_r}}$ \hfill (3.33)

(i, j,r) = (1, 2, A), (3, 4, C), (6, 7, D), (8, 9, B)

In the above equations, T_1 and T_4 were not included. Because Δ_{T1} and Δ_{T4} had a relationship with the deformation of the adjacent bond-slip springs as shown in Figure 3.8, T_1 and T_4 were simultaneously determined with the bond forces by an iterative computational technique, which is mentioned later in the joint computational procedure.
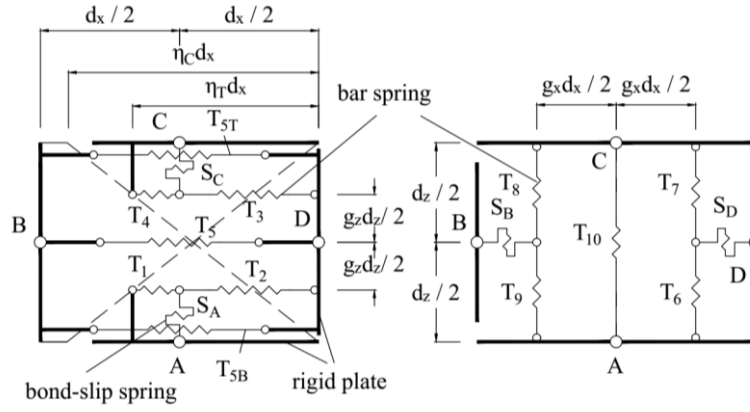
Length of bar springs and bond-slip springs:

$l_{SA} = \eta_T\, d_x;$ $l_{SB} = d_z;$ $l_{SC} = \eta_T\, d_x;$ $l_{SD} = d_z;$

$l_{T1} = (\eta_T - 1/2)\, d_x;$ $l_{T2} = d_x / 2;$ $l_{T3} = d_x / 2;$ $l_{T4} = (\eta_T - 1/2)\, d_x;$

$l_{T5} = g_x d_x;$ $l_{T6} = d_z / 2;$ $l_{T7} = d_z / 2;$ $l_{T8} = d_z / 2;$

$l_{T9} = d_z / 2;$ $l_{T10} = d_z;$ $l_{T5T} = g_x d_x;$ $l_{T5B} = g_x d_x;$

Figure 3.7. Definition of bar springs and bond-slip springs of the exterior joint element
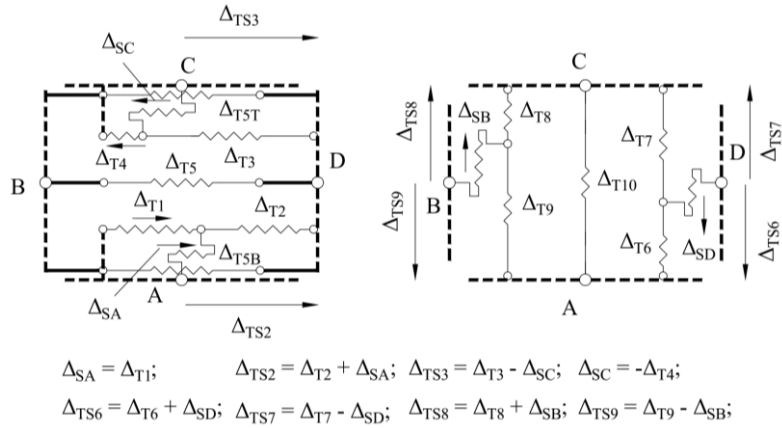
$\Delta_{SA} = \Delta_{T1};$ $\Delta_{TS2} = \Delta_{T2} + \Delta_{SA};$ $\Delta_{TS3} = \Delta_{T3} - \Delta_{SC};$ $\Delta_{SC} = -\Delta_{T4};$

$\Delta_{TS6} = \Delta_{T6} + \Delta_{SD};$ $\Delta_{TS7} = \Delta_{T7} - \Delta_{SD};$ $\Delta_{TS8} = \Delta_{T8} + \Delta_{SB};$ $\Delta_{TS9} = \Delta_{T9} - \Delta_{SB};$

Figure 3.8. Deformation of bar springs and bond-slip springs of the exterior joint element
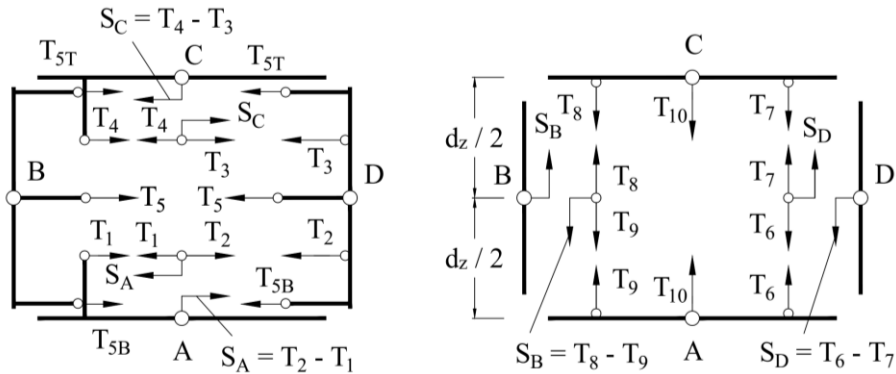
Figure 3.9. Axial forces of bar springs and bond-slip springs of the exterior joint element

3.2.5 Joint compatibility and stiffness

3.2.5.1 Before cracking

The joint elastic stiffness was used to analyze the joint response before cracking. The definition was similar to section 2.3.4.1.

3.2.5.2 After cracking

Equation (2.45) was also used to check the point when cracks occurred.

The joint deformation vector had a compatibility relationship with the vector including the average deformation of the struts (Δ_{C1} to Δ_{C8}) and the combined deformation of the springs as follows:

$$\mathbf{\Delta} = \mathbf{B_1}\mathbf{\delta} \tag{3.34}$$

where

$$\Delta = \left\{ \Delta_{C_1}, \Delta_{C_2}, .., \Delta_{C_7}, \Delta_{C_8}, \Delta_{TS_2}, \Delta_{TS_3}, \Delta_{T_5}, \Delta_{T_{5T}}, \Delta_{T_{5B}}, \Delta_{TS_6}, \Delta_{TS_7}, \Delta_{TS_8}, \Delta_{TS_9}, \Delta_{T_{10}} \right\} \tag{3.35}$$

Due to contragredience, there was the following relationship of the joint force vector $\mathbf{f}$ and the force vector of all springs and struts $\mathbf{q}$:

$$\mathbf{f} = \mathbf{B_1^T}\mathbf{q} \tag{3.36}$$

where

$$\mathbf{q} = \left\{ C_1, C_2, C_3, C_4, C_5, C_6, C_7, C_8, T_2, T_3, T_5, T_{5T}, T_{5B}, T_6, T_7, T_8, T_9, T_{10} \right\} \tag{3.37}$$

$$
\mathbf{B_1} = \begin{bmatrix}
\cos\alpha & 0 & \sin\alpha & 0 & \eta_{15} & 0 & \eta_{17} & 0 & \eta_{19} \\
\sin\alpha & 0 & 0 & \cos\alpha & \eta_{25} & 0 & 0 & \eta_{28} & \eta_{29} \\
0 & \cos\alpha & 0 & \sin\alpha & 0 & \eta_{36} & 0 & \eta_{38} & \eta_{39} \\
0 & \sin\alpha & \cos\alpha & 0 & 0 & \eta_{46} & \eta_{47} & 0 & \eta_{49} \\
\sin\alpha & 0 & 0 & \cos\alpha & \eta_{55} & 0 & 0 & \eta_{58} & \eta_{59} \\
\cos\alpha & 0 & \sin\alpha & 0 & \eta_{65} & 0 & \eta_{67} & 0 & \eta_{69} \\
0 & \sin\alpha & \cos\alpha & 0 & 0 & \eta_{76} & \eta_{77} & 0 & \eta_{79} \\
0 & \cos\alpha & 0 & \sin\alpha & 0 & \eta_{86} & 0 & \eta_{88} & \eta_{89} \\
0 & 1 & 0 & 0 & 0 & \dfrac{g_z d_z}{2} & -\dfrac{(1-g_z)d_z}{2} & 0 & -\dfrac{(1-g_z)d_z}{2} \\
0 & 1 & 0 & 0 & 0 & -\dfrac{g_z d_z}{2} & 0 & -\dfrac{(1-g_z)d_z}{2} & \dfrac{(1-g_z)d_z}{2} \\
1 & 1 & 0 & 0 & 0 & 0 & 0 & 0 & 0 \\
1 & 1 & 0 & 0 & -\dfrac{d_z}{2} & -\dfrac{d_z}{2} & 0 & 0 & 0 \\
1 & 1 & 0 & 0 & \dfrac{d_z}{2} & \dfrac{d_z}{2} & 0 & 0 & 0 \\
0 & 0 & 1 & 0 & 0 & -\dfrac{(1-g_x)d_x}{2} & \dfrac{g_x d_x}{2} & 0 & -\dfrac{(1-g_x)d_x}{2} \\
0 & 0 & 0 & 1 & 0 & \dfrac{(1-g_x)d_x}{2} & 0 & \dfrac{g_x d_x}{2} & \dfrac{(1-g_x)d_x}{2} \\
0 & 0 & 0 & 1 & \dfrac{(1-g_x)d_x}{2} & 0 & 0 & -\dfrac{g_x d_x}{2} & -\dfrac{(1-g_x)d_x}{2} \\
0 & 0 & 1 & 0 & -\dfrac{(1-g_x)d_x}{2} & 0 & -\dfrac{g_x d_x}{2} & 0 & \dfrac{(1-g_x)d_x}{2} \\
0 & 0 & 1 & 1 & 0 & 0 & 0 & 0 & 0
\end{bmatrix}
\tag{3.38}
$$

where α is the are the angle with respect to the orientation of the joint diagonals and the horizontal direction:

$$
\alpha = \arctan\left(\frac{d_z}{\eta_C d_x}\right)
\tag{3.39}
$$

and:

$$
\eta_{15} = \frac{\beta_1 \mathrm{d}_z}{2}\cos\alpha - \left(2 - \eta_C - \eta_C\beta_1\right)\frac{\mathrm{d}_x}{2}\sin\alpha
\tag{3.40}
$$

$$
\eta_{17} = \left(1 - \beta_1\right)\frac{\mathrm{d}_z}{2}\cos\alpha - \left(\eta_C - 1 + \eta_C\beta_1\right)\frac{\mathrm{d}_x}{2}\sin\alpha
\tag{3.41}
$$

$$\eta_{19} = \left(1-\beta_1\right)\frac{\mathrm{d}_{dia}}{2}\sin 2\alpha + \left(1-\eta_C\right)d_x\sin\alpha \tag{3.42}$$

$$\eta_{25} = -\left(1-\beta_2\right)\frac{\mathrm{d}_z}{2}\sin\alpha + \left(1-\eta_C+\eta_C\beta_2\right)\frac{\mathrm{d}_x}{2}\cos\alpha \tag{3.43}$$

$$\eta_{28} = \frac{\beta_2\,\mathrm{d}_z}{2}\sin\alpha - \left(2\eta_C-1-\eta_C\beta_2\right)\frac{\mathrm{d}_x}{2}\cos\alpha \tag{3.44}$$

$$\eta_{29} = -\beta_2\frac{\mathrm{d}_{dia}}{2} + \left(1-\eta_C\right)d_x\cos\alpha \tag{3.45}$$

$$\eta_{36} = -\frac{\beta_3\,\mathrm{d}_z}{2}\cos\alpha + \left(1-\beta_3\right)\eta_C\frac{\mathrm{d}_x}{2}\sin\alpha \tag{3.46}$$

$$\eta_{38} = -\left(1-\beta_3\right)\frac{\mathrm{d}_z}{2}\cos\alpha + \left(1-\eta_C+\eta_C\beta_3\right)\frac{\mathrm{d}_x}{2}\sin\alpha \tag{3.47}$$

$$\eta_{39} = \left(1-\beta_3\right)\frac{\mathrm{d}_{dia}}{2}\sin 2\alpha \tag{3.48}$$

$$\eta_{46} = \left(1-\beta_4\right)\frac{\mathrm{d}_z}{2}\sin\alpha - \eta_C\beta_4\frac{\mathrm{d}_x}{2}\cos\alpha \tag{3.49}$$

$$\eta_{47} = -\frac{\beta_4\,\mathrm{d}_z}{2}\sin\alpha + \left(1-\eta_C\beta_4\right)\frac{\mathrm{d}_x}{2}\cos\alpha \tag{3.50}$$

$$\eta_{49} = -\beta_4\frac{\mathrm{d}_{dia}}{2} \tag{3.51}$$

$$\eta_{55} = -\frac{\beta_5\,\mathrm{d}_z}{2}\sin\alpha + \left(2-\eta_C-\eta_C\beta_5\right)\frac{\mathrm{d}_x}{2}\cos\alpha \tag{3.52}$$

$$\eta_{58} = \left(1-\beta_5\right)\frac{\mathrm{d}_z}{2}\sin\alpha - \left(\eta_C-1+\eta_C\beta_5\right)\frac{\mathrm{d}_x}{2}\cos\alpha \tag{3.53}$$

$$\eta_{59} = -\left(1-\beta_5\right)\frac{\mathrm{d}_{dia}}{2} + \left(1-\eta_C\right)d_x\cos\alpha \tag{3.54}$$

$$\eta_{65} = \left(1-\beta_6\right)\frac{\mathrm{d}_z}{2}\cos\alpha - \left(2-2\eta_C+\eta_C\beta_6\right)\frac{\mathrm{d}_x}{2}\sin\alpha \tag{3.55}$$

$$\eta_{67} = \frac{\beta_6 \, \mathrm{d}_z}{2} \cos \alpha - \left(2\eta_C - 1 - \eta_C \beta_6\right) \frac{\mathrm{d}_x}{2} \sin \alpha \tag{3.56}$$

$$\eta_{69} = \beta_6 \frac{\mathrm{d}_{dia}}{2} \sin 2\alpha + \left(1 - \eta_C\right) d_x \sin \alpha \tag{3.57}$$

$$\eta_{76} = \frac{\beta_7 \, \mathrm{d}_z}{2} \sin \alpha - \eta_C \left(1 - \beta_7\right) \frac{\mathrm{d}_x}{2} \cos \alpha \tag{3.58}$$

$$\eta_{77} = -\left(1 - \beta_7\right) \frac{\mathrm{d}_z}{2} \sin \alpha + \left(1 - \eta_C + \eta_C \beta_7\right) \frac{\mathrm{d}_x}{2} \cos \alpha \tag{3.59}$$

$$\eta_{79} = -\left(1 - \beta_7\right) \frac{\mathrm{d}_{dia}}{2} \tag{3.60}$$

$$\eta_{86} = -\left(1 - \beta_8\right) \frac{\mathrm{d}_z}{2} \cos \alpha + \eta_C \beta_8 \frac{\mathrm{d}_x}{2} \sin \alpha \tag{3.61}$$

$$\eta_{88} = -\frac{\beta_8 \, \mathrm{d}_z}{2} \cos \alpha + \left(1 - \eta_C \beta_8\right) \frac{\mathrm{d}_x}{2} \sin \alpha \tag{3.62}$$

$$\eta_{89} = \beta_8 \frac{\mathrm{d}_{dia}}{2} \sin 2\alpha \tag{3.63}$$

The stiffness matrix $\mathbf{k_0}$ in Equation (2.10) could be computed as follows:

$$\mathbf{k}_0 = \mathbf{B}_1^t \, \mathbf{k}_1 \, \mathbf{B}_1 \tag{3.64}$$

where $\mathbf{k_1}$ is the stiffness matrix which includes the stiffness of all concrete struts and bar springs:

$$\mathbf{k}_1 = \begin{bmatrix} \mathbf{k}_C & 0 \\ 0 & \mathbf{k}_{TS} \end{bmatrix} \tag{3.65}$$

$\mathbf{k_{TS}}$ is derived from Equation (3.31); $\mathbf{k_C}$ is the diagonal stiffness matrix of all concrete struts including:

$$k_{Ci} = \frac{C_i^n - C_i^{n-1}}{\Delta_{Ci}^n - \Delta_{Ci}^{n-1}} \quad (i = 1 \div 8) \tag{3.66}$$

where $\Delta_{Ci}{}^n$, $C_i{}^n$, $\Delta_{Ci}{}^{n-1}$, and $C_i{}^{n-1}$ are the average deformations and axial forces of strut C_i and strut C_j at step n and step $n-1$ respectively. $\Delta_i{}^n$ and $\Delta_i{}^{n-1}$ were defined as follows:

$$\Delta_{Ci}^n = \frac{\xi_i - \beta_i}{\xi_i} \delta_{com\_i} \tag{3.67}$$

$$\Delta_{Cj}^n = \frac{\xi_j - \beta_j}{\xi_j} \delta_{ten\_j} \tag{3.68}$$

At the beginning of loading, coefficient ξ_i *(i = 1÷8)* was assigned to be 0.5.

The strut initial stiffness was determined as follows:

$$k_{Ci} = \frac{E_c A_{ci}}{l_c} \quad (i = 1÷8) \tag{3.69}$$

where E_c is the concrete modulus.

The joint stiffness in Equation (2.10) was rewritten as follows:

$$\mathbf{K} = \mathbf{B_0^t} \mathbf{B_1^t} \mathbf{k_1} \mathbf{B_1} \mathbf{B_0} \tag{3.70}$$

The constitutive model of materials is the same with the definition in section 2.6.2.

3.2.6 Verification of experimental result

3.2.6.1 Specimens

Four specimens (L06, N02, O02, and P02) from a series of tests on exterior joint subassemblages [48] were chosen for verification. Details of specimens are described in Table 3.1. Specimen L06 has a common section of 240 x 240 mm for beam and column using steel plate welded at ends of beam bars as anchorages. Specimen O02 has the same size like L06 but anchorages type U are employed. N02 and P02 also uses the same type of anchorage of L06 but different size of frame members with beam section of 240 x 170 mm and column section of 240 x 340 mm for N02, and beam section of 240 x 340 mm and column section of 240 x 170 mm for P02. Bars D6 are utilized for hoops of all specimens with two sets for L06, N02, O02 and three sets for P02. Beams and columns of specimens are 700 mm length from one end to the joint center, and detailed geometric properties are shown in Figure 3.10, Figure 3.11, Figure 3.12. Load setup and loading history are described in Figure 3.13 and Figure 3.14. Force

applies at the top of columns so that the absolute magnitude of axial force in columns is equal to half of shear forces in beam V_b.

Table 3.1. Properties of exterior joint specimens

Specimen	L06	N02	O02	P02
concrete compressive strength (MPa)	27.7	29.0	29.8	26.2
beam width x depth (mm)	240 x 240	240 x 170	240 x 240	240 x 340
longitudinal beam bars	4-D13	6-D13	4-D13	3-D13
bar yielding strength (Mpa)		380		
bar distant ratio	0.8	0.72	0.8	0.86
column width x depth (mm)	240 x 240	240 x 340	240 x 240	240 x 170
longitudinal column bars	4-D13	2-D13	2-D13	5-D13
column bar yielding strength (Mpa)		380		
column bar distant ratio	0.8	0.86	0.8	0.72
anchorage length (mm)	156	221	156	111
anchorage length		0.65		
joint hoops		D6 (2 sets)		D6 (3 sets)
hoops yielding strength (Mpa)		334		
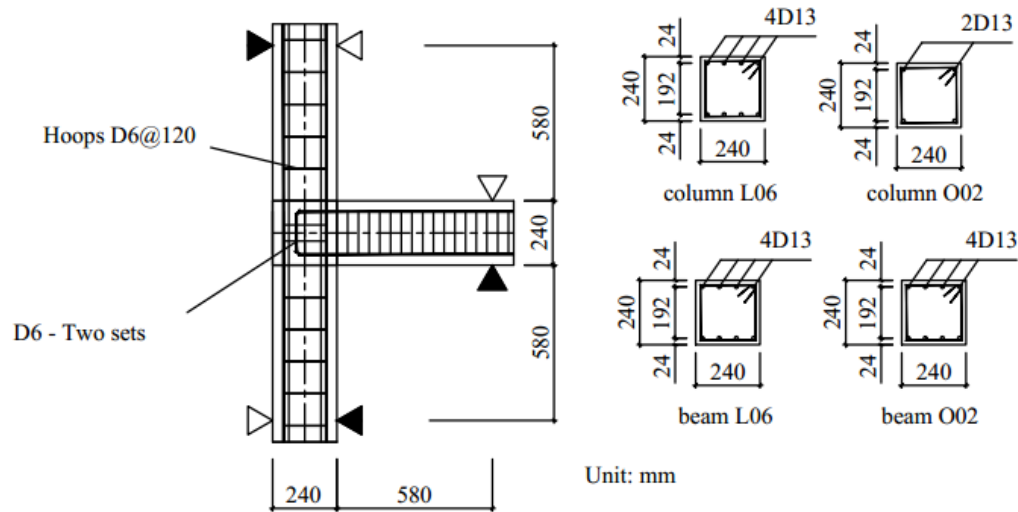
Figure 3.10. Test specimens: L06, O02
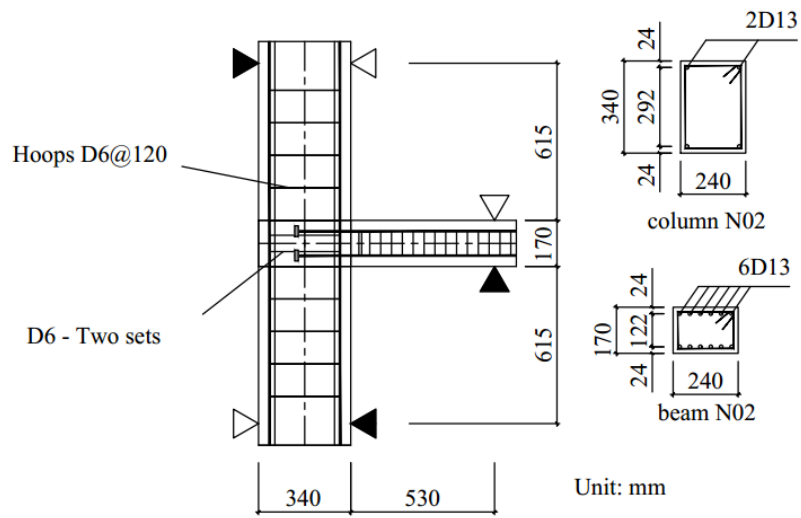
Figure 3.11. Test specimens: N02

102
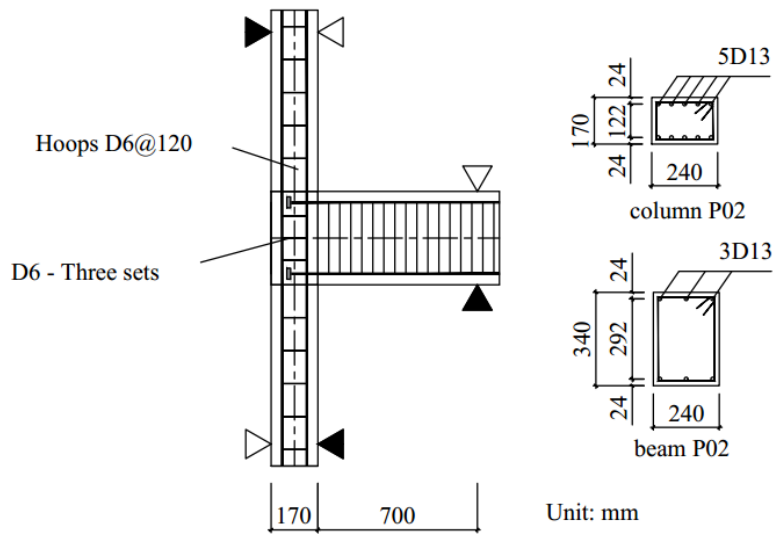
Figure 3.12. Test specimens: P02
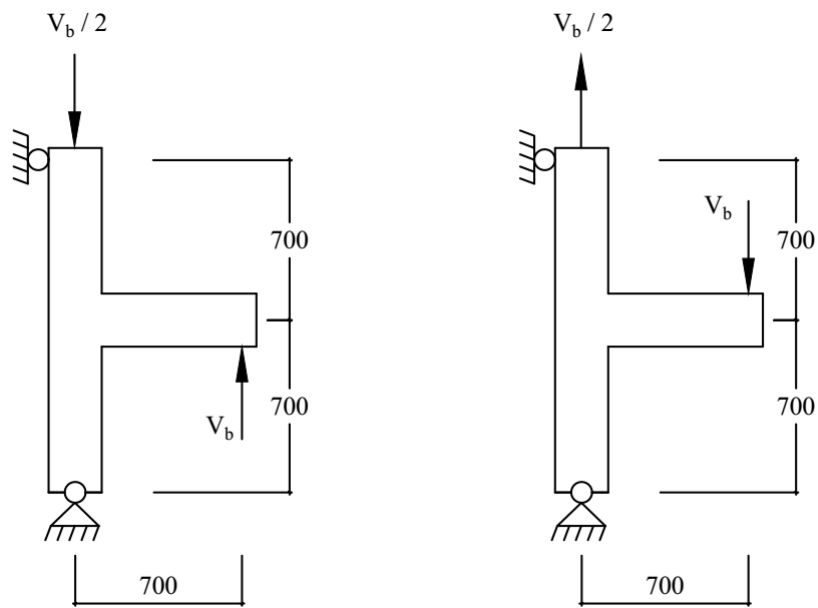
Figure 3.13. Load setup of exterior joint experiment
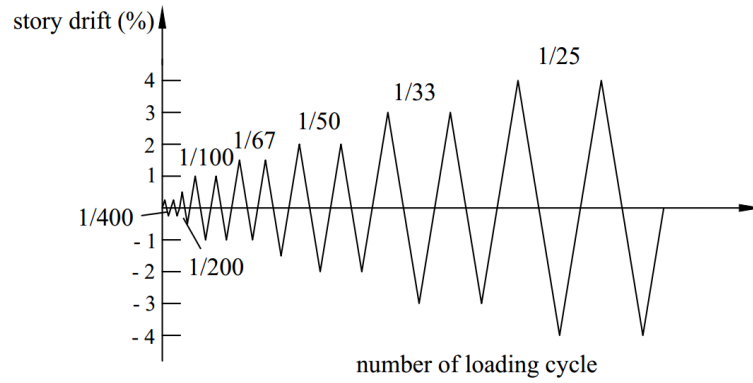
Figure 3.14. Load history of exterior joint specimens

3.2.6.2 *Computational procedure*

The computational procedure before cracking was similar to Figure 2.21. The Newton-Raphson iterative algorithm in Figure 2.23 was also used. The detailed computational procedure of the joint is described in Figure 3.15 for stages after cracking in which a set of the joint nodal displacements (**d**) returned in a set of the joint nodal forces (**p**). Computation was carried out by OBASAN with Newton-Raphson iterative method. Response after degradation was not interested in order to avoid non-converging.

```
          ┌─────────────────────────────────┐
          │    Compute K in Eq.(2.58)       │
          └─────────────────────────────────┘
                          │
          ┌ ─ ─ ─ ─ ─ ─ ─ ─ ─ ─ ─ ─ ─ ─ ─ ─┐
          │  Assume the column axial force Fzi │
          └ ─ ─ ─ ─ ─ ─ ─ ─ ─ ─ ─ ─ ─ ─ ─ ─┘
                          │
          ┌─────────────────────────────────┐
          │  Compute δ = B₀e in Eq.(3.34)   │
          └─────────────────────────────────┘
```

Compute $\delta = B_0 e$ in Eq.(3.34)

Compute $\Delta = B_1 \delta$ in Eq.(3.34)

Get Δ_{TS}

Compute
δ_{com_i}, δ_{ten_j} in Eq.(3.1) to Eq.(3.8)
ε_{com_i}, ε_{ten_j} in Eq.(3.9) and Eq.(3.10)
ζ_{com_i}, ζ_{ten_j} in Eq.(3.11) and Eq. (3.12)
w_{ci}, w_{cj}, A_{ci}, A_{cj})
$(i = 1,2,3,4)$, $(j = 5,6,7,8)$

Assume Δ_{Sr}

$\Delta_{Ti} = \Delta_{TSi} + \Delta_{Sr}$
$\Delta_{Tj} = \Delta_{TSj} - \Delta_{Sr}$

Not in equilibrium

Constitutive slip model

Constitutive steel model

S_r

T_i, T_j

Check
$|S_r - (T_i - T_j)|$
$< |S_r|$*tolerance

Compute β_i, β_j
in Eq.(3.16) and Eq.(3.17)
and update B_1 in Eq. (3.38)

Compute
σ_{ci} $(i = 1,2,3,4)$, σ_{cj} $(j=5,6,7,8)$
in Eq.(3.14) and Eq.(3.15)

Compute
$C_i = A_{ci}\sigma_{ci}$; $C_j = A_{cj}\sigma_{cj}$

Compute **f** in Eq.(3.36)
and compute **p**

No

Check $| F_{zi} - 0.5V_b| < | F_{zi} |$*tolerance

Yes

Compute k_{Ci} and k_{TS} then compute K in Eq. (2.58) for
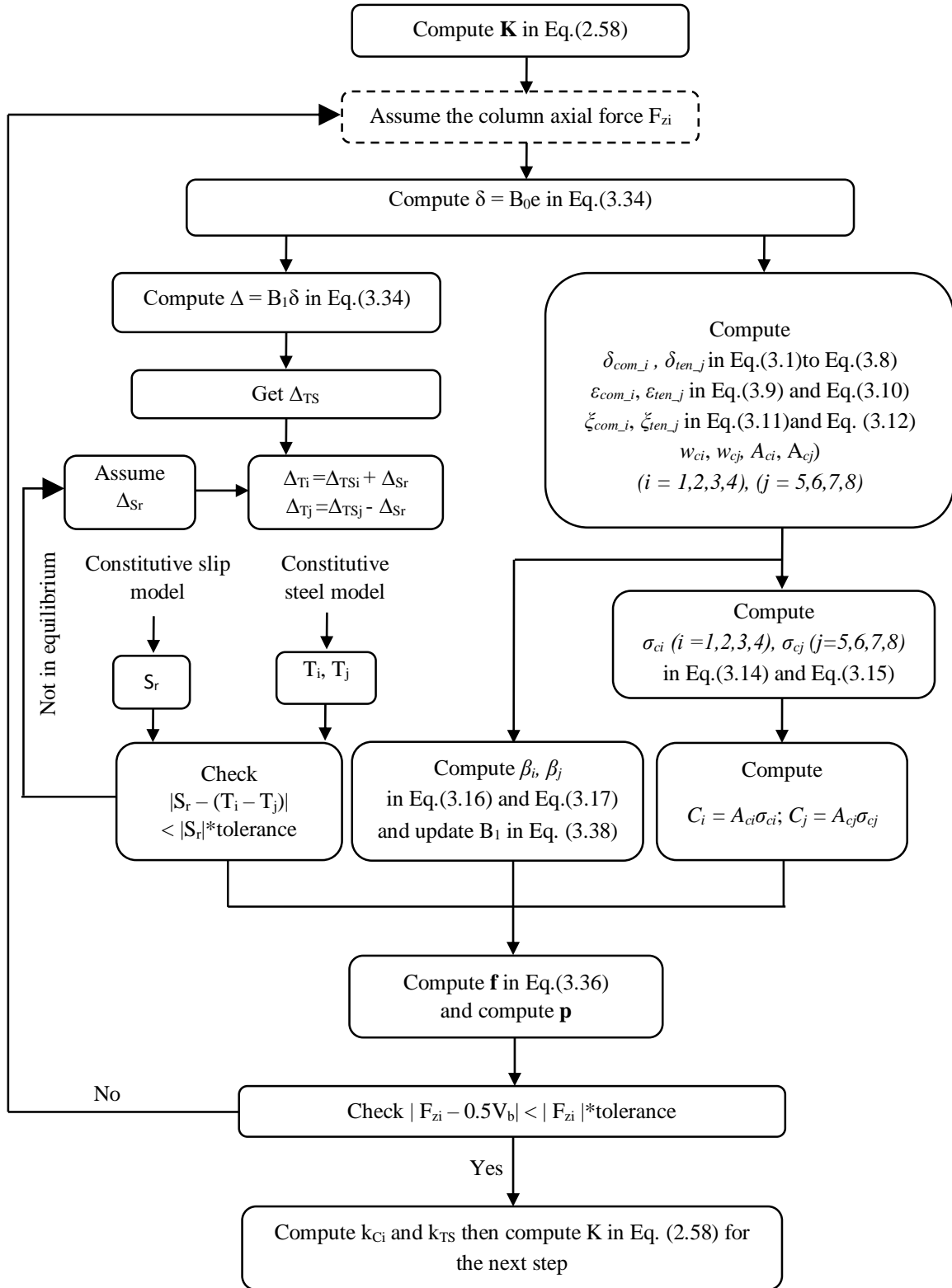the next step

Figure 3.15. Chart of the computational procedure after cracking for an exterior joint element

3.2.6.3 Load deflection relationship

Relationships of story shear versus story drift of the four specimens are described in Figure 3.16. Results showed good correlations between maximum story shear predicted by the new model with observation. The differences of maximum story shear between observation and computation based on the new joint model were 1.9%, 5.6%, 11.4%, and 2.4% in specimen L06, N02, O02, and P02 respectively. Degradation of story shear at 1.5% of L06, O02, and P02, and at 1% of N02 was predicted well although there was disagreement in O02 with the ultimate point at 2% of negative path instead of 1.5% by prediction.

3.2.6.4 Failure mode

The prediction of the joint failure mode was confirmed by observation in all specimens. To understand more specifically joint performance, failure modes of specimens are evaluated with considering failure of crushing concrete struts, yielding failure of reinforcements, and bond failure of reinforcing bars. The crushing of concrete struts was predicted when the computed concrete average stress degraded. The bond failure of reinforcement was captured when the bond stress exceeded $2.5f'_c$. The results of the joint failure modes were described in Table 3.2. Crushing of concrete was predicted only in specimen P02, but the maximum compressive forces in struts of other specimen almost attained limitation. Similar to analysis of interior joints, there was no estimated bond failure although in the most critical case in specimen N02, the bond stress attained 80% the bond strength.

In comparison to test data, the computation in specimen L06 and P02 had a good prediction of yielding in the center joint hoop although there was a difference in predicting yielding of the longitudinal bars in the beams and columns. There was also a good correlation between the analytical results and test data in specimen N02 and O02 in which the longitudinal bars in the beams did not yield while the center joint hoops and the longitudinal bars in columns yielded within the story drift of 1%.

Figure 3.16. Story shear versus story drift relationship of exterior joint specimens
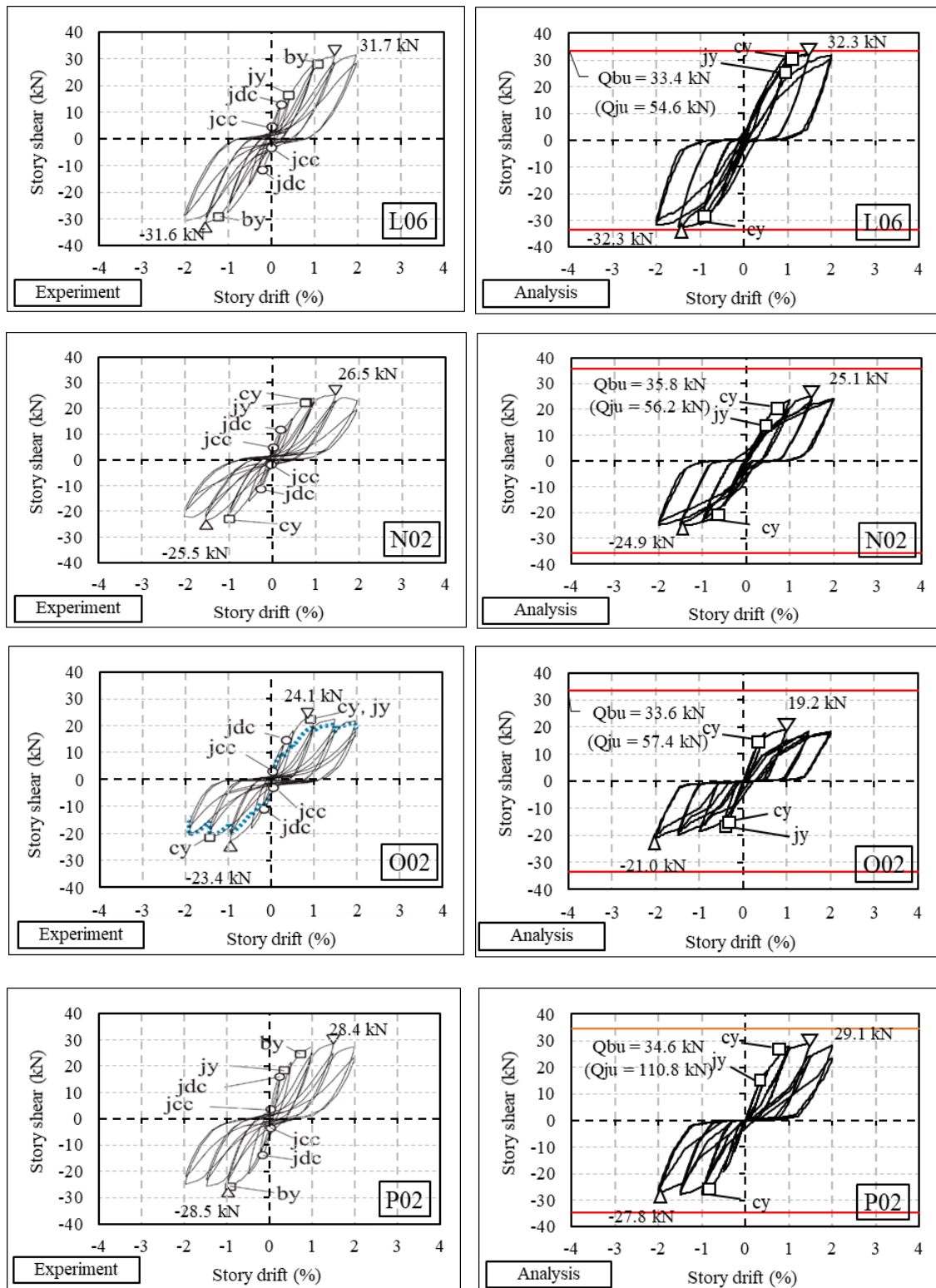
*** Notation

jcc	diagonal cracking at corner of joint	cy	yielding of longitudinal bar in column
jdc	diagonal cracking at center of joint	jy	yielding of joint hoop
by	yielding of longitudinal bar in beam	▽	maximum story shear

Table 3.2. Failure modes of exterior joint specimens

Specimen	Failure mode
L06	Yielding of bars of column Yielding of joint hoops
N02	Yielding of bars of column Yielding of joint hoops
O02	Yielding of bars of column Yielding of joint hoops
P02	Yielding of bars of column Yielding of joint hoops Concrete strut crushing

3.2.6.5 *Comparison to Shiohara's numerical method*

Shiohara [49] introduced a numerical method to compute the story shear and the resultant force in concrete and reinforcing bars at the ultimate stage based on some assumptions of stress in material. That numerical method was used in this section to compare with the material resultant forces by the analysis. The result is shown in Figure 3.17 and Table 3.3 in which all of the forces were normalized by $0.85tf'_c$. In all specimens, there was a good agreement of the story shear at the ultimate point in the two cases. The resultant force in the longitudinal bars in the beams and columns was almost the same. The computation showed that there was no compressive force in strut C2 which agreed well with the same assumption in Shiohara numerical method. The difference in the concrete resultant forces was attributed to the stress in the center joint hoops. At the failure point, the center joint hoops in Shiohara numerical method were assumed to yield. In the present analysis, the yielding of the center joint hoops occurred before the failure stage. Due to the plastic deformation, the stress of the center joint hoops at the failure point was smaller than the hoop yielding strength. In general, there was a good correlation between two cases in predicting the story shear and the forces in material at the ultimate stage.
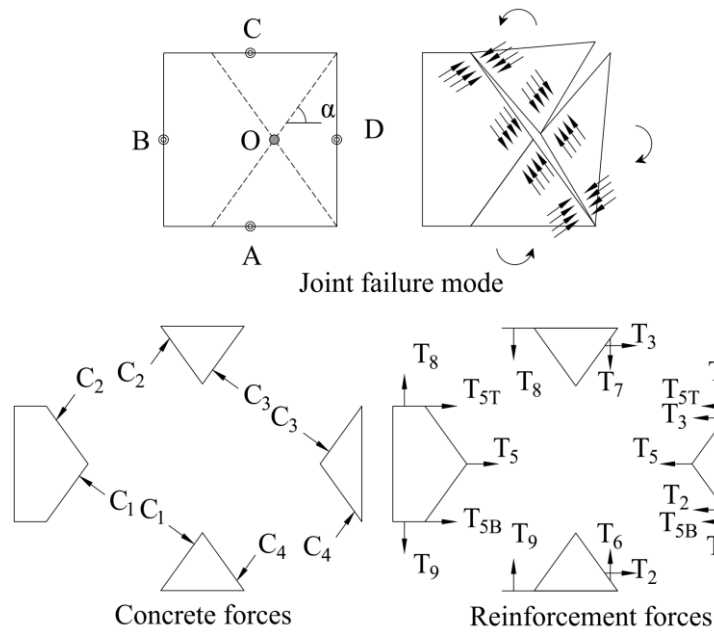
Figure 3.17. Joint failure mode and resultant forces in material of exterior joint specimens

Table 3.3. Predicted story shear and resultant forces in material of exterior joint specimens

Force	Specimen			
	L06	N02	O02	P02
C1	0.011 (0.013)	0.007 (0.009)	0.009 (0.012)	0.007 (0.009)
C2	0.000 (0.000)	0.000 (0.000)	0.000 (0.000)	0.000 (0.000)
C3	0.043 (0.047)	0.032 (0.051)	0.018 (0.015)	0.032 (0.028)
C4	0.025 (0.027)	0.023 (0.028)	0.020 (0.021)	0.023 (0.025)
T2	0.008 (0.008)	0.002 (0.002)	0.006 (0.006)	0.002 (0.002)
T3	0.031 (0.034)	0.031 (0.049)	0.014 (0.013)	0.031 (0.028)
T5	0.006 (0.007)	0.005 (0.007)	0.005 (0.007)	0.005 (0.007)
T5T	0.004 (0.004)	0.004 (0.004)	0.004 (0.004)	0.004 (0.004)
T5B	-0.004 (-0.004)	-0.004 (-0.004)	-0.004 (-0.004)	-0.004 (-0.004)
T6	0.004 (0.006)	0.012 (0.012)	0.008 (0.010)	0.012 (0.015)
T7	0.036 (0.034)	0.019 (0.019)	0.018 (0.018)	0.019 (0.019)
T8	0.004 (0.004)	0.002 (0.002)	-0.001 (-0.002)	0.024 (0.014)
T9	0.013 (0.014)	0.006 (0.006)	0.008 (0.008)	0.006 (0.006)
Story shear	0.006 (0.006)	0.006 (0.006)	0.004 (0.004)	0.005 (0.005)

*Number in parentheses was derived from Shiohara's numerical method

3.3 Application of the new joint model to investigate the cyclic response of knee joints

3.3.1 Knee joint model

In this section, knee beam-column joints with a full anchorage length ratio ($\eta_{Cx} = \eta_{Cz} \approx 1$) were modeled by the interior joint element in Chapter 2 to investigate the cyclic response.

3.3.2 Specimens

An experiment on response of RC knee joints under cyclic loadings of Mogili et al. [50] was employed for analysis. Specimen KJ1 and specimen KJ2 with the same length of 1800 mm and the same beam and column section of 300x300 mm, as shown in Figure 3.18, were chosen for analysis. The columns of two specimens had three bars T20 (diameter = 20 mm) at the top layer and the bottom layer symmetrically. While the beam of KJ1 had the same bar arrangement like columns, the beam of KJ2 had two bars T20 at the top layer. Stirrup T10 (diameter = 10 mm) was placed at the joint region with 3-closed stirrup for transverse and 3-U shaped stirrup for vertical direction respectively. Bar T20 and bar T10 had yield strength of 551.4 MPa and 500.6 MPa, modulus of elasticity 200 GPa and 204.8 GPa respectively. KJ1 used concrete with strength of 38.34 MPa while KJ2 used concrete with strength of 39.43 MPa. Test setup and loading history for specimens are denoted in Figure 3.18 and Figure 3.19. Load was applied to beam end and column end through a diagonal hydraulic actuator which could generate opening mode and closing mode for a joint.

3.3.3 Analytical results and discussion

The relationships of story shear versus story drift of the two specimens are shown in Figure 3.20 and the resultant forces in concrete and reinforcement at the ultimate stage are shown in Figure 3.21 in which all forces were normalized by *0.85tf'$_c$.*. There was significant difference between test data and the analysis. In both specimen KJ1 and KJ2, the beam yielding occurred although there was joint failure mode from observation. There was an absent of the top middle reinforcing bar in the beam section of KJ2 in comparison to that of KJ1 while the column reinforcing details of the two specimens were identical. These features induced the same opening response in both KJ1 and KJ2 and the dominant response in the closing mode of KJ1 which could not be predicted by the computation. As shown in Figure 3.21, the resultant forces in materials were symmetric respect to the diagonals in KJ1 in which the location resultant

110

forces returned in a little difference of story shear between the opening mode and closing mode. Similarly, although there was a redistribution of resultant forces due to the difference of section properties of beam and column in KJ2, the computed story shear in the two modes attained that at the yielding strength of beam and column and resulted in the story shear ratio of 1.0 between the two modes which overestimated the observed response. In KJ1, the difference of the maximum actuator force between test data and the analysis was 6.8% and 34.3% in KJ1 and KJ2 respectively. The ratio of the maximum force between the opening mode and the closing mode in KJ1 from experiment was 0.61 which was quite different from that ratio of 0.92 from computation. In KJ2, the ratio was 0.78 and 1.00 for observation and prediction respectively. The above disagreements were attributed to the difference of the failure mode used for building the joint model and the real failure mode in knee joint specimens. In Figure 3.22, observed dominant crack of knee joints opened fanwise which differed the diagonal crack pattern from those of interior joints in Figure 2.2 and those of exterior joints in Figure 3.2. To have a more reliable response, some further modifications of the size and the location of rigid bodies in knee joints are necessary.
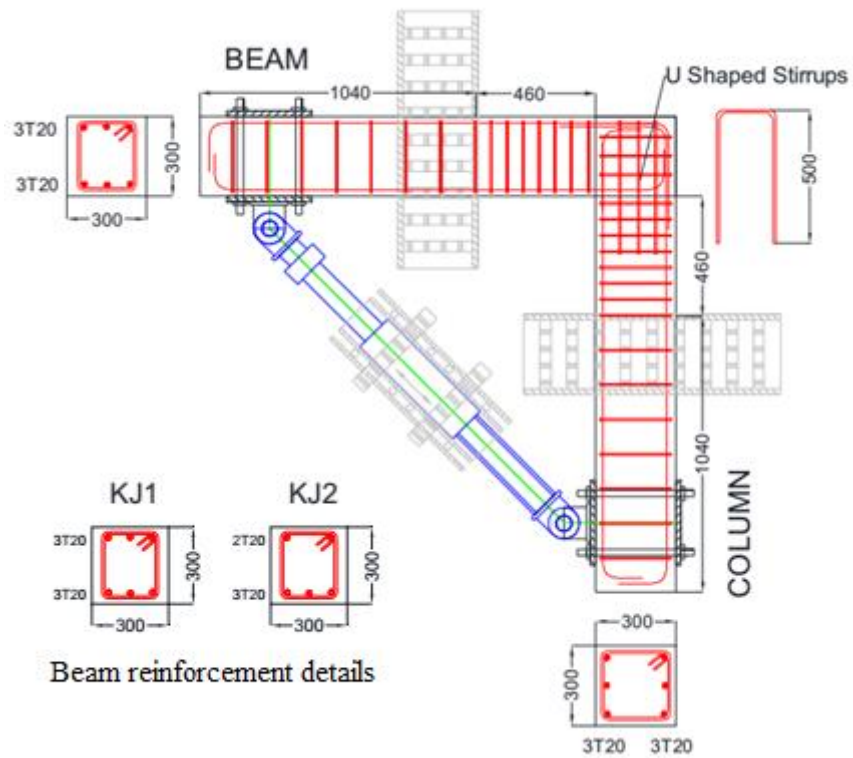
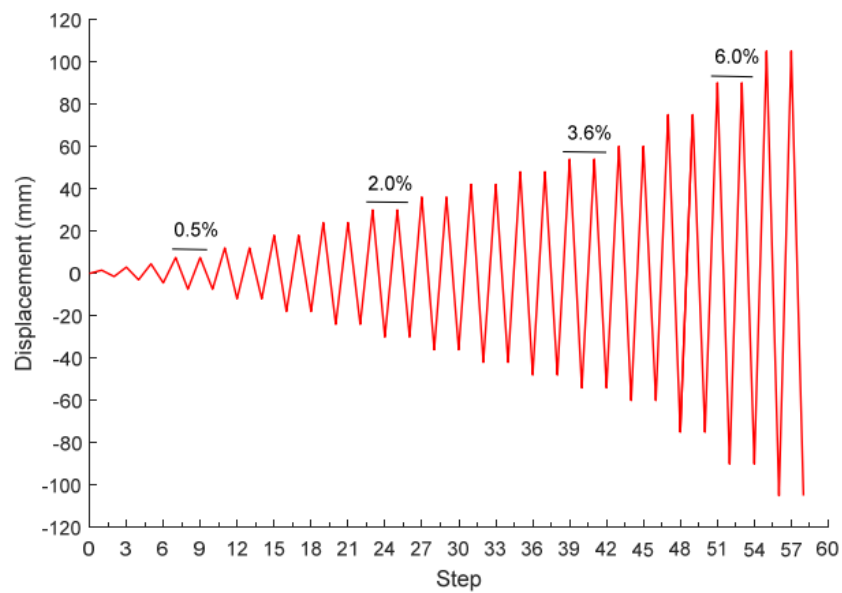Figure 3.18. Test setup of specimen KJ1 and KJ2

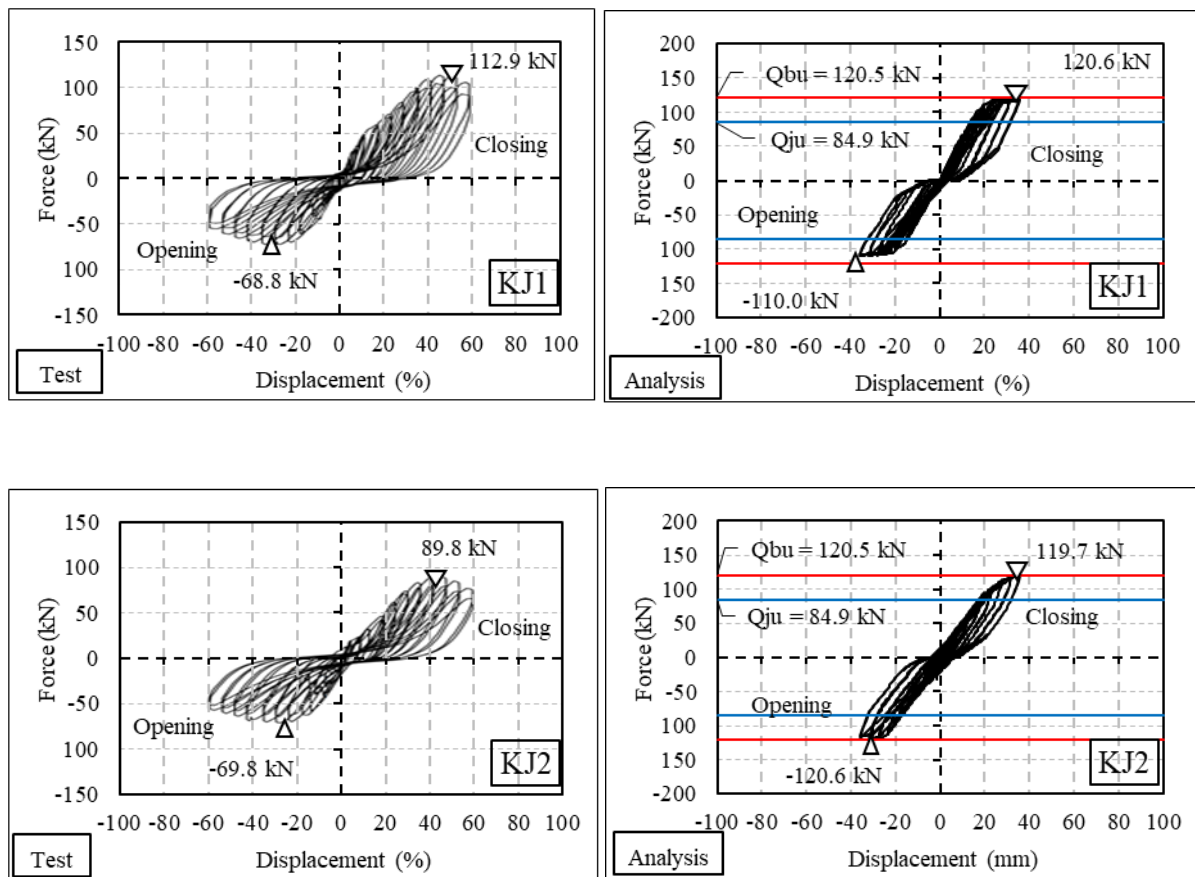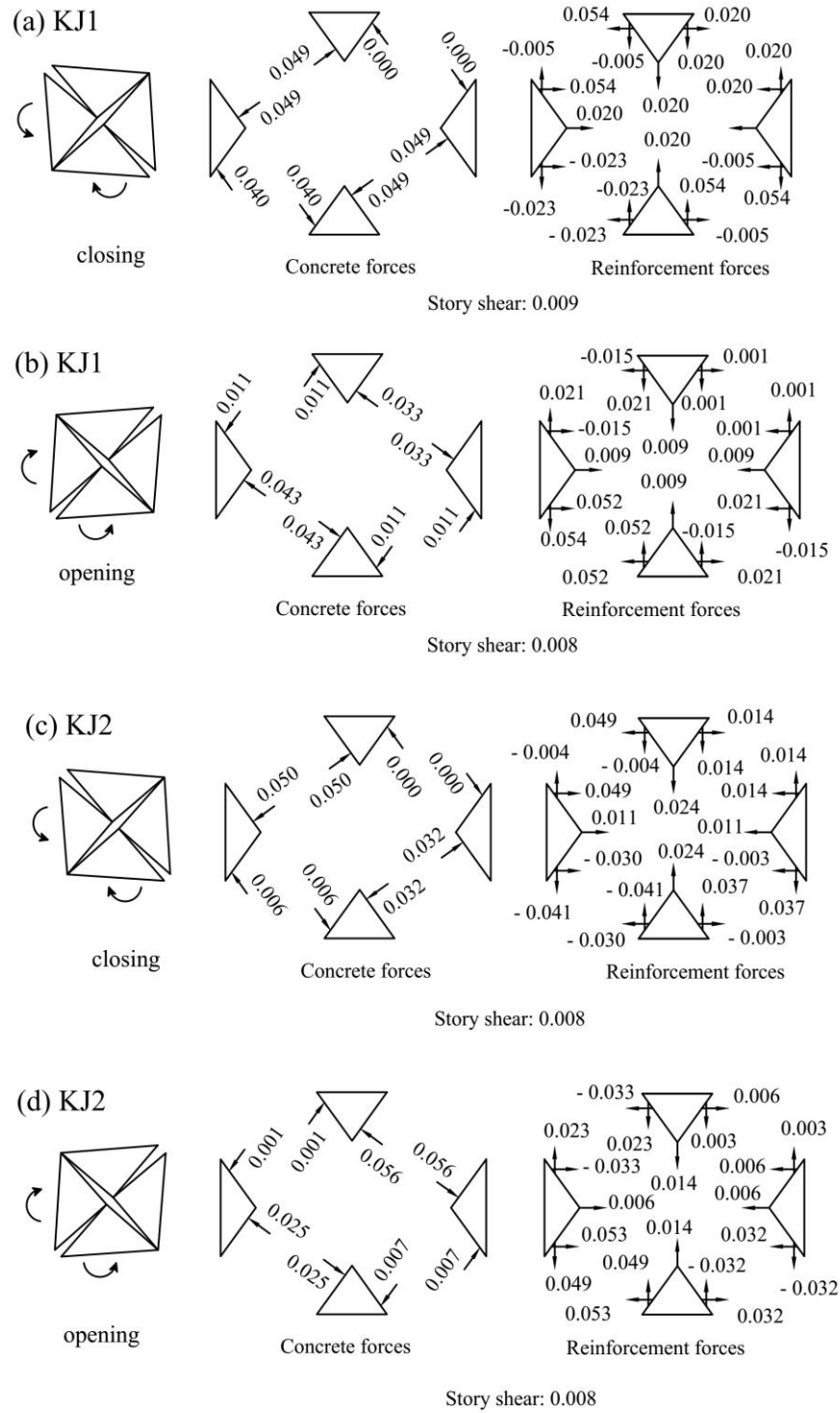Figure 3.19. Loading chart of test KJ1 and KJ2

112

Figure 3.20. Relationship of force and displacement of the actuator of specimen KJ1 and KJ2

(a) Specimen KJ1 in closing mode; (b) Specimen KJ1 in opening mode

(c) Specimen KJ2 in closing mode; (d) Specimen KJ2 in opening mode

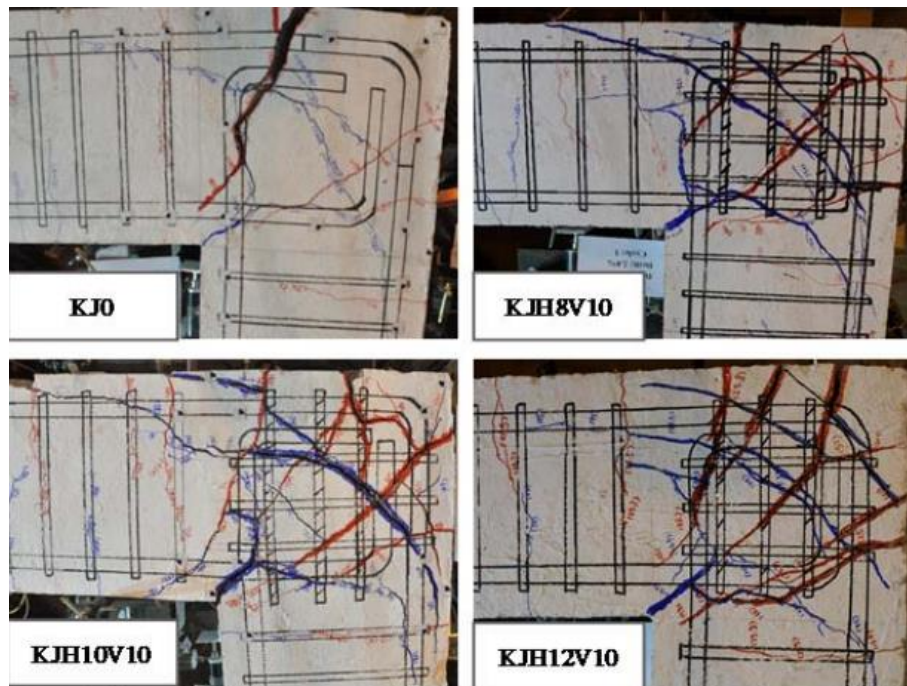Figure 3.21. Resultant forces in material of knee joint specimens

Figure 3.22. Cracking patterns of some knee joint specimens by Zhang and Mogili

3.4 Application on investigating the cyclic response of a RC frame

3.4.1 Introduction

Many RC frame buildings in the last century was designed from countries to countries without ductility, as a result, fail to fulfil modern standards for seismic resisting criteria. Recently, present codes have required stronger reinforcing details which are not considered fully in the past. Experience from collapse of existing buildings due to severe earthquakes also shows that demolition of those structures may be derived from causes such as inadequate reinforcing details and poor anchorage conditions, particularly in beam-column joint regions. In practical design, there are many cases in which stress in joint regions is pretty high due to using small columns reinforced by longitudinal bars with high strength or high ratio of reinforcement. During loading, diagonal cracks open and compressed concrete crushes on each other which causing deterioration on joint stiffness. Since contribution of beam-column joints on the overall response of a RC frame is crucial, this deterioration must be prevented to fulfil the rigidity assumption in analysis [33]. Many models for simulating seismic behaviors of joints including effects of joint failure local response on the whole performance of RC multi-storey frame building have been also proposed. Ghobarah and Biddah [51] used their joint model which

115

consisted of a shear rotational springs and a bond-slip rotational springs to study seismic response of a three storey frame and a nine storey frame. Calvis et al. [52] simulated a three story frame structure with typical deficiencies in the 1950s and 1970s, and simple joint model was utilized. They key point was to emphasize seismic vulnerabilities of a RC frame due to using smooth bars and inadequate anchorage method. A recent study conducted by Shiohara and Kusuhara has employed Kusuhara joint model to examine seismic performance of a four story RC frame [7, 10] designed as a strong column-weak beam structure satisfying Japan building standard. The study focused on influence of joint hinging failure on joint damage and the overall deformation with P-delta effect included.

With the main attention of the proposed beam column joint model, this part presents an application of the new element in simulating cyclic response of a 2D RC frame. Utilizing success of simulating cyclic response of interior joints and exterior joints previously, this part examines a further application of the new joint model into frame analysis.

3.4.2   Test specimen

As for application on RC frame simulation, a test of 2D RC frame with unequal span subjected to cyclic loading [53] was adopted for analysis. The frame is a ½ scale two-bay two-storey structure fabricated following the standard of Chinese code for seismic design of buildings [54]. Figure 3.23 denotes the front view of the frame with details of dimensions, reinforcements and concrete mentioned in Table 3.4. The frame is a 3.6-meter-high structure with the bottom beam attached to a rigid base while the top beam was loaded by cyclic loading through an actuator.

The research aimed to verify simulated response of the frame utilized the new joint model and analyzed influence of joint models on analytical results. For verification, the load – deflection relationship in term of story shear versus story drift was considered. Beside experimental data, computational results of the frame modelling beam-column joints as fiber elements by Wang et al. [53] was also utilized for comparison. The fiber element was developed by Spacone et al. [55, 56] and the computation was conducted on OpenSees program. The present study employed OBASAN program for analysis which considered three cases: modeling the frame using the new joint model, using a joint element with shear stiffness derived from the joint shear strength recommended by AIJ 1999 [1], and using rigid joints.

3.4.3 Verification of the experimental results

Figure 3.24 and Figure 3.25 show an idealized schematic for the frame with using the new joint model and notation of nodes and line elements respectively. Three interior joints (IJ1 to IJ3) and six exterior joints (EJ1 to EJ6) were simulated by the present joint element, whereas beams and columns were modelled simply by line elements with two nonlinear rotation springs at the ends and the flexural strength determined based on ACI 318 [2]. Points of contraflexure were assumed to be located at mid-span of beams and columns and trilinear hysteresis rule was applied for the moment – curvature skeleton.

In case of using joint shear strength, eight deformations of a joint element consisting of four axial deformations (δ_{x1}, δ_{x2}, δ_{z1}, δ_{z2}), four bending deformations (φ_{x1}, φ_{x2}, φ_{z1}, φ_{z2}) were assumed to follow linear rule with stiffness established from theory of elasticity, whereas shear deformation φ_0 was assumed to carry joint nonlinearity with anti-symmetric bending moment calculated based on the joint shear strength following AIJ 1999. For hysteresis rule, Takeda model [42] was employed for the anti-symmetric bending moment – shear deformation skeleton. Schematic of the third case with rigid joints was shown in Figure 3.26 with frame members simulated by line elements. Loading history applied on the frame is denoted in Figure 3.27 with three initial cycles for determining yielding displacement (Δ) and remaining cycles for displacement control. In this section, because the detailed experimental results regarding the failure mode of each joint in the frame and yielding of reinforcing bars were not available, the main interest was the overall load deflection relationship of the frame.

The relationship of loading force versus displacement of the top floor is presented in Figure 3.28. In Figure 3.28a, experimental result and analytical result by Wang [53] are shown in comparison to the response computed with the proposed joint model in Figure 3.28b. The result indicated that analysis with the new joint model returned in a good agreement with test data in which the difference of maximum load was 5.85% although the maximum force in negative path was pretty overestimated. Pinching effect in the analysis was quite similar to observation and was more apparent than that of Wang's model.

Figure 3.28c reveals the dominance of frame member strength in the case of using joint shear strength by AIJ 1999 as curves mostly are covered by the trilinear rule. Pinching effect does not occur and the shape looks like that of Wang's model, whereas the maximum force is overestimated 21.5%. Without using joint model or in other word, using rigid nodes for

simulating connections of beams and columns, the maximum force is pretty much overestimated (68.0%) in comparison to previous cases. Like the case with joint shear strength, pinching effect also does not occur.

Figure 3.29, Figure 3.30 and Figure 3.31 present in turn displacement of the first floor when simulating with the proposed joint model, with joint shear strength included and with rigid joint. There is little difference in results of the three cases and displacements are nearly a half of the second floor displacement. In frames with more stories, the different would be more apparent [57].

Table 3.4. Properties of frame members

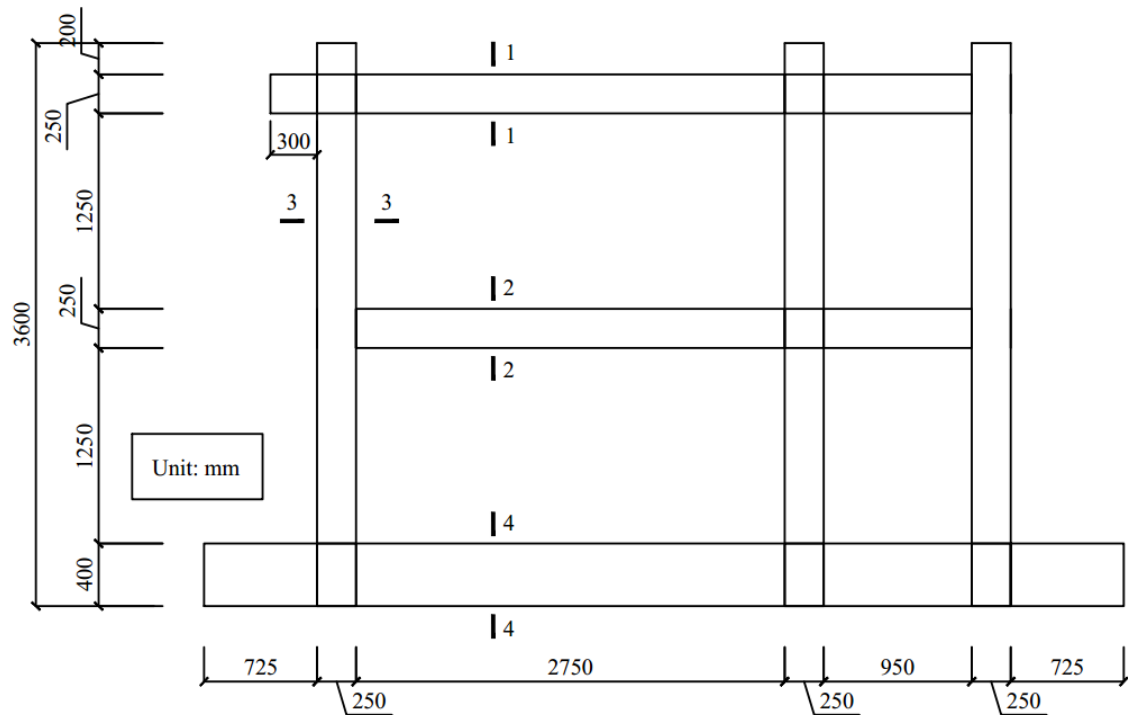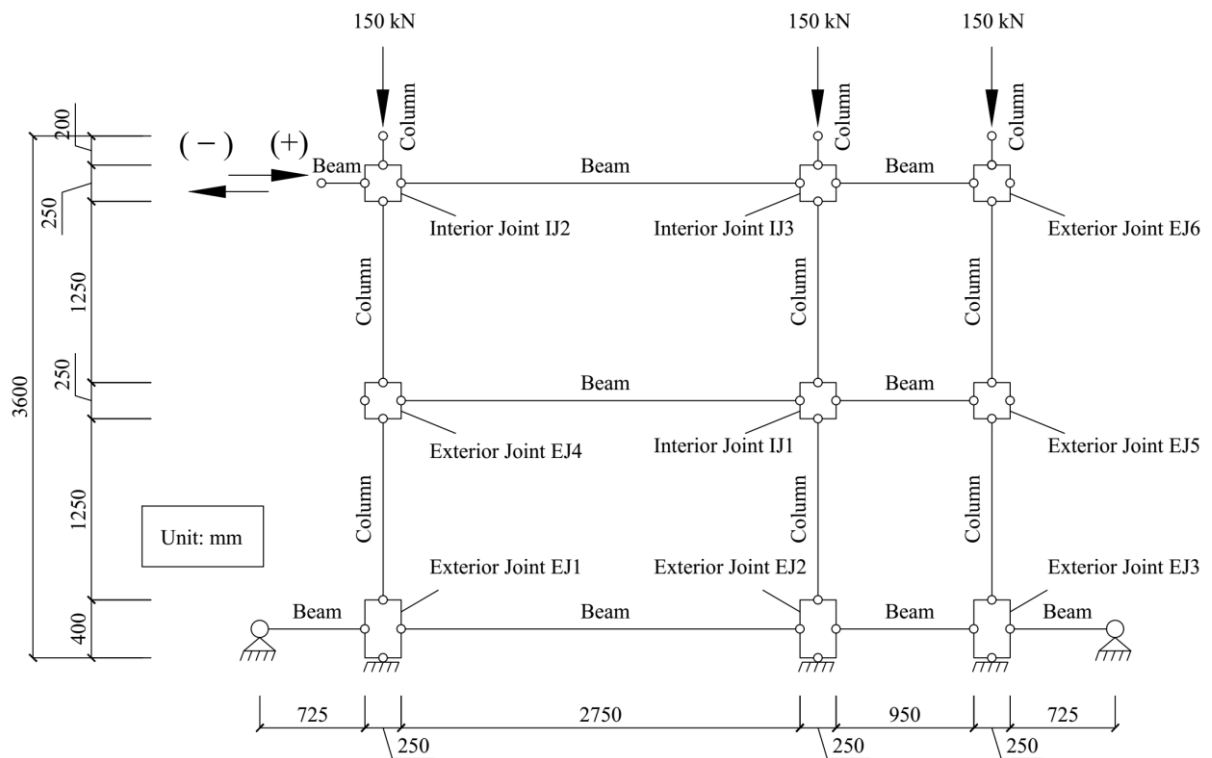| Section	1-1 & 2-2	3-3	4-4
concrete compressive strength (MPa)	19.04		
width x depth (mm)	150 x 250	200 x 250	350 x 400
longitudinal bars	2-D16	2-D16 2-D16	3-D22 2-D22
bar yielding strength (Mpa)	425	425	425
bar distant ratio	0.8	0.8 0.5	0.875 0
Joint hoops	D8@50		
Hoops yielding strength (Mpa)	305		

Figure 3.23. Front view of the frame

Figure 3.24. Analytical idealization of the frame under cyclic loading using the new joint element
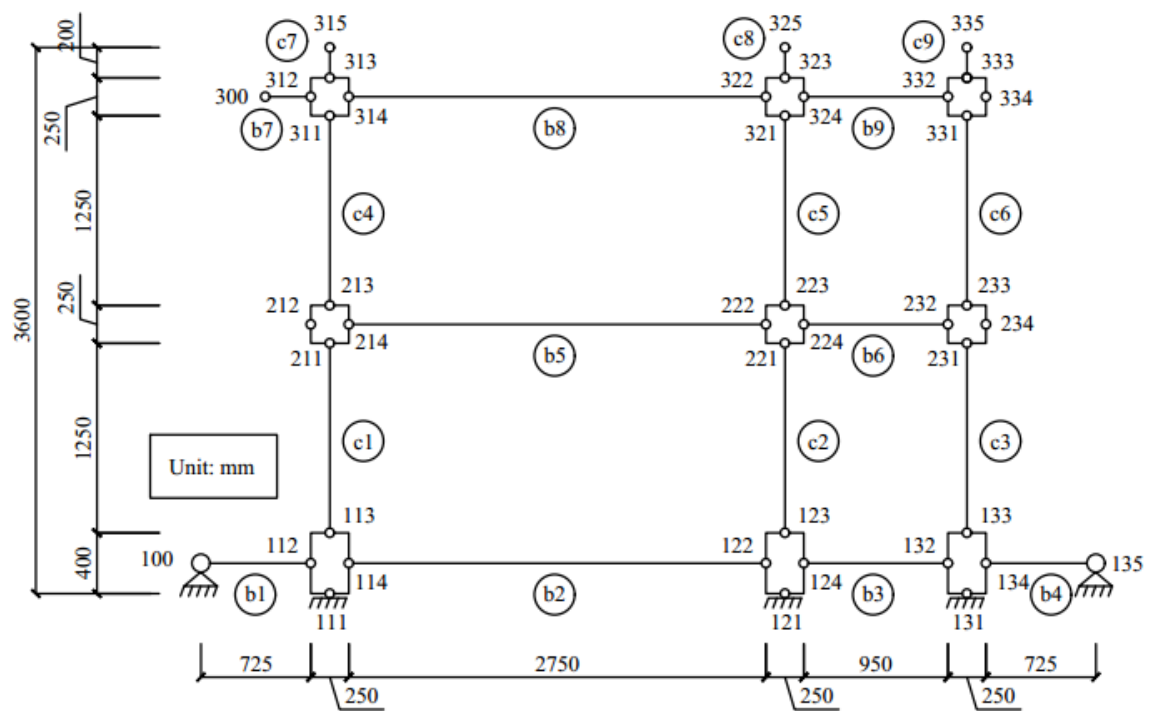
119

Figure 3.25. Numbering nodes and elements of the frame
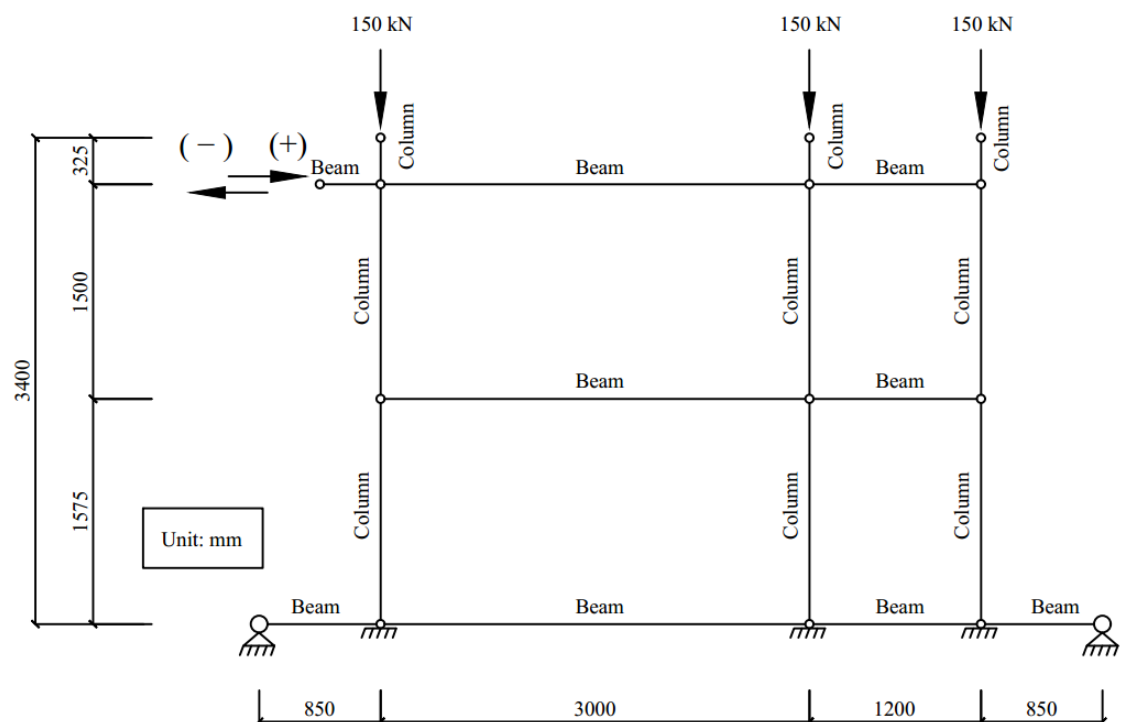

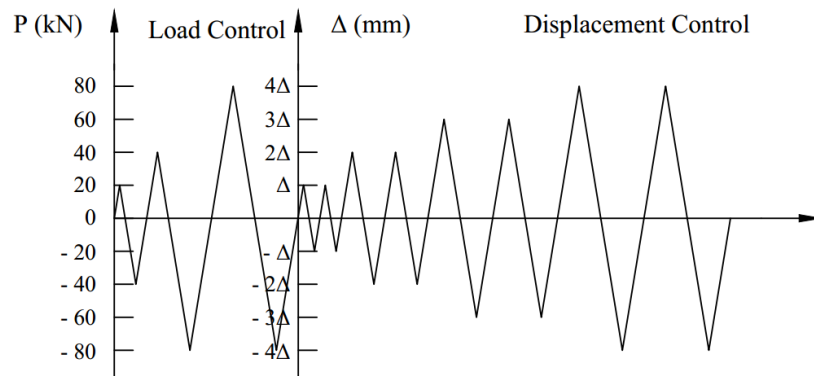Figure 3.26. Analytical idealization of the frame under cyclic loading with using rigid joints
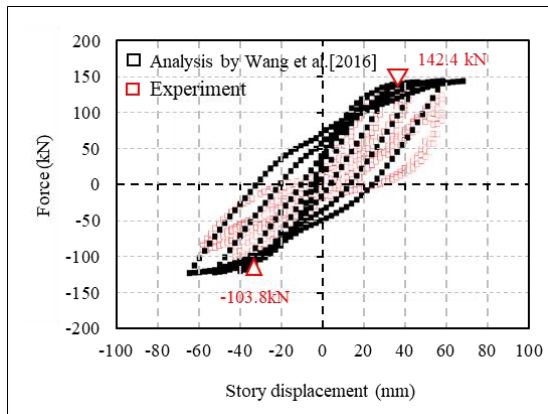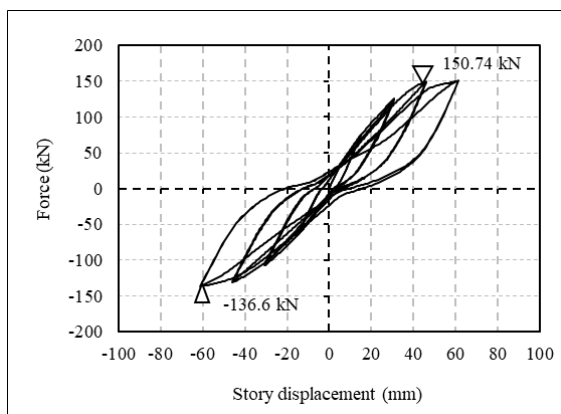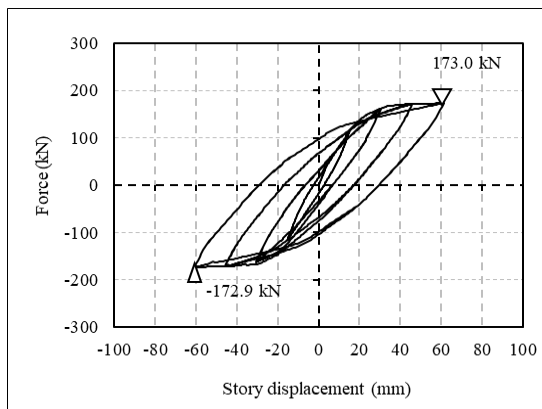
Figure 3.27. Loading history of the frame

(a) Experiment

(b) Analysis with using the new joint model

(c) Analysis using joint shear strength
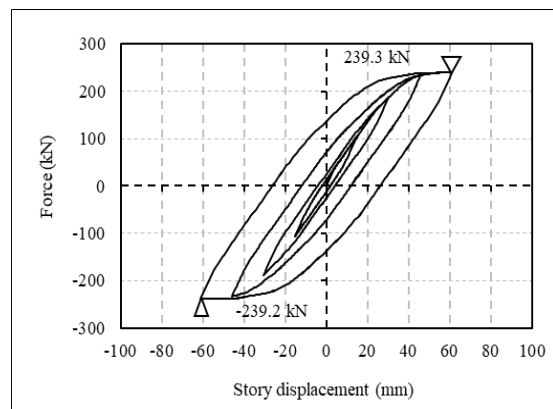
(d) Analysis rigid joint

Figure 3.28. Force versus displacement of the second floor relationship
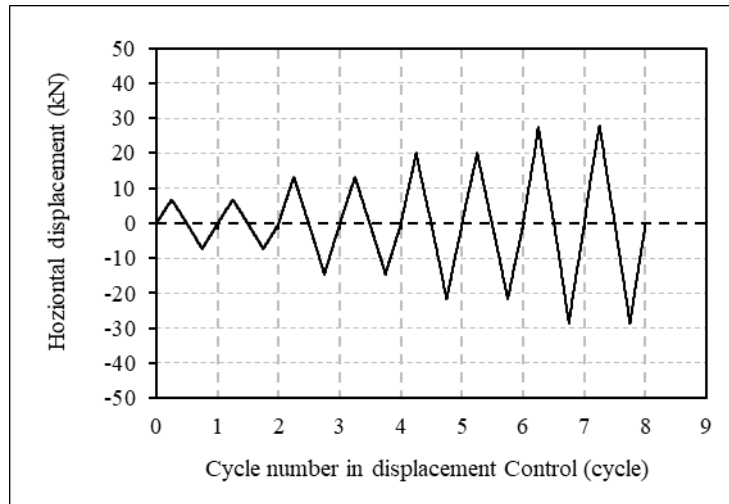
121

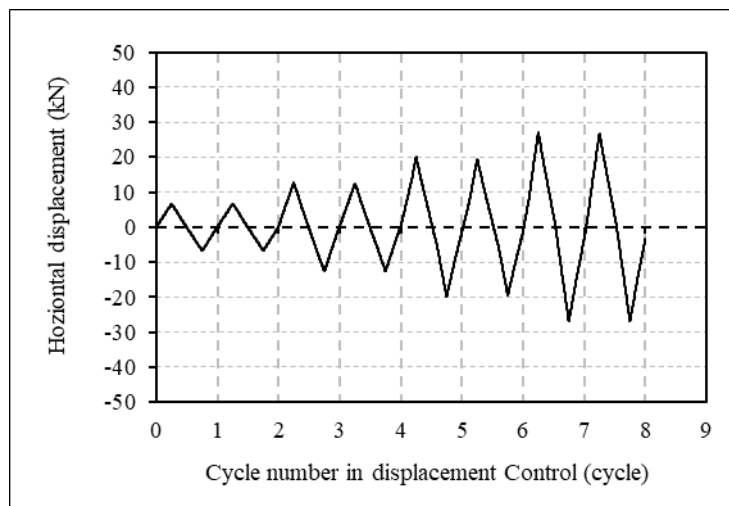Figure 3.29. Displacement of the first floor with using the new joint model

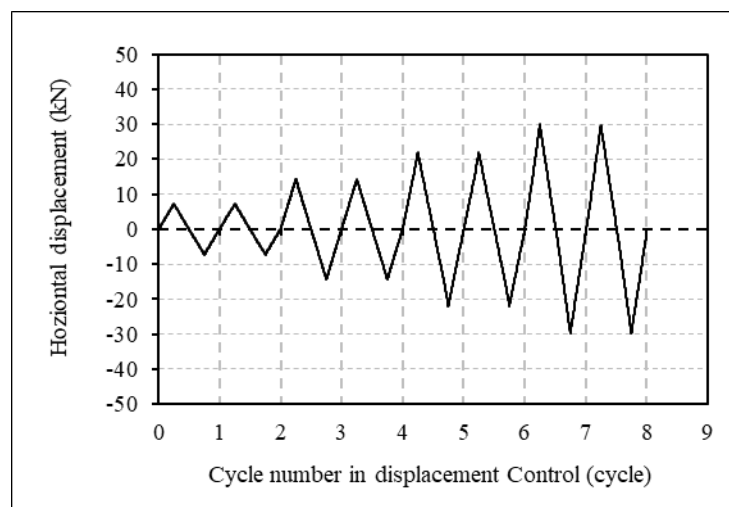Figure 3.30. Displacement of the first floor with using the joint strength (AIJ 1999)

Figure 3.31. Displacement of the first floor with using the rigid joint

122

3.5 Conclusion

Application of the new joint model on simulating cyclic response of exterior joints, knee joints, and a 2D RC frame was mentioned.

First, some modifications were included to develop the interior joint element into the exterior joint element. The ratio of the anchorage length of longitudinal bars in beam to column depth was the key factor which governed the location of the diagonal cracks and the size of free bodies. Deformation of concrete struts and bar springs were also determined from the rotation of the four triangular free bodies. To verify the new exterior joint model, an experiment on four exterior joint subassemblages under cyclic loading was adopted. Results indicated a good agreement between simulation and test with respect to load versus deflection relationship. The failure mode of each specimen was studied in which the prediction of reinforcement yielding showed a good agreement with the observation in most specimens. A comparison between the resultant forces in concrete and bar springs at the ultimate stage determined from the computation with the new exterior joint model and from Shiohara's numerical method was presented. The comparison results showed a good correlation between the two methods in predicting the resultant forces in most reinforcing bars and the very small compressive force in concrete zones near joint corner without beam bar anchoring.

Second, an application of the new joint model in investigating the cyclic response of knee joints was included. A test of two knee joint subassemblages with difference in reinforcing details was employed for verification. Because the ratio of the anchorage length in beam and column depth was close to unit ($\eta_{Cx} = \eta_{Cz} \approx 1$), the new interior joint model in Chapter 2 was used to model the two joint specimens. The results showed some disagreements between the computation and test data regarding the load-deflection relationship of specimens. The distinct difference in the response of the opening mode and the closing mode of specimen KJ1 which had the identical geometric properties of beam and column was not captured. Moreover, the same response of the opening mode in KJ1 and KJ2 was not predicted by the analysis. To improve the reliability of the analytical results, it was suggested that some further modifications in the crack pattern of the knee joint model were necessary based on the observed pattern from experiments.

Finally, an application of the proposed joint model on studying cyclic response of a 2D RC frame was mentioned. The frame had three interior joints and six exterior joints which were modelled by the joint elements in Chapter 2 and Chapter 3 respectively. Because the detailed observation of failure in each member of the frame was not available, only the overall load-deflection relationship was considered. The results indicated a good agreement on predicting the load-displacement response of the top floor. The reliability of using the new joint model in comparison to computation with the joint shear strength and with rigid joints was also pointed out.

Chapter 4 Conclusion and Recommendation for Future Research

4.1 Sumarry of research activities

The main purpose of the study is to propose a new analytical model for simulating cyclic response of RC beam column connections derived from Shiohara's theory of joint hinging.

Firstly, a new model for interior joints was proposed. Different from other multi-spring models, the present joint model was fabricated directly from Shiohara's mechanical model (SMM). Before cracks occurred, the joint element was considered to be elastic. After cracking, bar springs, bond-slip springs and concrete struts were used to characterize the joint nonlinear behaviors. In SMM, only equilibriums of external forces and resultant forces in concrete and reinforcements were mentioned to estimate the joint capacity. The present research used springs and struts with an aim to simulate those resultant forces. Moreover, the deformation of springs and concrete struts was determined from the rotation of the four free bodies in SMM. From the rotation of the free bodies, the displacement of the joint corner points and the joint center was computed by nine independent components of the joint deformations. Then, a linear distribution of concrete strain on joint diagonals was assumed to achieve the concrete stress through constitutive concrete model. Four concrete struts were defined to represent four concrete compressive zones and other four concrete struts were used to represent concrete tensile zones which were potentially carried compression in reversed loading. A definition of the length for these struts was suggested to assure the linear strain distribution assumption of concrete, while a detailed computational method to compute the average stress of struts from strain was also provided. In the same way, bar springs were introduced to represent reinforcing bars in joint core. The compatibility regarding relationship between deformations of springs and struts with joint deformations was established. As a result, the joint general stiffness was established to capture the joint response from the elastic stage till the ultimate stage. The interior joint model was developed gradually through several cases: monotonic response of interior joints with the identical depth and different depth of beam and column, with and without perfect bond condition, and cyclic response of interior joint with general properties. Verification by test data indicated the reliability of the interior joint model with respect to capturing the load-deflection

relationship and failure mode of joint specimens. The resultant forces in material at the ultimate stage were also confirmed by the numerical method of Shiohara.

Secondly, applications of the new joint model in investigating cyclic response of exterior joint, knee joint and a RC frame was introduced. The model of the exterior joint was developed in the same way of the interior joint model in which the ratio of the anchorage length of longitudinal bars in beam to column depth was the key parameter in determining the location of diagonal cracks and free bodies. For verification, the cyclic response of four exterior joint specimens were predicted well by the exterior joint model. The application of the interior joint model to simulate the performance of two knee joint specimens was studied. There were some disagreements between test data and the analytical results which led to suggestions of adjusting the location of diagonal cracks on the knee joint element based on the observed crack pattern. The interior joint in Chapter 2 and the exterior joint in Chapter 3 were employed to investigate the cyclic response of a RC frame. Due to the limitations of experimental data, only overall load-deflection relationship was considered which showed a good correlation between test result and the computation.

4.2 Conclusion

Through discussion in Chapter 2 and Chapter 3, the following conclusions of the research were reached:

- A new 2D analytical model to simulate cyclic response of beam column joints derived directly from Shiohara joint hinging theory was proposed.
- Joint compatibility was successful introduced into Shiohara mechanism.
- The new joint element showed reliability of predicting behaviors of 2D interior joints, 2D exterior joints and 2D frame.
- Application of the model on analysis cyclic behaviors of knee joints returns in the unreliable outcome, and further modifications are necessary.

4.3 Recommendation for further study

Following recommendations are suggested for other studies in the future:

- Adjusting several aspects regarding the diagonal cracks, reinforcing details and rigid bodies for applying on knee joints
- Developing the author's idea into a 3D joint model

- Developing the model into structural design tools in application for building analysis

References

[1]   Architectural institute of japan, Design guidelines for earthquake resistant reinforced concrete building based on ultimate strength concept and commentary. *AIJ-1999,* 1999 (In Japanese).

[2]   ACI Commitee, American Concrete Institute, International Organization for Standardization, Building code requirements for structural concrete (ACI 318-08) and commentary.

[3]   Standards New Zealand, Structural Design Actions, Part 5: Earthquake actions–New Zealand. 2004.

[4]   European Committee for Standardization, Design of structures for earthquake resistance-Part 1: General rules, seismic actions and rules for buildings. *Eurocode 8,* 2005.

[5]   Shiohara, H. New model for shear failure of RC interior beam-column connections. *Journal of Structural Engineering*. 2001; **127**: 152-160.

[6]   Shiohara, H. Reinforced concrete beam-column joints: An overlooked failure mechanism. *ACI Structural Journal*. 2012; **109**: 65.

[7]   Shiohara, H. and Kusuhara, F. The next generation seismic design for reinforced concrete beam-column joints. In: Proc. Tenth US National Conference on Earthquake Engineering, 2014.

[8]   Shiohara, H. A New AIJ standard for Seismic Capacity Calculation: Recent Advances in Beam-Column Joint Design and Seismic Collapse Simulation on Reinforced Concrete Frame Buildings. *Special Publication*. 2017; **313**: 1-10.

[9]   Tajiri, S., Shiohara, H. and Kusuhara, F. A new macroelement of reinforced concrete beam column joint for elasto-plastic plane frame analysis. In: Eight national conference of earthquake engineering, San Francisco, California, 2006.

[10]   Kusuhara, F., Kim, S. and Shiohara, H. Seismic Response of Reinforced Concrete Moment Resisting Frames of Beam-column Joint Yielding. *Journal of Construction and Structural Engineering, Architectural Institute of Japan*. 2013; **78**: 847-855.

[11]   Kim, S., Kusuhara, F. and Shiohara, H. Analysis of RC slab-beam-column sub-assemblages subjected to bi-directional lateral cyclic loading using a new 3D macro element. *Earthquake Engineering & Structural Dynamics*. 2017; **46(14)**: 2519-2536.

[12]   Durrani, A. J. and Wight, J. K., Experimental and analytical study of internal beam to column connections subjected to reversed cyclic loading. Dept. of Civil Engineering: A. A. Univ. of Michigan, Mich, Rep. No. UMEE 82R3, 1982.

[13]   Lehman, D., Stanton, J., Anderson, M., Alire, D. and Walker, S. Seismic performance of older beam-column joints. In: 13th World Conference On Earthquake Engineering, 2004.

[14]   Walker, S. G., Seismic performance of existing reinforced concrete beam-column joints. University of Washington. 2001.

[15]   Park, R. and Milburn, J. Comparison of recent New Zealand and United States seismic design provisions for reinforced concrete beam-column joints and test results from four units designed according to the New Zealand code. *Bulletin of the New Zealand national society for earthquake engineering*. 1983; **16**: 3-24.

[16]   Lowes, L. N., Mitra, N. and Altoontash, A., A beam-column joint model for simulating the earthquake response of reinforced concrete frames.

[17]   El-Metwally, S. and Chen, W. Moment-rotation modeling of reinforced concrete beam-column connections. *Structural Journal*. 1988; **85**: 384-394.

[18]   Morita, S. and Kaku, T. Hysteresis loops for reinforced concrete beam-column connections. In: Eighth World Conference on Earthquake Engineering, San-Francisco, CA, USA, 1984. 477–484.

[19]   Youssef, M. and Ghobarah, A. Modelling of RC beam-column joints and structural walls. *Journal of Earthquake Engineering*. 2001; **5**: 93-111.

[20]   Kent, D. C. and Park, R. Flexural members with confined concrete. *Journal of the Structural Division*. 1971;

[21]   Ghobarah, A. and Youssef, M. Modelling of reinforced concrete structural walls. *Engineering Structures*. 1999; **21**: 912-923.

[22]   Giuriani, E., Plizzari, G. and Schumm, C. Role of stirrups and residual tensile strength of cracked concrete on bond. *Journal of Structural Engineering*. 1991; **117**: 1-18.

[23]   Lowes, L. N. and Altoontash, A. Modeling Reinforced-Concrete Beam-Column Joints Subjected to Cyclic Loading. *Journal of Structural Engineering*. 2003; **129**: 1686-1697.

[24]   Vecchio, F. J. and Collins, M. P. The modified compression-field theory for reinforced concrete elements subjected to shear. *ACI J.* 1986; **83**: 219-231.

[25]   Eligehausen, R., Popov, E. P. and Bertero, V. V., Local bond stress-slip relationships of deformed bars under generalized excitations. EERC, University of California, Berkeley: 1983.

[26]   Viwathanatepa, S., Popov, E. P. and Bertero, V. V., *Effects of generalized loadings on bond of reinforcing bars embedded in confined concrete blocks*. University of California, Earthquake Engineering Research Center; 1979.

[27]   Shima, H., Chou, L.-L. and Okamura, H. Micro and macro models for bond in reinforced concrete. *Journal of the Faculty of Engineering*. 1987; **39**: 133-194.

[28]   Paulay, T. and Priestley, M. N. Seismic design of reinforced concrete and masonry buildings. 1992;

[29]   Paulay, T., Park, R. and Preistley, M. J. Reinforced concrete beam-column joints under seismic actions. In: Journal Proceeding, 1978. 585-593.

[30]   Park, R. and Paulay, T., *Reinforced concrete structures*. John Wiley & Sons; 1975.

[31]   Tran, T., Hadi, M. N. and Pham, T. M. A new empirical model for shear strength of reinforced concrete beam-column connections. 2014;

[32]   Sharma, A., Reddy, G., Eligehausen, R., Vaze, K., Ghosh, A. and Kushwaha, H. Experiments on reinforced concrete beam-column joints under cyclic loads and evaluating their response by nonlinear static pushover analysis. *Structural Engineering and Mechanics*. 2010; **35**: 99-117.

[33]   Shiohara, H. Quadruple flexural resistance in R/C beam-column joints. In: 13 th World Conference on Earthquake Engineering, 2004.

[34]   Park, R., Priestley, M. and Gill, W. D. Ductility of square-confined concrete columns. *Journal of the structural division*. 1982; **108**: 929-950.

[35]   Ramberg, W. and Osgood, W. R. Description of stress-strain curves by three parameters. *National Advisory Committee on Aeronautics, Technical Note 902*. 1943;

[36]   Nakamura, H. and Higai, T. Compressive fracture energy and fracture zone length of concrete. *Modeling of inelastic behavior of RC structures under seismic loads*. 2001; 471-487.

[37]   CEB-FIP CE, Model Code 1990. 1991.

[38]   Kurose, Y., Guimaraes, G. N., Zuhua, L., Kreger, M. E. and Jirsa, J. O., Study of Reinforced Concrete Beam-to-Column Joints Under Uniaxial and Biaxial Loading. 1988.

[39]   Scott, B. D., Park, R. and Priestley, M. J. Stress-strain behavior of concrete confined by overlapping hoops at low and high strain rates. In: Journal Proceeding, 1982. 13-27.

[40]   Giberson, M. F., The response of nonlinear multi-story structures subjected to earthquake excitation. Ph.D. Thesis. California Institute of Technology. 1967.

[41]   Otani, S. Inelastic analysis of R/C frame structures. *Journal of the Structural Division*. 1974; **100**: 1433-1499.

[42]   Takeda, T., Sozen, M. A. and Nielsen, N. N. Reinforced concrete response to simulated earthquakes. *Journal of the Structural Division*. 1970; **96**: 2557-2573.

[43]

[44]   Kusuhara, F. and Shiohara, H. Tests of R/C beam-column joints with variant boundary conditions and irregular details on anchorage of beam bars. In: 14th World Conference on Earthquake Engineering, Beijing, China, 2008.

[45]   Palermo, D. and Vecchio, F. J. Compression field modeling of reinforced concrete subjected to reversed loading: formulation. *Structural Journal*. 2003; **100**: 616-625.

[46]   Kusuhara, F. and Shiohara, H. Ultimate moment of reinforced concrete exterior beam-column joint. *Journal of Structural and Construction Engineering (AIJ)*. 2013; **78**: 1949-1968.

[47]   Architectural Institute of Japan, Design guidelines for earthquake resistant reinforced concrete building based on ultimate strength concept and commentary (AIJ-1999). 1999

[48]   Kusuhara, F. and Shiohara, H. Joint Shear? or Column-to-Beam Strength Ratio? Which is a key parameter for seismic design of RC Beam-column joints-Test Series on Exterior Joints. In: Proceeding of 15th World Conference on Earthquake Engineering, Lisbon, 2012.

[49]   Shiohara, H., New Model for Joint Shear Failure of R/C Exterior Beam-column Joints. Pacific earthquake engineering research center: 2002.

[50]   Mogili, S., Kuang, J. S. and Zhang, N. Seismic Behaviour of RC Knee Joints in Closing and Opening Actions. *World Academy of Science, Engineering and Technology, International Journal of Civil, Environmental, Structural, Construction and Architectural Engineering*. 2017; **11**: 393-398.

[51]   Ghobarah, A. and Biddah, A. Dynamic analysis of reinforced concrete frames including joint shear deformation. *Engineering Structures*. 1999; **21**: 971-987.

[52]   Calvi, G. M., Magenes, G. and Pampanin, S. Relevance of beam-column joint damage and collapse in RC frame assessment. *Journal of Earthquake Engineering*. 2002; **6**: 75-100.

[53]   Wang, L., Wei, X., Ning-Ning, F., Shuping, C., Feng, L. and Qiumei, G. Research on Seismic Performance of Reinforced Concrete Frame with Unequal Span Under Low Cyclic Reversed Loading. *The Open Civil Engineering Journal*. 2016; **10**:

[54]   Ministry of Housing and Urban-Rural Development of the People's Republic of China, Code for Design of Concrete Structures. *GB50011-2010,* 2010 (In Chinese).

[55]   Taucer, F., Spacone, E. and Filippou, F. C., *A fiber beam-column element for seismic response analysis of reinforced concrete structures*. Earthquake Engineering Research Center, College of Engineering, University of California Berkekey, California; 1991.

[56]   Spacone, E., Filippou, F. C. and Taucer, F. F. Fibre beam–column model for non-linear analysis of R/C frames: Part I. Formulation. *Earthquake Engineering & Structural Dynamics*. 1996; **25**: 711-725.

[57]   Favvata, M. J., Izzuddin, B. A. and Karayannis, C. G. Modelling exterior beam–column joints for seismic analysis of RC frame structures. *Earthquake Engineering & Structural Dynamics*. 2008; **37**: 1527-1548.

List of Publications

Journal Papers

Xuan Hoa TRAN and Yoshiro KAI. Modeling interior reinforced concrete beam-column joint based on an innovative theory of joint shear failure, *International Journal of Japan Architectural Review for Engineering and Design* (under review).

Xuan Hoa TRAN and Yoshiro KAI. Modeling exterior reinforced concrete beam-column joint based on an innovative theory of joint shear failure, *International Journal of Concrete Structures and Materials* (under review).

Xuan Hoa TRAN and Yoshiro KAI. Developing a new method to model concrete in beam-column joint under cyclic loading based on the joint hinging mechanism, *International Journal of Japan Architectural Review for Engineering and Design* (under review).

International Conference

Xuan Hoa TRAN and Yoshiro KAI. A new model for reinforced concrete beam-column joint subjected to cyclic loading. *The international symposium of Japan Association for Earthquake Engnineering*, Kochi, Japan, September 26-27, 2016.

Xuan Hoa TRAN and Yoshiro KAI. Developing an analytical model of reinforced concrete beam-column joint based on an innovative approach of joint shear failure mechanism in application for disaster prevention. *International Symposium of the 11th SSMS and the 5th RCND 2017*, Bangkok, Thailand, September 20-21, 2017.

Xuan Hoa TRAN and Yoshiro KAI. Investigation on seismic response of 2D frame structure using a new macro-element model of beam-column connections. *10th European Solid Mechanics Conference,* Bologna, Italy, July 2-6, 2018.

Acknowledgement